



저작자표시-비영리-변경금지 2.0 대한민국

이용자는 아래의 조건을 따르는 경우에 한하여 자유롭게

- 이 저작물을 복제, 배포, 전송, 전시, 공연 및 방송할 수 있습니다.

다음과 같은 조건을 따라야 합니다:



저작자표시. 귀하는 원저작자를 표시하여야 합니다.



비영리. 귀하는 이 저작물을 영리 목적으로 이용할 수 없습니다.



변경금지. 귀하는 이 저작물을 개작, 변형 또는 가공할 수 없습니다.

- 귀하는, 이 저작물의 재이용이나 배포의 경우, 이 저작물에 적용된 이용허락조건을 명확하게 나타내어야 합니다.
- 저작권자로부터 별도의 허가를 받으면 이러한 조건들은 적용되지 않습니다.

저작권법에 따른 이용자의 권리는 위의 내용에 의하여 영향을 받지 않습니다.

이것은 [이용허락규약\(Legal Code\)](#)을 이해하기 쉽게 요약한 것입니다.

[Disclaimer](#)

공학박사 학위논문

제일 원리 계산을 이용한
금속 공기 전지의 화학반응 규명

**First-principles study on the
reaction chemistry of metal-air batteries**

2018 년 2 월

서울대학교 대학원

재료공학부

이 병 주

Abstract

First-principles study on the reaction chemistry of metal-air batteries

Lee, Byungju

Department of Material Science and Engineering

College of Engineering

The Graduate School

Seoul National University

Nowadays, development of battery systems with high energy density and low cost as well as environmental sustainability is becoming important due to fast-growing market of large energy storage applications such as electric vehicles and energy storage systems. Lithium ion batteries, which have powered portable devices during recent decades, are predicted to be unable to supply future battery demands because of their limited energy density and high production cost. Metal-air batteries, which

exploit direct reaction of metal (e.g. Li, Na, K, Al, ...) and gas molecule (O_2 , CO_2 , SO_2 , ...), are regarded as one of the most promising post-LIB system, because of their exceptionally high energy density. However, metal-air batteries generally suffers from poor cycle life and low energy efficiency, which is originated from side reaction and high polarization during cycling.

Lithium-oxygen batteries and sodium-oxygen batteries are most intensively studied system among metal-air system, due to the abundance of elements and highest energy density of the system. Despite the chemical similarity of Li and Na, the two systems exhibit distinct characteristics, especially the typically higher charging overpotential observed in Li-oxygen batteries. In previous theoretical and experimental studies, this higher charging overpotential was attributed to factors such as the sluggish oxygen evolution or poor transport property of the discharge product of the Li-oxygen cell; however, a general understanding of the interplay between the discharge products and overpotential remains elusive. In **chapter 2**, I investigated the charging mechanisms with respect to the oxygen evolution reaction (OER) kinetics, charge-carrier conductivity, and dissolution property of various discharge products reported in Li-oxygen and Na-oxygen cells. The OER kinetics were generally faster for superoxides (*i.e.*, LiO_2 and NaO_2) than for peroxides (*i.e.*, Li_2O_2 and Na_2O_2). The electronic and ionic conductivities were also predicted to be significantly higher in superoxide phases than in peroxide phases. Moreover, systematic calculations of the dissolution energy of the discharge products in the electrolyte, which mediate a

solution-based OER reaction, revealed that the superoxide phases, particularly NaO_2 , exhibited markedly low dissolution energy compared with the peroxide phases. These results imply that the formation of superoxides instead of peroxides during discharge may be the key to improving the energy efficiency of metal–oxygen batteries in general.

The discovery of effective catalysts is an important step toward achieving Li-O_2 batteries with long-cycle life and high round-trip efficiency. Soluble-type catalysts or redox mediators (RMs) possess great advantages over conventional solid catalysts, generally exhibiting much higher efficiency. In **chapter 3**, I select a series of organic RM candidates as a model system to identify the key descriptor in determining the catalytic activities and stabilities in Li-O_2 cells. It is revealed that the level of ionization energies, readily available parameters from database, of the molecules can serve such a role when comparing with the formation energy of Li_2O_2 and the highest occupied molecular orbital energy of the electrolyte. It is demonstrated that they are critical in reducing the overpotential and improving the stability of Li-O_2 cells, respectively. Accordingly, I propose a general principle for designing feasible catalyst and report a RM, dimethylphenazine, with a remarkably low overpotential and high stability.

I believe that the fundamental understandings investigated in this thesis, which elucidated the effect of possible origin of charge overpotential (chapter 2) and reaction mechanism of soluble catalyst in lithium-oxygen cell (chapter 3), can provide

intuition to the researchers in this field.

Keywords : Energy storage, First principle calculation, Metal-Air battery, Redox mediator

Student Number : 2014-30196

Table of Contents

Abstract.....	i
Table of Contents.....	v
List of Figures	vii
List of Tables.....	xvii
Chapter 1. General Introduction.....	1
1.1 Introduction to metal-air battery.....	1
1.2 Introduction to density functional theory calculation	4
1.3 References	6
Chapter 2. Theoretical evidence for low charging overpotentials of superoxide discharge products in metal- oxygen batteries.....	9
2.1 Introduction	9
2.2 Computational details	13
2.2.1 Conductivity calculations.....	13
2.2.2 Dissolution properties of discharge products.....	15
2.3 Result and Discussion	20
2.3.1 OER from crystalline surfaces	20
2.3.2. Charge transport in discharge products	30
2.3.3 Dissolution of discharge products in the solution-based charging process	45

2.3.4 Supplementary Notes	51
2.4 Conclusion	54
2.5 References	55
Chapter 3. Rational design of redox mediators for advanced Li-O₂ batteries	63
3.1 Introduction	63
3.2 Method.....	66
3.2.1 Calculations details.....	66
3.2.2 Preparation of Li-O ₂ cells	70
3.2.3 Characterizations.....	71
3.3 Results and discussion.....	73
3.3.1 Screening for RMs based on ionization energy	73
3.3.2 Verification of the catalytic effect of RMs	79
3.3.3 Understanding the reaction mechanism of RMs	86
3.3.4 Catalytic effect of DMPZ for Li-O ₂ batteries	102
3.3.5 Supplementary Notes	112
3.4 Conclusion.....	125
3.5 References	126
Chapter 4. Summary.....	136
Abstract in Korean.....	138
Curriculum Vitae	141

List of Figures

Figure 1-1. Reaction mechanism of lithium-oxygen batteries.

Figure 2-1. Suggested mechanisms for OER in metal-oxygen batteries.

Figure 2-2. Formation energy per oxygen atom calculated in HSE ($\alpha=0.48$) at 0 K versus the formation enthalpy measured at standard state, 298 K and 1 atm. Black squares, red circles, blue triangles indicate oxides, peroxides, superoxides respectively. Black dash line shows exact correspondence between experiment and calculation, while red solid line is linear regression fitted to all data points which yields slope of 1.003 and y-intercept of 0.468. Note that separate fittings for oxides, peroxides, superoxides in the same data set result in overbinding correction of 0.590, 0.335, and 0.317 eV/O respectively. However, relative conductivity differences among the discharge products in this study were not largely changed (Table 2-1).

Figure 2-3. Crystal structure of (a) pyrite NaO_2 , (b) Na_2O_2 , (c) Li_2O_2 and (d) LiO_2 . Yellow, green and red atoms represent sodium, lithium, oxygen respectively. Black box with dash line indicates oxygen dumbbell ion (O_2^{n-}) in the structure.

Figure 2-4. Relationship between cell voltage and oxygen partial pressure, in the Li/O_2 cell. Higher cell voltage is related with more negative Gibbs free energy, according to Nernst equation; $\mu_{\text{Li}} - \mu_{\text{Li}}^0 = -nFE_{\text{cell}}$, where μ_{Li} is chemical potential of metal Li in structure, μ_{Li}^0 is chemical potential of pure metal, n is the number of charge of metal ion, F is faraday constant, E_{cell} is the voltage of the cell.

HSE functional was used for energy calculation. LiO_2 becomes more stable than Li_2O_2 in about 25 atm of oxygen partial pressure.

Figure 2-5. (a-g) The low index surface structures of LiO_2 and their terminations. (h) Wulff shape of LiO_2 was constructed from calculated surface energies. For surface energy calculations, a slab/vacuum geometry composed of repeating slabs and vacuum layers was adopted.

Figure 2-6. OER energy profile of LiO_2 under the calculated equilibrium potential $U = 2.76$ V, in (a) (101) surface, (b) (110) surface and (c) (111) surface. During the OER, oxygen or metal atoms leave the surface upon charging. In the situation, two sequences are possible; the metal ion extraction which is the electrochemical reaction (black) or the oxygen molecule evolution, the chemical reaction (red). The energies of the intermediate steps of the OER were calculated by removing metal ions or oxygen molecules from the surface. One OER cycle can be modeled by considering the atoms in the surface of the unit cell.

Figure 2-7. Density of state (DOS) of intrinsic (a) NaO_2 , (b) Na_2O_2 , (c) LiO_2 and (d) Li_2O_2 , calculated with HSE hybrid functional. Mixing coefficient (α) was chosen as 0.48. Calculated bandgap was 3.3, 5.8, 3.7 and 6.8 eV for NaO_2 , Na_2O_2 , LiO_2 and Li_2O_2 respectively.

Figure 2-8. Formation energies of low energy defects in (a) NaO_2 , (b) Na_2O_2 , (c) LiO_2 and (d) Li_2O_2 versus Fermi energy. Red dash line is Fermi energy which satisfies charge neutrality.

Figure 2-9. The hopping paths of hole and their hopping barrier in (a) NaO_2 , (b)

Na₂O₂, (c) LiO₂ and (d) Li₂O₂, calculated with HSE hybrid functional.

Figure 2-10. The hopping paths of negatively charged metal vacancy and their hopping barrier in (a) NaO₂, (b) Na₂O₂, (c) LiO₂ and (c) Li₂O₂, calculated with GGA functional and NEB method.

Figure 2-11. Increase of conductivity in logarithm as a function of applied charging overpotential. Red dash lines indicate that charging overpotential of 1.1 V and 0.7 V is required for Li₂O₂ and LiO₂ respectively, to reach same conductivity of NaO₂ with 0.1 V overpotential applied.

Figure 2-12. Required overpotential to form metal deficient phase of discharge product, Li_{1-x}O₂, Na_{1-x}O₂, Li_{2-x}O₂, Na_{2-x}O₂, 0.01 < x < 0.06.

Figure 2-13. The dissolution energy of LiO₂, NaO₂, Li₂O₂ and Na₂O₂. (a) in molecular and ionic form with respect to their bulk structure at dielectric constant (ϵ) = 10. The dielectric constant dependence of the dissolution energy in (b) superoxide species and (c) peroxide species were studied to investigate effect of different solvents.

Figure 2-14. Relation between LiO₂ ion dissolution energy (vs. intermediate product LiO₂ at the surface) in ref. 51 and LiO₂ ion dissolution energy (vs. bulk LiO₂) in this study, calculated from interpolation of data in Figure 4(b), dielectric constants of 80.16 (H₂O), 46.45 (DMSO), 36.71 (DMF), 37.78 (DMA), 32.17 (NMP) and 7.2 (DME) were used.

Figure 3-1. Role of RM for Li-O₂ batteries. (a) Schematic illustration of reaction mechanism of RM for Li-O₂ batteries. During the charge, RM (blue circles) is oxidized near the electrode surface (step 1, electrochemical reaction), then RM⁺ (red

circles) chemically oxidizes Li_2O_2 to 2Li^+ (green circle) and O_2 gas (orange circles). Finally, RM^+ is reduced to the initial state of RM (step 2, chemical reaction). (b) Schematic discharge (black line) and charge profiles of Li- O_2 batteries with (blue line) and without RM (red line).

Figure 3-2. Relationship between ionization energy in a vacuum and oxidation voltage (vs. Li/Li^+) in TEGDME electrolyte for the RM candidates described in Table 3-3.

Figure 3-3. FT-IR spectra of (a) NDA, (b) TMA, (c) PPD, (d) NC, and (e) DMPZ in the range of $1800\text{--}650\text{ cm}^{-1}$. The spectra were obtained after dissolving the RMs in TEGDME. All the RMs were well dissolved in TEGDME and stable even after 10 days. Although NC was not identified after its dissolution in the electrolyte, the electrolyte exhibited no changes and appeared to be stable.

Figure 3-4. Electrochemical properties of various RMs. (a) Change of OCVs of Li- O_2 cells with various RMs upon a time. The line with small circles indicates the reference cell without catalyst. (b) Electrochemical oxidation potentials of RMs dissolved in the electrolyte under an Ar atmosphere. The dotted line is the theoretical formation voltage of Li_2O_2 . (c) The first discharge and charge profiles of Li- O_2 cells using various 0.01 M RMs at a constant current density of 0.2 mA cm^{-2} . Discharge capacity are limited to 1 mAh and recharged to the same capacity. The reference (the line with small circles) indicates the electrochemical profile of Li- O_2 cell without catalyst.

Figure 3-5. The first discharge and charge profiles of Li-O₂ cells using a) Ketjen black electrode with LiI catalyst and b) carbon nanotube mesh electrode with LiI catalyst. The discharge capacity is limited to 1000 mAhg⁻¹, and the current density is 200 mA g⁻¹. Even if the Li-O₂ cells used the same soluble catalyst of LiI, the charge profiles were different based on the types of air cathodes used. A slight deviation of the charge profile is observed in the cell using the bulk carbon of Ketjen black because of the transport limitations of the catalyst and reaction products, whereas constant charge potential was observed using the hierarchically porous carbon nanotube mesh electrode.

Figure 3-6. Gas analyses on effect of RMs. (a) Schematic illustration of the gas analysis process. RMs dissolved in the electrolyte were electrochemically charged to 0.03 mAh, and the electrolyte containing the RMs⁺ was transferred to the excess Li₂O₂ powder in a glass vial. Then, the evolved inner gases were flowed into the gas analyzer. Detections of the evolved oxygen using (b) TTF and LiI, (c) NDA, (d) TMA, (e) PPD, and (f) DMPZ. The Ar carrier gas was flowed in at a constant rate of 10 ml min⁻¹, and the dotted line represents the injection time of the electrolyte in the vial.

Figure 3-7. Molecular orbital energies of RMs and TEGDME. HOMO and LUMO energies of original RMs (black line) and first oxidized RMs (red line) in TEGDME electrolyte based on DFT calculations. The dotted blue line represents the theoretical formation energy of Li₂O₂ ($2\text{Li}^+ + \text{O}_2 + 2\text{e}^- \leftrightarrow \text{Li}_2\text{O}_2$, 2.96 V vs. Li/Li⁺), and the redox potentials of $\text{RM}^+ + \text{e}^- \leftrightarrow \text{RM}$ reactions are indicated in yellow region, which are required to be higher than 2.96 V. The dotted black line represents the HOMO energy

of TEGDME. When SOMO of oxidized RM is lower than HOMO of TEGDME, the RM can react with the electrolyte (purple box), otherwise, the RM is stable in TEGDME (green box). Black shaded area indicates the relative instability of molecules possibly reacting with TEGDME.

Figure 3-8. HOMO and LUMO energies of original RMs (black line) and first oxidized RMs (red line) in DMSO electrolyte using DFT calculations. The dotted blue and black lines represent the theoretical formation energy of Li_2O_2 and the HOMO energy of DMSO, respectively.

Figure 3-9. HOMO and LUMO energies of 1,4-dioxane and N,N-dimethylformamide in TEGDME electrolyte using DFT calculations. 1,4-dioxane and N,N-dimethylformamide have high I.E. values of ~6.8 and ~6.9 eV in TEGDME, respectively, which are quite high compared with those of the other RM candidates described in Figure 3-7. Therefore, it is believed that these molecules are not oxidized under a typical voltage window (2.0–4.5 V), as demonstrated in Figure 3-4c.

Figure 3-10. Schematic energy diagram of (a) $2\text{RM}^+ + \text{Li}_2\text{O}_2 \leftrightarrow 2\text{RM} + 2\text{Li}^+ + \text{O}_2$ reaction in case of $E^\circ(\text{RM} \leftrightarrow \text{RM}^+) < 2.96 \text{ V}$ (b) relative MO position of RM/TEGDME, and (c) TEGDME decomposition reaction in the presence with RM^+ whose HOMO is lower than that of the solvent. See Supplementary Note 2 for detailed discussion.

Figure 3-11. (a) HOMO and LUMO energies and (b) molecular structures of TMPD, TEMPO, TDPA and FePc in TEGDME electrolyte based on DFT calculations. See Supplementary Note 3 for detailed discussion.

Figure 3-12. The HOMO/LUMO energies of five representative solvents used in the Li-O₂ battery. See Supplementary Note 4 for detailed discussion.

Figure 3-13. Cyclic voltammetries of RMs. CV and chemical structure of (a) NDA, (b) TMA, (c) PPD, and (d) DMPZ in 1 M LiTFSI/TEGDME under an Ar atmosphere at a scan rate of 100 mV s⁻¹. (e) CV of DMPZ for 200 cycles in the voltage range of 2.0–4.5 V vs. Li/Li⁺. (f) CV of DMPZ in 1 M TBATFSI/DMSO under an Ar and an O₂ atmosphere.

Figure 3-14. CV of (a) NDA, (b) TMA, and (c) PPD in 0.1 M TBATFSI/DMSO under Ar atmosphere at a scan rate of 100 mV s⁻¹. In total, 1 mM of the RMs was added to the electrolyte.

Figure 3-15. HOMO and LUMO energies of original RMs (black line) and second oxidized RMs (red line) in TEGDME electrolyte based on DFT calculations. See Supplementary Note 5 for detailed discussion.

Figure 3-16. Cyclability of the Li-O₂ cells with and without DMPZ catalyst. The capacity is limited to 500 mAh g⁻¹ at a constant current of 0.2 mA cm⁻² in an oxygen atmosphere. See Supplementary Note 6 for detailed discussion.

Figure 3-17. Average redox voltage of DMPZ/DMPZ⁺ along with the cycle numbers. The scan rate was constantly maintained at 100 mV s⁻¹. We investigated the stability of DMPZ/DMPZ⁺ redox under the prolonged cycles. Figure 3-17 shows that the redox potentials of DMPZ/DMPZ⁺ is highly stable for a few thousands cycles. Average redox voltages of DMPZ/DMPZ⁺ are constantly maintained, which implies that the redox of DMPZ/DMPZ⁺ is reversible and stable.

Figure 3-18. Effects of DMPZ as a catalyst for Li-O₂ battery. (a) *Ex situ* XRD patterns of Li-O₂ cells using DMPZ catalyst: as-prepared, after discharge, and after re-charge. (b) GITT voltage profile of Li-O₂ cell using DMPZ catalyst during discharge (blue) and charge (red). The dotted line is the theoretical formation voltage of Li₂O₂ (2.96 V vs. Li/Li⁺) and the inset presents a voltage vs. time plot. FESEM images of the air electrode: (c) as-prepared, (d) after discharge, and (e) re-charge at same magnification.

Figure 3-19. Electrochemical oxidation of DMPZ to 4.5 V in TEGDME electrolyte. The theoretical capacity that DMPZ alone can contribute by the oxidation to DMPZ⁺ and DMPZ²⁺ in the absence of Li₂O₂ is approximately 0.1 mAh based on the amount of RMs used in the Li-O₂ cell. Accordingly, the capacity from the intrinsic DMPZ oxidation is close to 0.1 mAh, as shown in Figure 3-19, followed by the electrolyte oxidation in the continuing charge over 4.2 V. Considering that the capacity of the Li-O₂ cell in Figure 3-42c is 1 mAh, which is 10 times higher than the possible capacity from RM, the charge capacity with the low overpotential in Figure 3-4c clearly demonstrates a continuous and simultaneous reduction of DMPZ⁺ to DMPZ by reacting with Li₂O₂ during the charge process.

Figure 3-20. FT-IR spectra of DMPZ in the range of 1800–650 cm⁻¹. The spectra were obtained after dissolving the RMs in TEGDME electrolyte with Ar and O₂ bubbling. The stability of DMPZ in the presence of oxygen was first examined with 0.01M and 1M concentration of DMPZ in TEGDME-based electrolyte. We dissolved DMPZ in the electrolyte and bubbled with O₂ for 1 hour before carrying out FTIR measurements. Figure 3-20 shows that there is no dominant change in the peaks from

both DMPZ and electrolyte, which indicates the stability of DMPZ with the oxygen in the electrolyte.

Figure 3-21. a) Cyclic voltammogram of oxygen alone (black), DMPZ with no oxygen present (red), and DMPZ (blue) under an O₂ atmosphere in TEGDME electrolyte. b) Cyclic voltammogram of DMPZ in DMSO electrolyte without (blue) and with (red) the chemically synthesized oxygen radicals. (Inset: ESR signal of the chemically generated oxygen radicals.) c) Cyclic voltammogram of DMPZ in different electrolytes of TEGDME and DMSO under an Ar atmosphere. The three electrodes compose of Pt counter and gold working electrodes with Ag/Ag⁺ in acetonitrile solution as a reference electrode. The scan rate was maintained at 100 mV s⁻¹. See Supplementary Note 7 for detailed discussion.

Figure 3-22. Discharge profiles of the cells with and without DMPZ catalyst in an oxygen atmosphere at a constant rate of 0.2 mA/cm². See Supplementary Note 8 for detailed discussion.

Figure 3-23. DEMS results of Li-O₂ cells during charge (a) with and (b) without DMPZ catalyst. Each cell was discharged to 1mAh and recharge to the same capacity at a current density of 0.2 mA cm⁻². See Supplementary Note 9 for detailed discussion.

Figure 3-24. Relationship between donor number of various non-aqueous solvents and Li/Li⁺ redox potential vs. SHE in each solvent. While the redox potential of Li/Li⁺ vs. SHE in TEGDME electrolyte was not precisely reported, it can be derived from the relationship between the donor number of solvent and Li/Li⁺ redox potential in each solvent. The redox potential of Li/Li⁺ vs. SHE in TEGDME can be interpolated

to around -2.9 V, which is similar to that in water. See Supplementary Note 9 for detailed discussion.

List of Tables

Table 2-1. Calculated conductivity of discharge products using single overbinding correction energy and separately applied overbinding correction energy.

Table 2-2. Calculated surface energies of low index surfaces. All possible terminations were considered. The spin-polarized generalized gradient approximation (GGA) type calculation was conducted using density functional theory (DFT). Perdew-Burke-Ernzerhof exchange-correlation parameterization was used. The overbinding energy of oxygen corrected from reaction $\text{Li}_2\text{O} + 1/2\text{O}_2 \rightarrow \text{Li}_2\text{O}_2$. The surface free energy was calculated from energy difference between bulk phase and surface structure, $\gamma = \frac{1}{2A} [G_{slab} - G_{bulk}] = \frac{1}{2A} [G_{slab} - N_O \mu_O^{bulk} - N_M \mu_M^{bulk}]$ where G_{slab}/G_{bulk} , N_M/N_O and $\mu_M^{bulk}/\mu_O^{bulk}$ indicate Gibbs free energy of surface structure/bulk phase, the number of metal/oxygen atom and chemical potential of metal and oxygen in bulk phase. Both maximum and minimum value of chemical potential, which were derived from M-O phase diagram, were considered for surface calculation of each phase. All possible terminations of low index surfaces were investigated to construct Wulff shape. A convergence test of the vacuum and slab thicknesses indicated that a vacuum thickness of 10 Å and slab thickness > 20 Å were sufficient for convergence within 1 meV/Å² for the surface energies. More detailed computational condition and formulation can be found in ref. 20 of manuscript.

Table 2-3. Major surfaces of discharge products, ratio of each surface in most oxidizing condition, and minimum OER barrier at each surface in LiO_2 , NaO_2 , Li_2O_2 and Na_2O_2 .

Table 2-4. Calculated concentration and hopping barrier of main charge carrier in LiO_2 , NaO_2 , Li_2O_2 and Na_2O_2 . Electronic and ionic conductivities were calculated from information of positive charge carrier p^+ and negative charge carrier V_M^- , respectively.

Table 2-5. Concentration of various defects in NaO_2 and Na_2O_2 at Fermi energy, which is taken to the point which satisfies charge neutrality.

Table 2-6. Concentration of various defects in LiO_2 and Li_2O_2 at Fermi energy, which is taken to the point which satisfies charge neutrality.

Table 2-7. Electronic coupling constant (V_{AB}), adiabatic activation barrier (v_{eff}), effective frequency of motion, and adiabaticity (γ) values of each polaron hopping barrier in LiO_2 , NaO_2 , Li_2O_2 , and Na_2O_2 .

Table 3-1. Donor number of various non-aqueous solvents and Li/Li^+ redox potential vs. SHE in each solvent.

Table 3-2. Experimental and calculated redox potential of RM candidates. See Supplementary Note 1 for detailed discussion.

Table 3-3. Various RM candidates for Li-O₂ batteries.

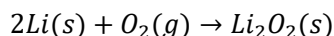
Chapter 1. General Introduction

1.1 Introduction to metal-air battery

Due to growing demands of large energy storage applications such as electric vehicles (EVs) and energy storage systems (ESSs), development of battery systems with high energy density and low cost as well as environmental sustainability is becoming intensive.[1] Lithium ion batteries (LIBs) have powered portable devices during recent decades,[2] however, they are predicted to be unable to supply future demands because of their limited energy density and high production cost.[3, 4] Current LIBs usually exploit transition-metal-oxide (TMO) cathode materials (*e.g.*, cobalt or nickel oxides), which is limited and concentrated in certain (sometimes conflict-prone) countries.[4] In addition, transition metal elements in TMO is much heavier than other elements, *e.g.* 58.93 g/mol for cobalt, 6.94 and 16.00 g/mole for lithium and oxygen respectively, limiting energy density of battery.

Metal-air batteries (MABs) are one of the most promising post-LIB system, which exploit direct reaction of metal (*e.g.* Li, Na, K, Al, ...) and gas molecule (O_2 , CO_2 , SO_2 , ...). Due to exclusion of transition metal, the energy density of MABs are ~10 times higher than conventional TMO-based LIBs.[5, 6] For example, the energy density of lithium-oxygen batteries, which is most intensively studied MAB system, exhibits exceptionally high energy density up to $\sim 3000 \text{ Wh kg}^{-1}$. [7] Figure 1-1 shows schematics for desired reaction of lithium-oxygen batteries. During discharge, lithium

metal in anode is oxidized to Li^+ ion, and oxygen molecules is reduced in carbon cathode which provides reaction site, forming solid discharge product, Li_2O_2 . The overall reaction can be written as:



Charge process is reverse reaction of discharge, *i.e.* decomposition of Li_2O_2 into Li metal and O_2 gas. Reaction chemistries of different metal and gas combinations are also formation and decomposition of solid product, similar to the lithium-oxygen system.[5, 6] This seemingly simple reaction of MAB was suggested as merit, however, it has been reported that side reactions involving an intermediate products and cell components occur complicatedly during MAB operation.[8, 9] Furthermore, the energy efficiency of MAB is generally low due to insulating discharge products, hindering it from practical use.[10, 11] To improve reversibility and energy efficiency of MAB, fundamental understandings on discharge product and reaction chemistry are essential, as well as careful engineering of cell components. In chapter 2, we focused on fundamental property of discharge products of lithium-oxygen batteries and sodium-oxygen batteries, *i.e.* theoretical overpotential of OER, ionic/electronic conductivity, and dissolution energy for each product, investigating the origin of high charging overpotential. Chapter 3 discusses desired reaction and side reaction of soluble catalyst, which usually used to lower charging overpotential, suggesting design principles for soluble catalyst with theoretical and experimental evidences.

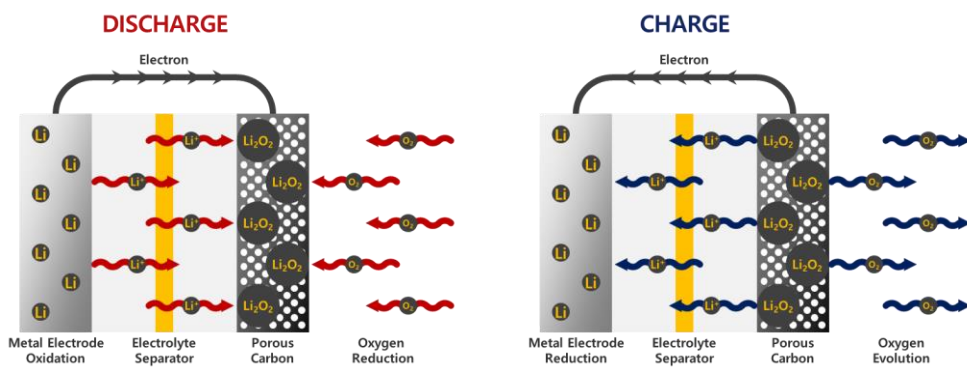


Figure 1-1. Reaction mechanism of lithium-oxygen batteries.

1.2 Introduction to density functional theory calculation

Density functional theory (DFT) calculation is one of the most widely used prediction tool in material science. The merit of DFT calculation is its high accuracy for large variety of materials, with no need of any empirical parameter, for which it is called as “first principles” or “*ab-initio*” calculation.[12] These features originated from time-dependent Schrödinger equation, *viz.*,

$$H\Psi = E\Psi$$

where H is Hamiltonian operator, Ψ is the wave function, and E is the total energy of the system. The Hamiltonian operator H is expressed as follows:

$$H = -\sum_{i=1}^N \frac{1}{2} \nabla_i^2 - \sum_{i=1}^M \frac{1}{2M_A} \nabla_A^2 - \sum_{i=1}^N \sum_{A=1}^M \frac{Z_A}{r_{iA}} + \sum_{i=1}^N \sum_{j>i}^N \frac{1}{r_{ij}} + \sum_{A=1}^M \sum_{B>A}^M \frac{Z_A Z_B}{R_{AB}}$$

The first and second terms concern kinetic operators of electrons and nuclei, respectively, while the third, fourth, and fifth terms account the interaction of particles, *i.e.* nuclei-electrons, electrons-electrons, and nuclei-nuclei, respectively. With nuclear charges and numbers of electrons as input information in Hamiltonian, electronic structure, which defines material property, and total energy of the system can be derived by solving the equation. Basically, the Schrödinger equation cannot be solved in multi-electron system, because of theoretical limit on expressing the interaction term. However, with assumptions such as Born-Oppenheimer approximation and electron mean-field approximation, the equation can be solved by iterative methodology. (Hartree-Fock method)

Hartree-Fock method considers wave function of all electrons, $3n$ degree of freedoms should be calculated, thus its computational cost become unacceptably high when the number of electron in the system increases. DFT remarkably decrease computational cost by treating electrons as “electron density”, of which degree of freedom is only 3, instead of $3n$. In DFT, the ground state energy can be expressed as follows:

$$E[\rho] = T[\rho] + V_{ee}[\rho] + \int \rho(\vec{r}) V_{Ne}(\vec{r}) d\vec{r}$$

where ρ is density, each term represents kinetic energy, electron-electron interaction, and Coulomb potential between electron and nuclei. As shown in above equation, whole equation can be expressed in the functional of density, for which the methodology is called as “density functional theory”.

In this paper, two types of DFT calculation tool were used. Calculations for bulk solid materials with periodic unit cell were performed by Vienna *ab initio* simulation package (VASP),[13] with a plane-wave basis set. Both DFT and Heyd-Scuseria-Ernzerhof (HSE) level of theory were conducted. Molecular materials floated in vacuum or dissolved in electrolyte were calculated by Gaussian09 package[14] with B3LYP level of theory (hybrid functional) and triple zeta valence polarization (TZVP) basis set.

1.3 References

- [1] Armand, M.; Tarascon, J. M., Building better batteries. *Nature* **2008**, 451, (7179), 652-657.
- [2] Julien, C.; Mauger, A.; Vijn, A.; Zaghib, K., Lithium Batteries. In *Lithium Batteries: Science and Technology*, Springer International Publishing: Cham, 2016; pp 29-68.
- [3] Etacheri, V.; Marom, R.; Elazari, R.; Salitra, G.; Aurbach, D., Challenges in the development of advanced Li-ion batteries: a review. *Energy & Environmental Science* **2011**, 4, (9), 3243-3262.
- [4] Nitta, N.; Wu, F.; Lee, J. T.; Yushin, G., Li-ion battery materials: present and future. *Materials Today* **2015**, 18, (5), 252-264.
- [5] Lim, H.-D.; Lee, B.; Bae, Y.; Park, H.; Ko, Y.; Kim, H.; Kim, J.; Kang, K., Reaction chemistry in rechargeable Li-O₂ batteries. *Chemical Society Reviews* **2017**, 46, (10), 2873-2888.
- [6] Hartmann, P.; Bender, C. L.; Sann, J.; Durr, A. K.; Jansen, M.; Janek, J.; Adelhelm, P., A comprehensive study on the cell chemistry of the sodium superoxide (NaO₂) battery. *Physical Chemistry Chemical Physics* **2013**, 15, (28), 11661-11672.
- [7] Bruce, P. G.; Freunberger, S. A.; Hardwick, L. J.; Tarascon, J.-M., Li-O₂ and Li-S batteries with high energy storage. *Nat Mater* **2012**, 11, (1), 19-29.
- [8] Freunberger, S. A.; Chen, Y.; Peng, Z.; Griffin, J. M.; Hardwick, L. J.; Bardé, F.; Novák, P.; Bruce, P. G., Reactions in the Rechargeable Lithium–O₂ Battery with

Alkyl Carbonate Electrolytes. *Journal of the American Chemical Society* **2011**, 133, (20), 8040-8047.

[9] Bryantsev, V. S.; Giordani, V.; Walker, W.; Blanco, M.; Zecevic, S.; Sasaki, K.; Uddin, J.; Addison, D.; Chase, G. V., Predicting Solvent Stability in Aprotic Electrolyte Li-Air Batteries: Nucleophilic Substitution by the Superoxide Anion Radical ($O_2^{\cdot -}$). *Journal of Physical Chemistry A* **2011**, 115, (44), 12399-12409.

[10] Lim, H.-D.; Park, K.-Y.; Song, H.; Jang, E. Y.; Gwon, H.; Kim, J.; Kim, Y. H.; Lima, M. D.; Robles, R. O.; Lepró, X.; Baughman, R. H.; Kang, K., Enhanced Power and Rechargeability of a Li–O₂ Battery Based on a Hierarchical-Fibril CNT Electrode. *Advanced Materials* **2013**, 25, (9), 1348-1352.

[11] Lim, H.-D.; Song, H.; Kim, J.; Gwon, H.; Bae, Y.; Park, K.-Y.; Hong, J.; Kim, H.; Kim, T.; Kim, Y. H.; Lepró, X.; Ovalle-Robles, R.; Baughman, R. H.; Kang, K., Superior Rechargeability and Efficiency of Lithium–Oxygen Batteries: Hierarchical Air Electrode Architecture Combined with a Soluble Catalyst. *Angewandte Chemie International Edition* **2014**, 53, (15), 3926-3931.

[12] Dong-Hwa Seo, I. P., Kisuk Kang, *Electrochemically Enabled Sustainability: Devices, Materials and Mechanisms for Energy Conversion (Chapter 6. First-Principles Approach for Cathode Design and Characterisation)*. CRC Press: 2014.

[13] Kresse, G.; Furthmüller, J., Efficient iterative schemes for ab initio total-energy calculations using a plane-wave basis set. *Physical Review B* **1996**, 54, (16), 11169-11186.

[14] Frisch, M.; Trucks, G.; Schlegel, H.; Scuseria, G.; Robb, M.; Cheeseman, J.; Scalmani, G.; Barone, V.; Mennucci, B.; Petersson, G., Gaussian 09 Revision D. **2009**, 01.

Chapter 2. Theoretical evidence for low charging overpotentials of superoxide discharge products in metal-oxygen batteries

(The content of this chapter has been published in *Chemistry of Materials*. Reproduced with permission from [Lee, B et al., *Chemistry of Materials* **2015**, 27, (24), 8406-8413.] Copyright (2015) American Chemical Society)

2.1 Introduction

Recently, Li–oxygen and Na–oxygen batteries have been studied extensively because of their high theoretical energy density relative to current Li-ion batteries in response to increasing demand for large-scale energy storage applications such as electric vehicles.[1-4] Although Li and Na exhibit similar chemical properties, an apparent distinction in the electrochemical properties of Li–oxygen and Na–oxygen batteries has been reported. The most important issue is the high charging overpotential (over 1 V) required in Li–oxygen cells to decompose the discharge product Li_2O_2 in the carbon electrode without a catalyst.[2, 5, 6]. In contrast, significantly lower charging overpotentials of Na–oxygen cells (~ 0.2 V) have been reported, with the discharge products consisting mainly of NaO_2 . [7, 8] Although the origin of this discrepancy remains poorly understood, recent experimental observations revealed that some Li–oxygen cells with LiO_2 as the discharge product

exhibited a charging overpotential lower than 0.5 V even without catalysts.[9] Furthermore, a Na–oxygen cell with Na₂O₂ as a discharge product unexpectedly suffered from a high overpotential of ~1 V.[10-12] These contradicting observations suggest a correlation between the various discharge products and corresponding overpotentials.

Herein, we investigated the physical and chemical differences among the discharge products of Li–oxygen and Na–oxygen batteries, LiO₂, Li₂O₂, NaO₂, and Na₂O₂, with respect to three possible origins of the overpotentials. Among the several stages that can contribute to the overpotentials, the (i) charge transport in each phase, (ii) oxygen releasing step from the phase, and (iii) dissolution/ionization of the phase in the electrolyte were mainly considered (See Figure 2-1). As the discharge products are known to be semiconducting to insulating,[13-15] the different ionic and electronic conductivities of the products may be one factor causing the discrepancies in the charging overpotentials.[13-15] Similarly, as the oxygen evolution reaction (OER) kinetics have been widely recognized as the rate-determining step of the reactions in fuel cells and water-splitting devices,[16, 17] the OER *via* $M_xO_2 \rightarrow x \cdot M^+ + O_2 + x \cdot e^-$ (M = Na or Li) can differ significantly among discharge products because of the crystal structures and corresponding metal–oxygen or oxygen–oxygen bonding characters.[18-20] Moreover, as recently proposed by many researchers,[21-25] a solution-mediated reaction can occur through dissolved species such as M_xO₂ molecules or M⁺ and O₂^{x-} ions. In this case, the dissolution kinetics of the discharge

products may be an important contributor to the charging overpotentials. Based on a comparative analysis of the discharge products with respect to these factors, in this study, we observed that the intrinsic nature of superoxides is much more preferable for the charging kinetics than that of peroxides regardless of the use of Li or Na. Our theoretical research on the various decomposition mechanisms of the discharge products provides insights into designing high-efficiency metal–oxygen batteries.

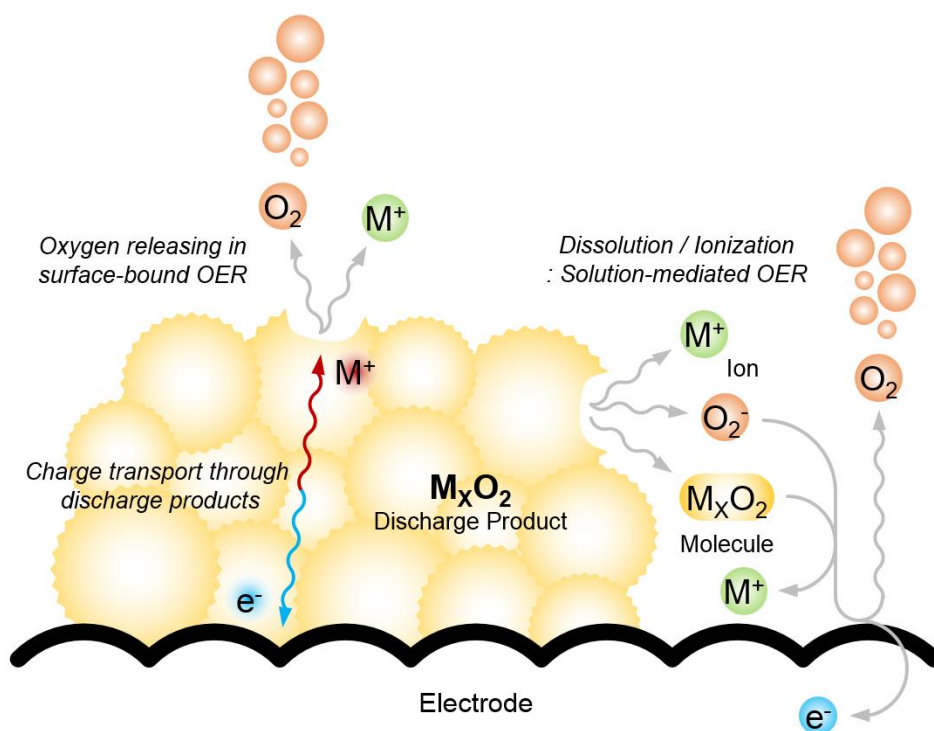


Figure 2-1. Suggested mechanisms for OER in metal-oxygen batteries

2.2 Computational details

2.2.1 Conductivity calculations

Energy calculations of the given states of materials were conducted using spin-polarized Heyd–Scuseria–Ernzerhof (HSE)–type first principle calculations[26, 27] using density functional theory (DFT). The Vienna *ab initio* simulation package (VASP)[28] was used with projector-augmented wave pseudopotentials.[29] We used a plane-wave basis with an energy cutoff of 500 eV and a Monkhorst–Pack $1 \times 1 \times 1$ k -point mesh. All the structures were fully relaxed. A mixing coefficient (α) of 0.48 was selected for the HSE hybrid calculation, which was calculated by matching the bandgap of Li_2O_2 to the results of G_0W_0 and self-consistent GW -type calculations.[13] It was confirmed that the value of $\alpha=0.48$ compensated for the overbinding energy of oxygen in various oxides, which will be discussed later. The supercell size of $3 \times 2 \times 3$, $2 \times 2 \times 2$, $3 \times 3 \times 2$ and $2 \times 2 \times 2$ was used for LiO_2 , NaO_2 , Li_2O_2 and Na_2O_2 respectively, which contains 108, 96, 144 and 108 atoms in the cell. The selected cutoff energy and k -point mesh ensure that the total energies converged within 7 meV per formula unit.

The formation energy of defect X of charge state q was calculated using the following formulation:[30]

$$E_f(X^q) = E_0(X^q) - E_0(\text{bulk}) - \sum_i n_i \mu_i + q\varepsilon_F + E_{MP1} \quad (1)$$

where n_i is the number of i defects; μ_i is the chemical potential of species i in an equilibrium state, ε_F is the Fermi energy; and E_{MP1} is the Makov–Payne monopole

size correction,[30, 31] which was calculated to be 0.014, 0.014, 0.170, and 0.306 for LiO_2 , NaO_2 , Li_2O_2 , and Na_2O_2 , respectively. The chemical potential of Li (μ_{Li}) or Na (μ_{Na}) ions was set to the energy level of metallic Li or Na, which is at dynamic equilibrium with the applied potential:[32]

$$\mu_M = \mu_M(\text{metal}) - eU \quad (2)$$

Here, eU is the applied potential, which was set to the calculated equilibrium potential, U_{eq} (3.07, 2.78, 3.11, and 2.46 V for LiO_2 , NaO_2 , Li_2O_2 , and Na_2O_2 , respectively). When addressing the oxygen chemical potential, however, note that DFT fails in calculating the exact energy of oxygen bonding, known as the oxygen overbinding error. Figure 2-2 shows the relationship between the experimental and calculated formation enthalpy. Ideally, the two formation enthalpies should be identical, as represented by the dashed line in the figure; however, all the points are located above the dashed line, which indicates that the calculation overestimated the chemical potential of oxygen in the gas phase. A slope of 1.003 and y-intercept of 0.468 were obtained by fitting the enthalpy data of various oxides, and, accordingly, we obtained a corrected oxygen chemical potential by compensating $E_{\text{correct}} = 0.468 \text{ eV}$ per oxygen atom. A previous work performed using the generalized gradient approximation (GGA) approach reported a slope lower than 1,[19] most likely due to the self-interaction error of GGA calculations. To obtain a slope of 1, Kang et al.[33] separately plotted the data of oxides, peroxides, and superoxides, resulting in different correction energies for each group. Obtaining a slope of 1 in this study implies that

the calculation condition (HSE, $\alpha=0.48$) properly predicts the oxygen binding energy of whole oxides; hence, various oxides can be compared in the same level of theory. Finally, the chemical potential of oxygen in the gas phase at standard state was obtained using the following equation:

$$\mu_{O_2}^0(298K, 1 \text{ atm}) = \frac{1}{2}(E_{O_2}^{calc} + 2E_{correct} - TS_{O_2}^0) \quad (3)$$

where $S_{O_2}^0$ is the entropy of oxygen gas at standard state, which was obtained from experiments.[34] The method used to correct the oxygen chemical potential with respect to the standard state can affect the resulting formation energy of defects. Yang et al.[14] reported V_{Na}^- and $V_{O_2}^+$ as the main charge carriers in the NaO_2 phase. In their work, the correction was performed based on the experimental formation enthalpy of NaO_2 .

For ion migration, the nudged elastic band (NEB) method[35] was adopted using GGA-type calculations because of the high computational cost of the NEB method using HSE. However, it has been reported that the selection of the functional does not significantly affect the hopping barrier derived using the NEB method.[13] For defect concentration analysis, the Fermi energy that satisfies charge neutrality was used, i.e., $E_f(V_M^-) = E_f(p^+)$. [13, 14, 36] For the defect mobility calculations, a hopping attempt rate of 10^{13} s^{-1} was used.[13, 37]

2.2.2 Dissolution properties of discharge products

Spin-polarized GGA-based first-principles calculations were conducted to determine the dissolution energies of the discharge products using continuum solvation modeling, VASPsol code.[38, 39] Solvated ions or molecules were located in a $12 \text{ \AA} \times 12 \text{ \AA} \times 12 \text{ \AA}$ cell to model isolated species. A plane-wave basis with an energy cutoff of 550 eV and Monkhorst–Pack $2 \times 2 \times 2$ k -point mesh was used. The total energies are ensured to be converged within 1 meV per formula unit, when the selected cutoff energy and k -point mesh is used. The solubility of the discharge products in the electrolyte was investigated in terms of the dissolution energy relative to the bulk phase, which can be expressed as:

$$\Delta E_{sol,mol} = E_{solvated}(M_x O_2) - E_{bulk}(M_x O_2) \quad (4)$$

where $E_{solvated}(M_x O_2)$ is the total energy of the solvated $M_x O_2$ molecule and $E_{bulk}(M_x O_2)$ is the energy of the bulk $M_x O_2$ per formula unit. Molecular $M_x O_2$ can also be solvated into an ionized form via the reaction $M_x O_2 \rightarrow x \cdot M^+ + O_2^{x-}$, where the dissolution energy formulation becomes

$$\Delta E_{sol,ion} = x \cdot E_{solvated}(M^+) + E_{solvated}(O_2^{x-}) - E_{bulk}(M_x O_2) \quad (5)$$

$E_{solvated}(M^+)$ and $E_{solvated}(O_2^{x-})$ are the total energies of the solvated M^+ ion and O_2^{x-} ion, respectively. We considered both the molecular and ionized cases in calculating the dissolution energy. The entropy effect was neglected in the calculation because the solvation entropy term (TS) of polar molecules (HF, HCl, and metal

halides) and ions was reported to be less than 5% of the enthalpy term in the standard state.[40, 41]

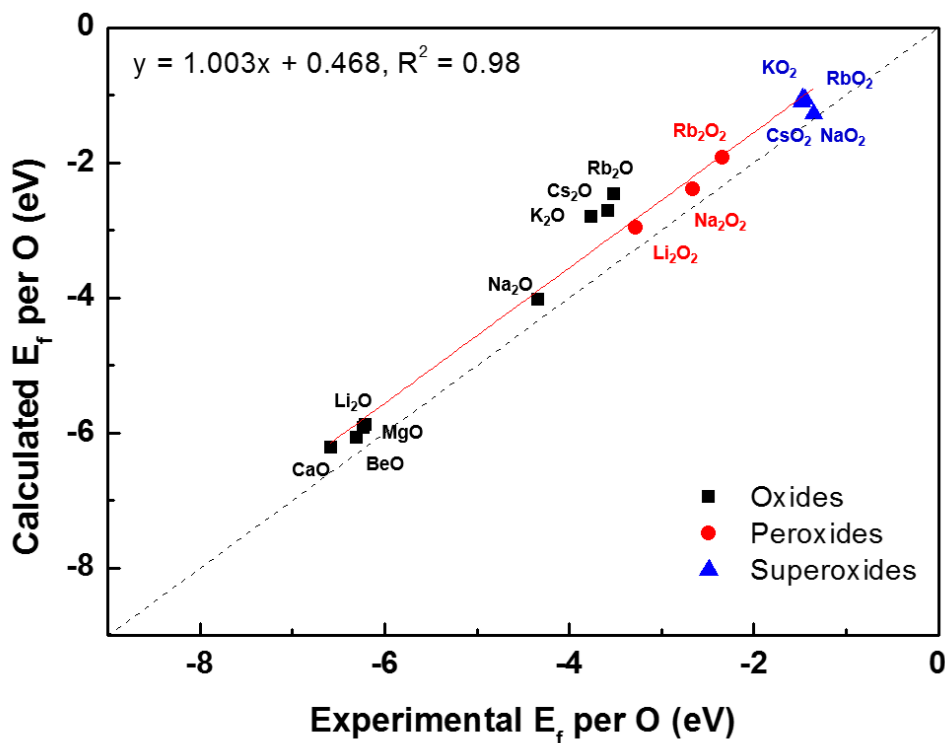


Figure 2-2. Formation energy per oxygen atom calculated in HSE ($\alpha=0.48$) at 0 K versus the formation enthalpy measured at standard state, 298 K and 1 atm. Black squares, red circles, blue triangles indicate oxides, peroxides, superoxides respectively. Black dash line shows exact correspondence between experiment and calculation, while red solid line is linear regression fitted to all data points which yields slope of 1.003 and y-intercept of 0.468. Note that separate fittings for oxides, peroxides, superoxides in the same data set result in overbinding correction of 0.590, 0.335, and 0.317 eV/O respectively. However, relative conductivity differences among the discharge products in this study were not largely changed (Table 2-1).

	Electronic conductivity (S/cm)		Ionic conductivity (S/cm)	
	Single overbinding correction	Separate overbinding correction	Single overbinding correction	Separate overbinding correction
LiO ₂	2×10^{-17}	1×10^{-19}	6×10^{-17}	3×10^{-19}
NaO ₂	4×10^{-17}	2×10^{-19}	3×10^{-9}	2×10^{-11}
Li ₂ O ₂	3×10^{-21}	3×10^{-22}	1×10^{-19}	1×10^{-20}
Na ₂ O ₂	2×10^{-19}	2×10^{-20}	3×10^{-20}	3×10^{-21}

Table 2-1. Calculated conductivity of discharge products using single overbinding correction energy and separately applied overbinding correction energy.

2.3 Result and Discussion

2.3.1 OER from crystalline surfaces

Figure 2-3 displays the schematic crystal structures of the discharge products reported in Li–oxygen and Na–oxygen batteries.[2, 7, 9, 10] All of the reported discharge products consist of 6-coordinated metal ions with oxygen dumbbell ions (O_2^{x-}) in their structures. Na ions occupy the octahedral sites in NaO_2 (pyrite, Pa-3) and the prismatic sites in Na_2O_2 . In Li_2O_2 , Li ions are present in both octahedral and prismatic sites, which exist as alternating layers in the structure. For the LiO_2 phase, the crystal structure has not yet been clearly verified. Nevertheless, various evidences for LiO_2 -like phases have been reported using Raman spectroscopy, EXAFS, and SQUID analysis.[42, 43] Especially, Zhai et al.[9] recently reported observation of the marcasite form of LiO_2 as a discharge product for a Li– O_2 cell. In addition, a theoretical study by Kang et al.[44] reported that marcasite LiO_2 is the most stable among various possible polymorphs. We also confirmed that marcasite LiO_2 phase becomes stable at oxygen partial pressure of > 25 atm (Figure 2-4), implying that this phase can formed in certain chemical condition. Note that all the discharge products contain oxygen dumbbell ions in their structure, which are known to be capable of accommodating electrons or holes in the O–O bond by altering the O–O bond length for the charge transfer.[13, 45, 46]

The decomposition kinetics to yield oxygen evolution from crystalline NaO_2 , Na_2O_2

and Li_2O_2 were theoretically studied previously.[20] We performed a similar calculation for the hypothetical marcasite LiO_2 phase to evaluate its OER capability. Based on the equilibrium particle shape constructed from calculated surface energies, the energy barrier of the OER was investigated at each stable surface (see Figures 2-5, 2-6, Table 2-2 and ref. 20 for detailed calculation methods). Table 2-3 lists the stable surfaces of the discharge products and compares their ratios in each phase and the corresponding OER energy barriers in the oxidizing condition. The OER barriers at major surfaces of the superoxides were revealed to be substantially lower than those for the peroxides (Na_2O_2 and Li_2O_2). In particular, the lowest OER barrier of ~ 160 meV was observed for one of the major surfaces in the marcasite LiO_2 . Furthermore, more than 95% of the crystalline surfaces of the LiO_2 exhibited OER barriers of less than ~ 320 meV. This value is significantly smaller than those of most of the surfaces in the other discharge products, indicative of the facile oxygen evolution from the LiO_2 phase. The generally lower barriers in superoxides are attributed to the weaker metal–oxygen bonds in the structure; the weaker electrostatic attraction between M and O due to the lower oxidation states of $\text{O}_2^{\text{x-}}$ in superoxides would require a lower energy penalty to lose the oxygen from the structure.[20]

Moreover, the number of charge transfer steps can also affect the kinetics of OER. For the evolution of one O_2 molecule, superoxide phases require one electron charge transfer step, while peroxides require two steps. The typically sluggish nature of multi-electron reaction with respect to the one-electron reaction of superoxides can

slow down the charging kinetics of peroxides. This general observation indicates that the intrinsic OER of superoxide phases would be more facile than those of peroxide phases assuming the absence of the charge transport limitation (electronic/ionic conductivity).

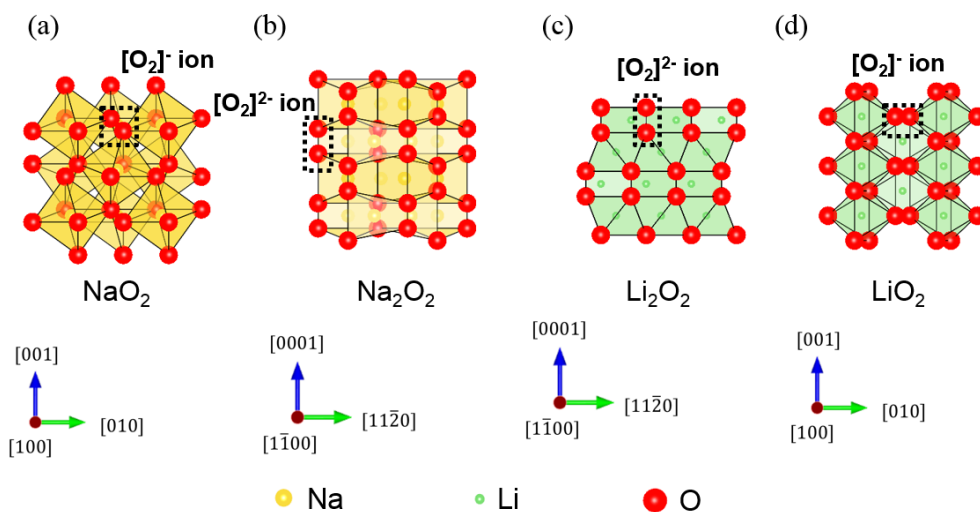


Figure 2-3. Crystal structure of (a) pyrite NaO_2 , (b) Na_2O_2 , (c) Li_2O_2 and (d) LiO_2 . Yellow, green and red atoms represent sodium, lithium, oxygen respectively. Black box with dash line indicates oxygen dumbbell ion (O_2^{n-}) in the structure.

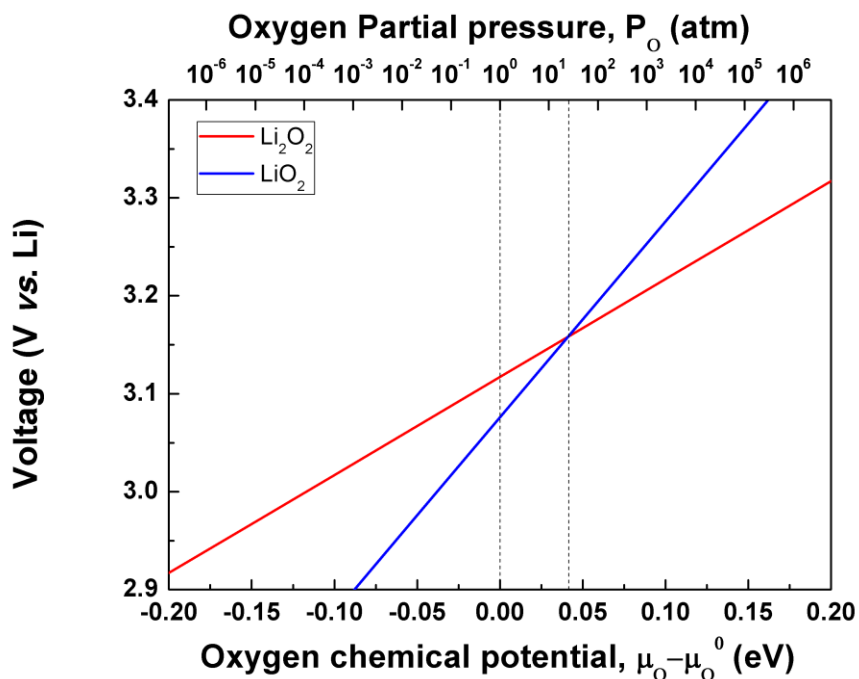


Figure 2-4. Relationship between cell voltage and oxygen partial pressure, in the Li/O₂ cell. Higher cell voltage is related with more negative Gibbs free energy, according to Nernst equation; $\mu_{Li} - \mu_{Li}^0 = -nFE_{cell}$, where μ_{Li} is chemical potential of metal Li in structure, μ_{Li}^0 is chemical potential of pure metal, n is the number of charge of metal ion, F is faraday constant, E_{cell} is the voltage of the cell. HSE functional was used for energy calculation. LiO₂ becomes more stable than Li₂O₂ in about 25 atm of oxygen partial pressure.

$$\gamma = \frac{1}{2A} [G_{slab} - G_{bulk}] = \frac{1}{2A} [G_{slab} - N_O \mu_O^{bulk} - N_M \mu_M^{bulk}]$$

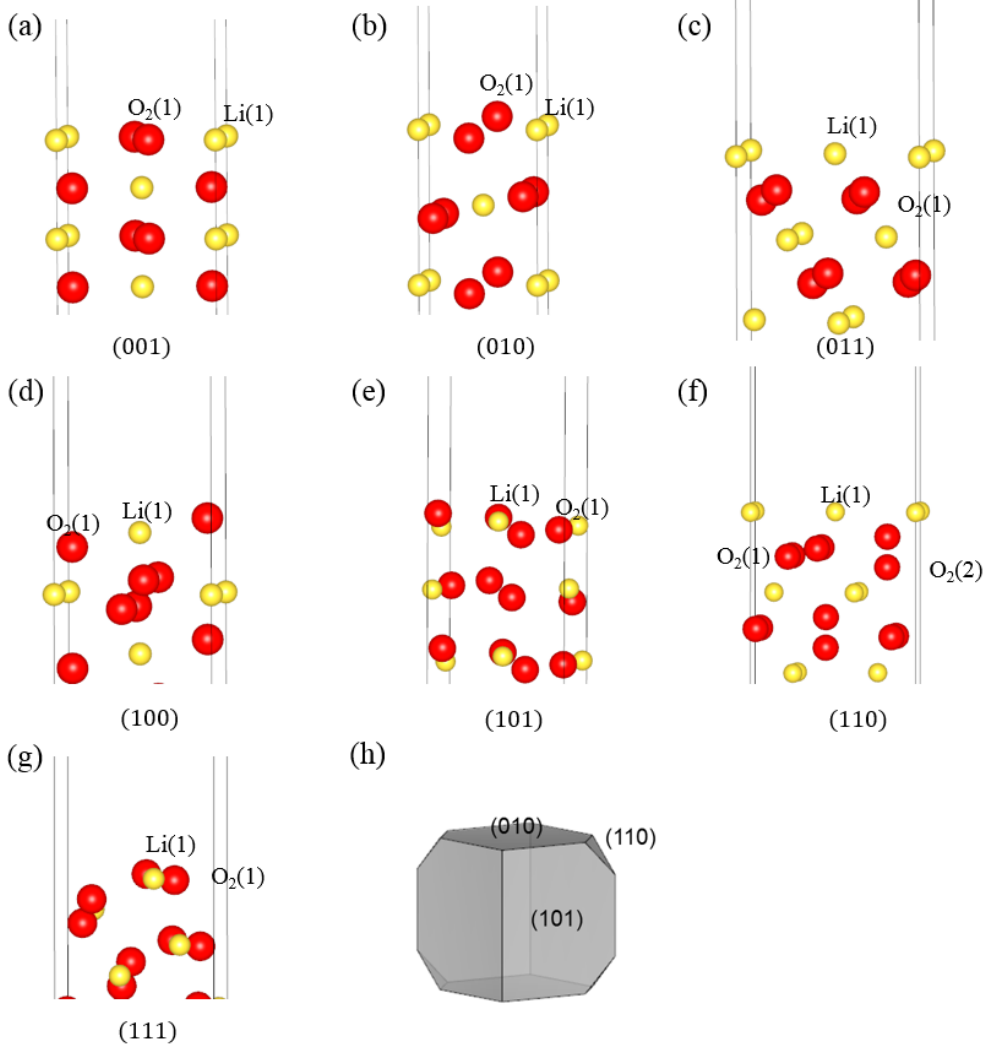


Figure 2-5. (a-g) The low index surface structures of LiO_2 and their terminations. (h) Wulff shape of LiO_2 was constructed from calculated surface energies. For surface energy calculations, a slab/vacuum geometry composed of repeating slabs and vacuum layers was adopted.

Orientation	Termination	Li ₂ O ₂ limit	O ₂ limit
(001)	O ₂ (1)-Li(1)*	31	31
	O ₂ (1)	47	53
	Li(1)	71	64
(010)	O ₂ (1)-Li(1)*	22	22
	O ₂ (1)	24	35
	Li(1)	221	210
(011)	O ₂ (1)-Li(1)	57	51
	O ₂ (1)	45	51
(100)	O ₂ (1)-Li(1)*	36	36
	O ₂ (1)	29	37
	Li(1)	58	50
(101)	O ₂ (1)-Li(1)*	18	18
	O ₂ (1)	17	28
	Li(1)	152	142
(110)	Li(1)-O ₂ (1)-O ₂ (2)	39	32
	O ₂ (1)-O ₂ (2)	38	45
	O ₂ (1)*	34	34
	O ₂ (2)*	29	29
(111)	O ₂ (1)-Li(1)*	25	25
	O ₂ (1)	27	32
	Li(1)	63	58

Table 2-2. Calculated surface energies of low index surfaces. All possible terminations were considered. The spin-polarized generalized gradient approximation (GGA) type calculation was conducted using density functional theory (DFT). Perdew-Burke-Ernzerhof exchange-correlation parameterization was used. The overbinding energy of oxygen corrected from reaction $\text{Li}_2\text{O} + 1/2\text{O}_2 \rightarrow \text{Li}_2\text{O}_2$. The surface free energy was calculated from energy difference between bulk phase and surface structure, $\gamma = \frac{1}{2A} [G_{\text{slab}} - G_{\text{bulk}}] = \frac{1}{2A} [G_{\text{slab}} - N_{\text{O}}\mu_{\text{O}}^{\text{bulk}} - N_{\text{M}}\mu_{\text{M}}^{\text{bulk}}]$ where $G_{\text{slab}}/G_{\text{bulk}}$, $N_{\text{M}}/N_{\text{O}}$ and $\mu_{\text{M}}^{\text{bulk}}/\mu_{\text{O}}^{\text{bulk}}$ indicate Gibbs free energy of surface structure/bulk phase, the number of metal/oxygen atom and chemical potential of metal and oxygen in bulk phase. Both maximum and minimum value of

chemical potential, which were derived from M-O phase diagram, were considered for surface calculation of each phase. All possible terminations of low index surfaces were investigated to construct Wulff shape. A convergence test of the vacuum and slab thicknesses indicated that a vacuum thickness of 10 Å and slab thickness > 20 Å were sufficient for convergence within 1 meV/Å² for the surface energies. More detailed computational condition and formulation can be found in ref. 20 of manuscript.

$$\Delta G = \frac{1}{2} [E_{step} - E_{initial} + \Delta N_O \cdot \mu_O^0 + \Delta N_{Li} \cdot (\mu_{Li}^0 - eU)]$$

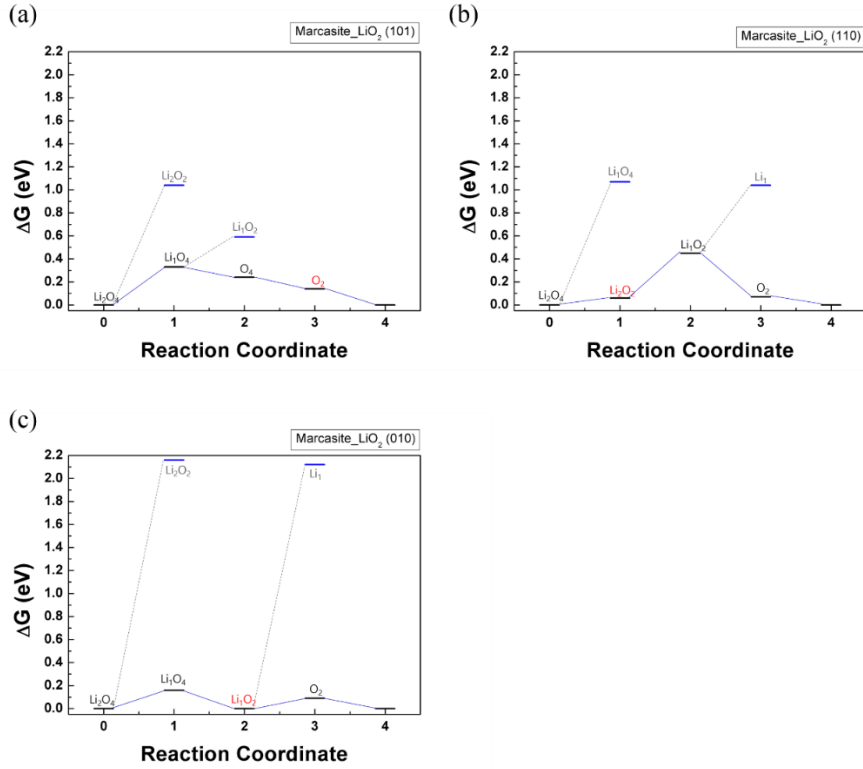


Figure 2-6. OER energy profile of LiO_2 under the calculated equilibrium potential $U = 2.76$ V, in (a) (101) surface, (b) (110) surface and (c) (111) surface. During the OER, oxygen or metal atoms leave the surface upon charging. In the situation, two sequences are possible; the metal ion extraction which is the electrochemical reaction (black) or the oxygen molecule evolution, the chemical reaction (red). The energies of the intermediate steps of the OER were calculated by removing metal ions or oxygen molecules from the surface. One OER cycle can be modeled by considering the atoms in the surface of the unit cell.

Species	Major surface	Surface ratio	OER barrier (eV)
LiO ₂ (marcasite)	(101)	68.5%	0.32
	(010)	27.8%	0.16
	(110)	3.7%	0.45
*NaO ₂ (pyrite)	(100)	79.2%	0.77
	(111)	12.1%	0.38
	(110)	8.7%	0.31
*Li ₂ O ₂	(11 $\bar{1}$ 00)	56.2%	1.97
	(0001)	34.6%	0.90
	(112 $\bar{1}$)	9.2%	0.50
*Na ₂ O ₂	(11 $\bar{1}$ 01)	70.2%	0.88
	(11 $\bar{1}$ 00)	17.9%	0.97
	(112 $\bar{0}$)	9.4%	0.88
	(0001)	2.5%	0.83

* Reference 20

Table 2-3. Major surfaces of discharge products, ratio of each surface in most oxidizing condition, and minimum OER barrier at each surface in LiO₂, NaO₂, Li₂O₂ and Na₂O₂.

2.3.2. Charge transport in discharge products

The IR polarization can be one of the contributors to the overpotential as a result of the insulating nature of the discharge products.[13, 46-48] In particular, in high-current-density charging of cells or if the size of the discharge products is appreciably large, the IR polarization can be rate-determining and build up a large overpotential value. The intrinsic conducting properties of the crystalline discharge products were estimated to compare their transport characteristics in the cells. In our calculations, a defect-mediated conduction model was adopted for the discharge products because of their large band gaps (see computational methods and Figure 2-7).[13, 14]

The defect-mediated conductivity can be expressed as a function of the defect concentration (C) and its mobility as follows:[49]

$$\sigma = C \times \text{mobility} = C \times \frac{va^2e^2}{k_BT} e^{\frac{-E_b}{k_BT}} \quad (6)$$

where E_b , v , and a are the energy barrier of hopping defects, hopping attempt rate, and hopping length, respectively. The value of C can be estimated using the following equation:[50]

$$C = N_{sites} e^{\frac{-E_f}{k_BT}} \quad (7)$$

where N_{sites} and E_f are the number of possible defect sites per unit volume and their formation energy. E_f of the various defects such as vacancies and polarons were calculated for LiO_2 , NaO_2 , Li_2O_2 , and Na_2O_2 using equations (1), (2), and (3). In all

the structures, the most stable negative defect was observed to be V_M^- ($M=Li, Na$), and the most stable positive defect was the hole polaron (p^+). Upon the formation of a hole in the peroxides, the oxygen dumbbell was reduced from O_2^{2-} to O_2^- with its length shrinking from 1.46 to 1.31 Å, indicating the formation of the hole polaron. For the hole formation in superoxides, O_2^- oxidizes to $O_2^{\delta-}$ ($\delta \approx 0$) with a bond length reduction from 1.29 to 1.20 Å, which is comparable to that of O_2 , ~1.19 Å. This similar nature to O_2 would lead to preferred oxygen evolution upon the formation of hole polarons in superoxides. The formation energies of the main charge carriers (V_M^- and p^+) were determined to be 0.6, 0.4, 0.9, and 0.8 eV for LiO_2 , NaO_2 , Li_2O_2 , and Na_2O_2 , respectively (Figure 2-8), demonstrating the generally lower defect formation energy in the superoxides. Based on the given formation energy of each charge carrier, the concentration could be calculated, and the results are presented in Table 2-4. The calculated concentrations of the main charge carriers (V_M^- and p^+) were $\sim 10^8$ sites/cm³ for Na_2O_2 and Li_2O_2 , whereas those of NaO_2 and LiO_2 were significantly higher at $\sim 10^{16}$ sites/cm³ and $\sim 10^{11}$ sites/cm³, respectively, because of the lower defect formation energies in the superoxides. The concentrations of the other defects are also provided in Tables 2-5 and 2-6.

The hopping barriers of the major defects, V_M^- and p^+ , were calculated using NEB methods to estimate the mobilities of the charge carriers, and the results are presented in Table 2-4 (see Figures 2-9 and 2-10 for details). Since polaron hopping in LiO_2 , NaO_2 , Li_2O_2 , and Na_2O_2 is adiabatic, polaron hopping barrier can be calculated in

plane-wave based calculation. (See details for Supplementary note 1) Although no notable differences were observed between the superoxides and peroxides with respect to the hopping barrier, the ion hopping (V_M^-) was generally faster than the electronic hopping (p^+). In NaO_2 , the ionic hopping barrier was particularly lower than that of p^+ , implying the dominant ionic charge transport mechanism. Using the calculated concentrations and mobilities of the main charge carriers (V_M^- and p^+), we estimated the ionic and electronic conductivities using equation (6); these values are tabulated in Table 2-4 for all the discharge products. The electronic conductivities of Li_2O_2 , Na_2O_2 , and NaO_2 were comparable in magnitudes, ranging from an order of 10^{-19} to 10^{-21} S/cm. The concentrations and mobilities of p^+ were similar among the peroxide phases, *i.e.*, Na_2O_2 and Li_2O_2 . NaO_2 exhibited a much higher p^+ concentration; however, its low mobility resulted in an electronic conductivity comparable to that of the other phases. Among the discharge products, the electronic conductivity of LiO_2 was slightly higher, $\sim 10^{-18}$ S/cm, with a relatively high carrier concentration and low hopping barrier.

Unlike the electronic conductivities, notable differences were observed in the ionic conductivities among the phases. The ionic conductivities of the superoxides were significantly higher than those of the peroxides, with NaO_2 and LiO_2 exhibiting nearly 11 and 3–4 orders of magnitude higher ionic conductivities, respectively, than those of Na_2O_2 and Li_2O_2 . The higher ionic conductivities in the superoxides are attributed primarily to the higher concentration of ionic defects compared with the peroxides.

Note that the calculated conductivities for Li_2O_2 , NaO_2 , and Na_2O_2 agree well with those reported in previous theoretical studies.^[13-15] The small differences in the conductivity values are most likely due to the use of a different α and oxygen reference. These results imply that superoxide phases exhibit intrinsically more efficient transport behaviors than peroxide phases because of their high charge carrier concentration.

When an overpotential η is applied to a discharge product, equation (2) becomes

$$\mu_M = \mu_M(\text{metal}) - e(U_{eq} + \eta) \quad (8)$$

where U_{eq} is the equilibrium potential. The increase in the overpotential shifts the chemical potential of the metal to lower values, resulting in further stabilization of V_M^- and p^+ defects. For example, an overpotential of 0.5 V causes the concentration of the main charge carriers to increase by a factor of 16,000; thus, the conductivity is enhanced by the same ratio. As indicated by the red dashed line in Figure 2-11, Li_2O_2 or Na_2O_2 require overpotentials above 1.1 V to become as conductive as NaO_2 . This result agrees well with the experimental observation by Hartmann et al.,^[7] who reported that the charging overpotential of Na– O_2 cell is lower by 1 V than that of a Li– O_2 cell with the same cell configuration. The same calculation for the LiO_2 phase implies that the formation of LiO_2 in the cell instead of Li_2O_2 can reduce the charging overpotential by roughly 0.4 V, which arises from the differences in the conductivity.

We note that most discharge products will allow some degree of metal vacancies

upon the initial charging process maintaining the pristine structure ($\text{Li}_{1-x}\text{O}_2$, $\text{Li}_{2-x}\text{O}_2$, $\text{Na}_{2-x}\text{O}_2$, or $\text{Na}_{1-x}\text{O}_2$). When created, a metal deficiency would significantly increase the number of charge carriers, correspondingly affect the formation of adjacent defects and greatly increasing the conductivities of the discharge phases. Kang et al. proposed that a metal-deficient phase, *i.e.*, $\text{Li}_{2-x}\text{O}_2$, can form during the charging of Li–oxygen cells because the oxygen evolution process is likely to be substantially slower than the extraction of Li or Na ions.[20, 44] We also confirmed that a metal-deficient phase of discharge products ($\text{Li}_{2-x}\text{O}_2$, $\text{Na}_{2-x}\text{O}_2$, or $\text{Na}_{1-x}\text{O}_2$, $0.03 < x < 0.04$) could be easily formed with a small amount of overpotential (< 0.05 V) (Figure 2-12); hence, the concentration of charge carriers is sensitively affected by the operating environment such as the charging current density. In this respect, the intrinsic conductivities of the pristine discharge phases should be carefully considered based on their contribution to the overpotential. In addition, the amount of deficiency in the dynamic equilibrium or its solubility limit in each phase should be determined for the precise estimation of the conductivities of discharge products in operating cells.

The position of the Fermi energy of discharge products can also be shifted in the dynamic equilibrium. Previous researches[46, 47, 51] reported that the Fermi energy of Li_2O_2 was calculated to be pinned at 0.35 eV above the VBM by the unoccupied LiO_2 (oxygen-rich surfaces) states, in the vicinity of the electrolyte. Due to the Fermi energy shift driven by the dynamic equilibrium, the concentration of hole polaron in Li_2O_2 structure increases, which can result in the enhancement of ionic conductivity.

The position of Fermi energy in dynamic equilibrium is affected by the band alignment between cell component and surface electronic structure of M_xO_2 . Therefore, the electronic properties of cell component, i.e. electrolytes and air electrodes, should also be considered for the determination of the exact position of the Fermi level, which can significantly alter the charge transfer mechanism. Nevertheless, the conductivity enhancement by dynamic equilibrium is governed by the intrinsic defect formation energy and defect hopping barrier; thus, the intrinsic conductivities of the discharge products serve as an appropriate basis for further discussion.

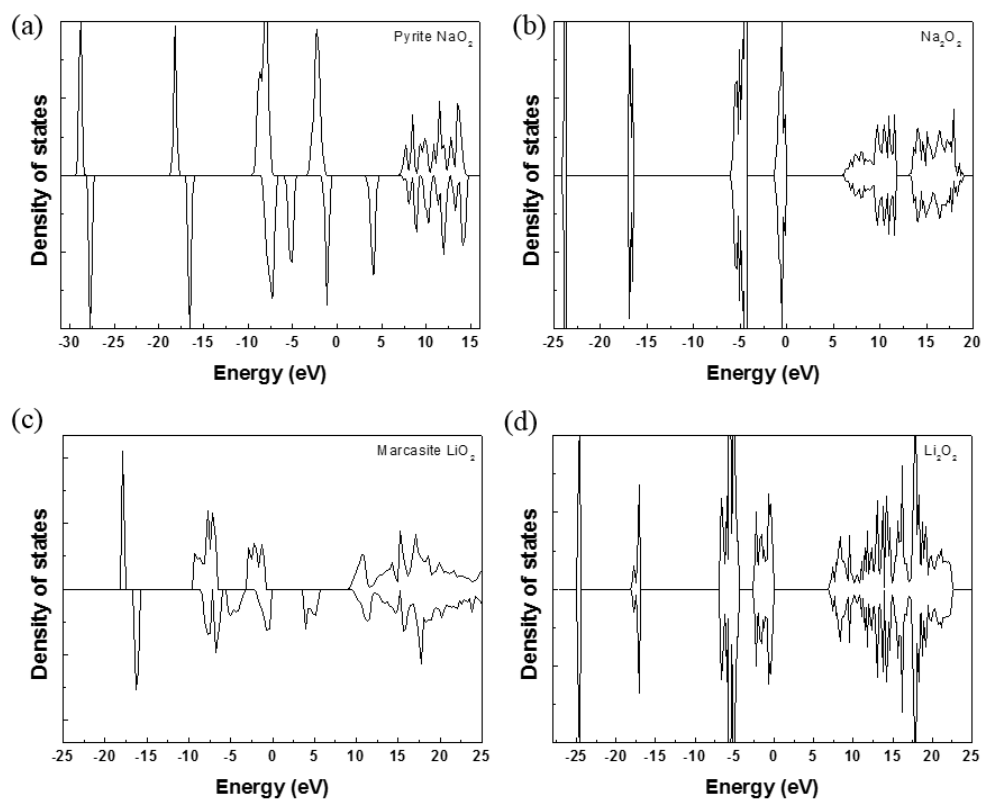


Figure 2-7. Density of state (DOS) of intrinsic (a) NaO_2 , (b) Na_2O_2 , (c) LiO_2 and (d) Li_2O_2 , calculated with HSE hybrid functional. Mixing coefficient (α) was chosen as 0.48. Calculated bandgap was 3.3, 5.8, 3.7 and 6.8 eV for NaO_2 , Na_2O_2 , LiO_2 and Li_2O_2 respectively.

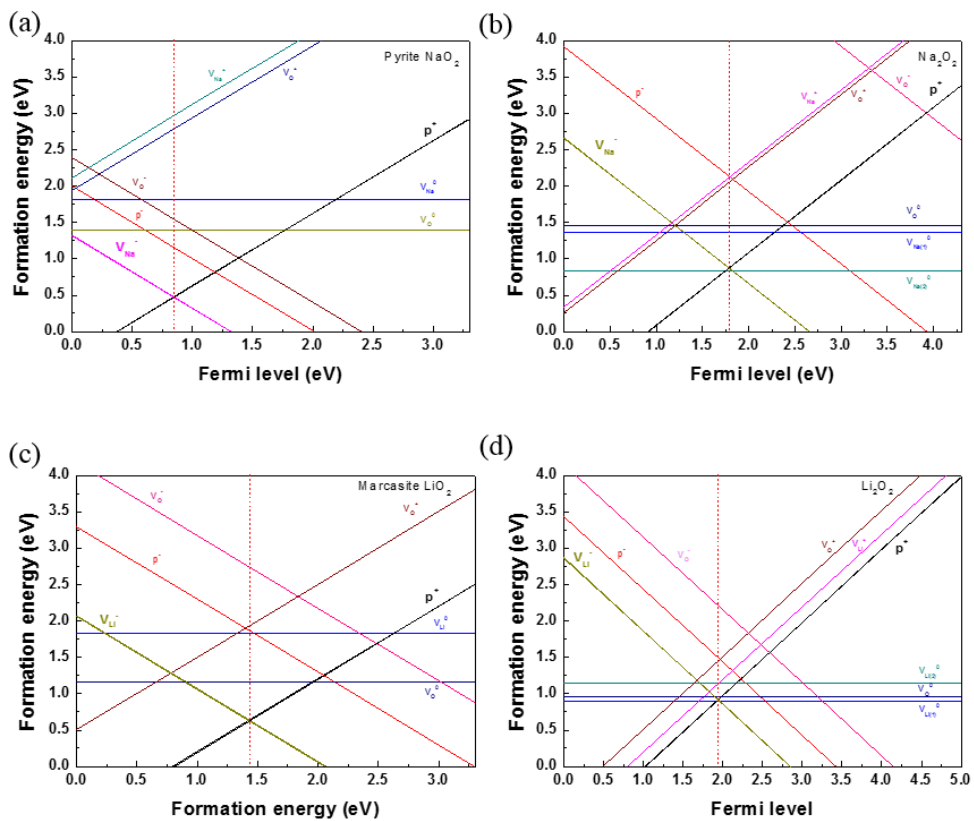


Figure 2-8. Formation energies of low energy defects in (a) NaO_2 , (b) Na_2O_2 , (c) LiO_2 and (d) Li_2O_2 versus Fermi energy. Red dash line is Fermi energy which satisfies charge neutrality.

Species	Defect	Concentration	Hopping barrier	Conductivity (S/cm)
LiO ₂	p ⁺ (electronic)	4.6×10 ¹¹	0.59	3×10 ⁻¹⁸
	V _M ⁻ (ionic)	4.6×10 ¹¹	0.51	6×10 ⁻¹⁷
NaO ₂	p ⁺ (electronic)	2.2×10 ¹⁶	0.81	4×10 ⁻¹⁷
	V _M ⁻ (ionic)	2.2×10 ¹⁶	0.34	3×10 ⁻⁹
Li ₂ O ₂	p ⁺ (electronic)	1.6×10 ⁷	0.51	3×10 ⁻²¹
	V _M ⁻ (ionic)	1.6×10 ⁷	0.41	1×10 ⁻²⁰
Na ₂ O ₂	p ⁺ (electronic)	2.3×10 ⁸	0.47	2×10 ⁻¹⁹
	V _M ⁻ (ionic)	2.3×10 ⁸	0.50	3×10 ⁻²⁰

Table 2-4. Calculated concentration and hopping barrier of main charge carrier in LiO₂, NaO₂, Li₂O₂ and Na₂O₂. Electronic and ionic conductivities were calculated from information of positive charge carrier p⁺ and negative charge carrier V_M⁻, respectively.

NaO_2	Concentration (sites/cm ⁻³)	Na_2O_2	Concentration (sites/cm ⁻³)
p^+	2.2.E+16	p^+	2.3E+08
p^-	1.7.E+01	p^-	7.0E-15
$\text{V}(\text{Na})^0$	3.2.E-05	$\text{V}(\text{Na})^0$	3.4E+09
$\text{V}(\text{Na})^+$	1.1.E-22	$\text{V}(\text{Na})^+$	3.4E-12
$\text{V}(\text{Na})^-$	2.2.E+16	$\text{V}(\text{Na})^-$	2.3E+08
$\text{V}(\text{O})^0$	2.2.E-01	$\text{V}(\text{O})^0$	1.8E-02
$\text{V}(\text{O})^+$	4.7.E-23	$\text{V}(\text{O})^+$	6.9E-12
$\text{V}(\text{O})^-$	9.4.E-06	$\text{V}(\text{O})^-$	5.6E-65
$\text{V}(\text{Na})^{2+}$	2.8.E-33	$\text{V}(\text{Na})^{2+}$	7.4E-33
$\text{V}(\text{Na})^{2-}$	1.6.E-21	$\text{V}(\text{Na})^{2-}$	8.0E-71
$\text{V}(\text{O})^{2+}$	9.5.E-26	$\text{V}(\text{O})^{2+}$	2.8E-39
$\text{V}(\text{O})^{2-}$	4.7.E-22	$\text{V}(\text{O})^{2-}$	4.0E-126
Na_i^0	5.2.E-17	Na_i^0	2.8E-39
Na_i^+	3.5.E+04	Na_i^+	1.8E-44
Na_i^-	2.7.E-32	Na_i^-	1.0E-72
$\text{V}(\text{O}_2)^0$	1.3.E-34	$\text{V}(\text{O}_2)^0$	1.3E-86
$\text{V}(\text{O}_2)^+$	3.5.E-01	$\text{V}(\text{O}_2)^+$	1.0E-58
$\text{V}(\text{O}_2)^-$	5.3.E-62	$\text{V}(\text{O}_2)^-$	2.3E-118

Table 2-5. Concentration of various defects in NaO_2 and Na_2O_2 at Fermi energy, which is taken to the point which satisfies charge neutrality.

LiO₂	Concentration (sites/cm⁻³)	Li₂O₂	Concentration (sites/cm⁻³)
p⁺	4.6E+11	p⁺	1.6E+07
p ⁻	6.8E-10	p ⁻	3.2E+03
V(Li) ⁰	3.2E-09	V(Li) ⁰	3.4E+07
V(Li) ⁺	1.8E+22	V(Li) ⁺	2.8E-03
V(Li)⁻	4.6E+11	V(Li)⁻	1.6E+07
V(O) ⁰	1.1E+03	V(O) ⁰	4.6E+06
V(O) ⁺	1.3E-10	V(O) ⁺	2.7E+02
V(O) ⁻	3.3E-24	V(O) ⁻	3.1E-15
V(Li) ²⁺	-	V(Li) ²⁺	4.8E-16
V(Li) ²⁻	-	V(Li) ²⁻	5.0E-35
V(O) ²⁺	-	V(O) ²⁺	1.8E-22
V(O) ²⁻	3.7E-18	V(O) ²⁻	5.6E-46
Li _i ⁰	1.5E+00	Li _i ⁰	5.7E-28
Li _i ⁺	1.5E+02	Li _i ⁺	2.1E-41
Li _i ⁻	4.5E-02	Li _i ⁻	2.0E-43
V(O ₂) ⁰	2.6E-20	V(O ₂) ⁰	4.0E-90
V(O ₂) ⁺	4.2E+06	V(O ₂) ⁺	2.4E-96
V(O ₂) ⁻	2.5E-22	V(O ₂) ⁻	7.8E-158

Table 2-6. Concentration of various defects in LiO₂ and Li₂O₂ at Fermi energy, which is taken to the point which satisfies charge neutrality.

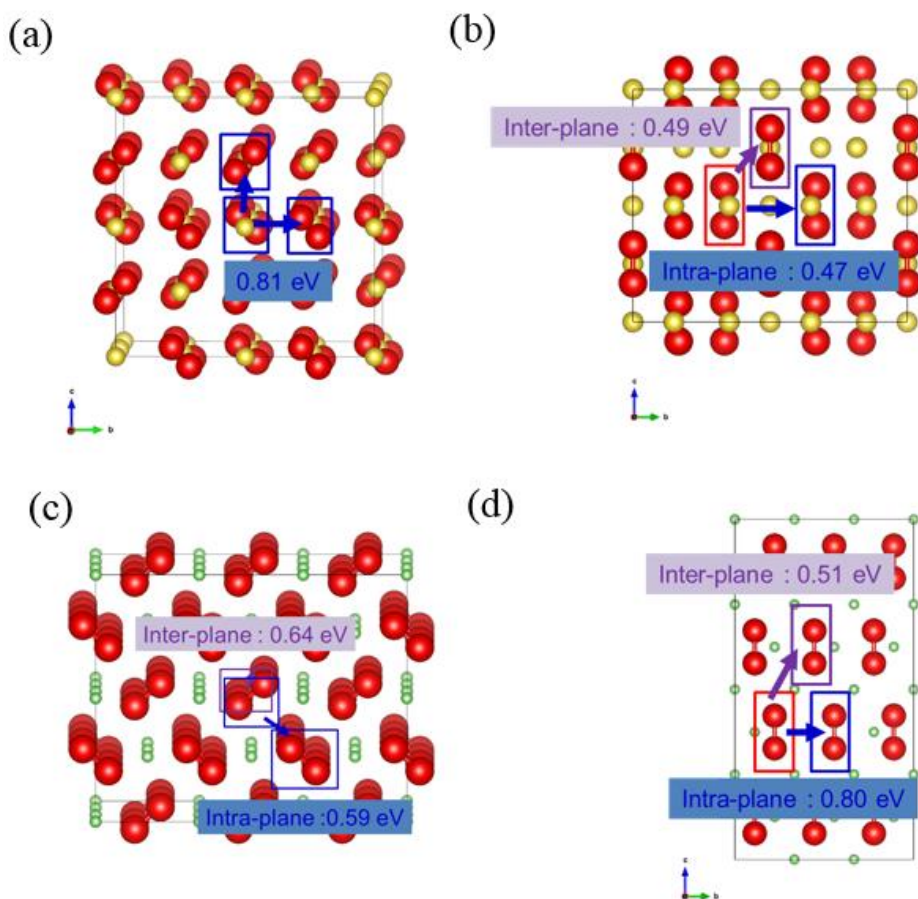


Figure 2-9. The hopping paths of hole and their hopping barrier in (a) NaO₂, (b) Na₂O₂, (c) LiO₂ and (d) Li₂O₂, calculated with HSE hybrid functional.

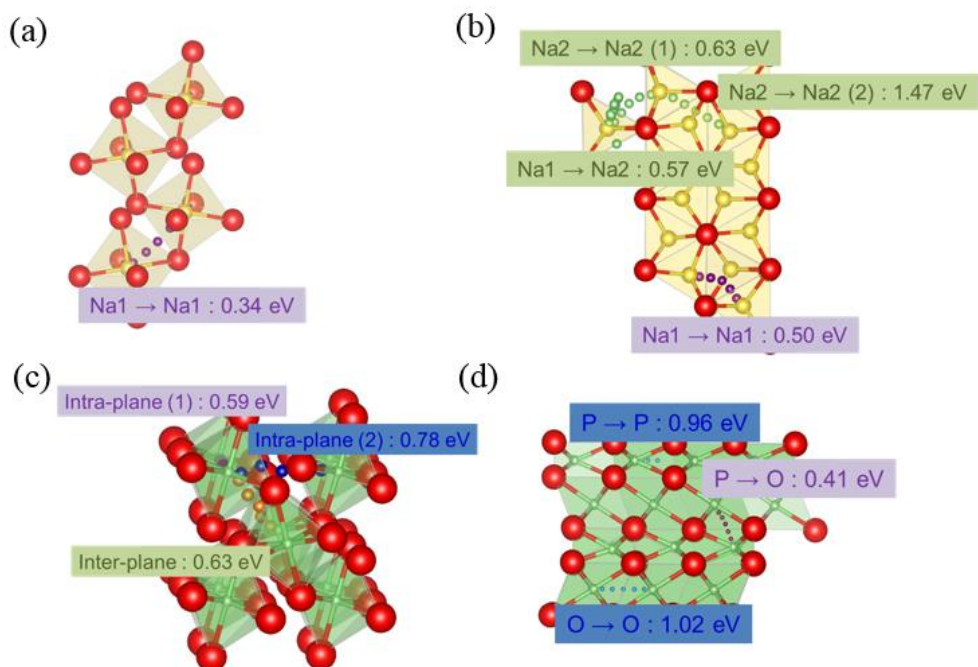


Figure 2-10. The hopping paths of negatively charged metal vacancy and their hopping barrier in (a) NaO_2 , (b) Na_2O_2 , (c) LiO_2 and (d) Li_2O_2 , calculated with GGA functional and NEB method.

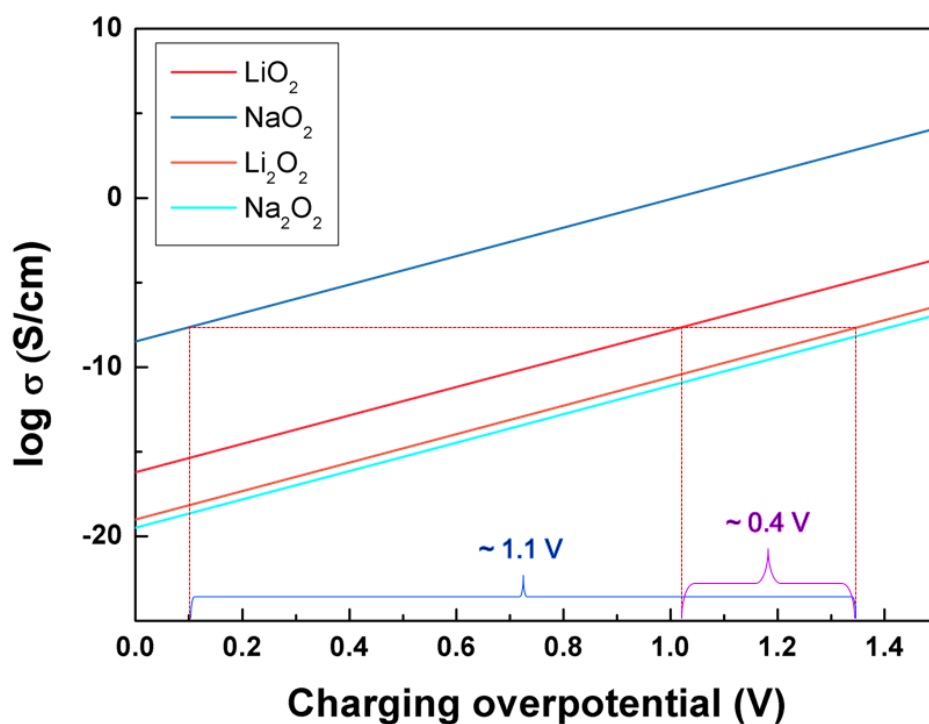


Figure 2-11. Increase of conductivity in logarithm as a function of applied charging overpotential. Red dash lines indicate that charging overpotential of 1.1 V and 0.7 V is required for Li_2O_2 and LiO_2 respectively, to reach same conductivity of NaO_2 with 0.1 V overpotential applied.

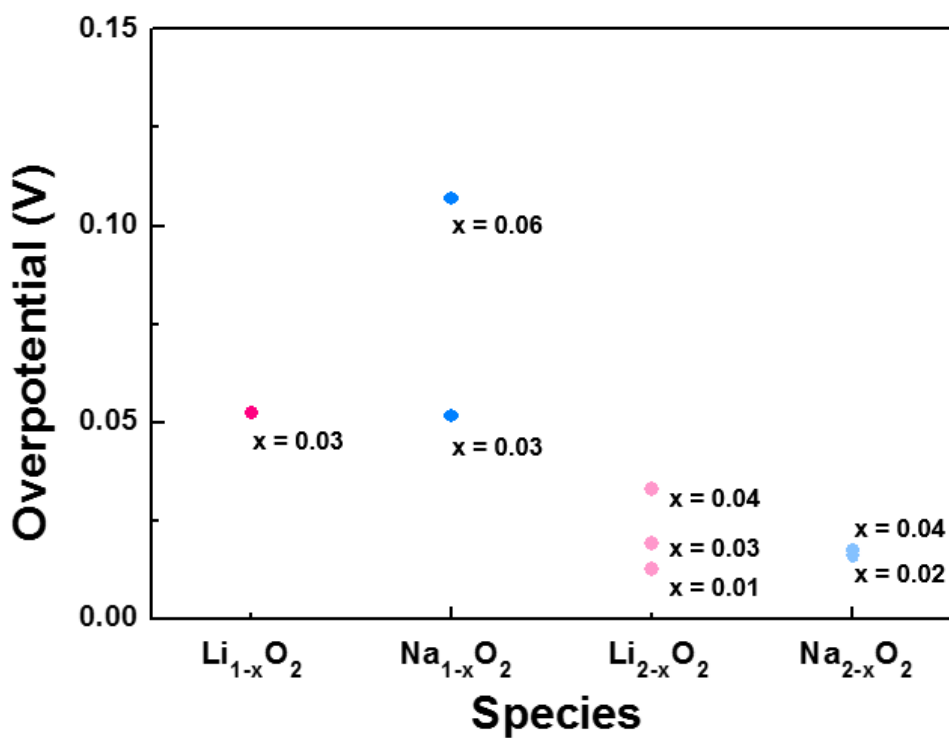


Figure 2-12. Required overpotential to form metal deficient phase of discharge product, $\text{Li}_{1-x}\text{O}_2$, $\text{Na}_{1-x}\text{O}_2$, $\text{Li}_{2-x}\text{O}_2$, $\text{Na}_{2-x}\text{O}_2$, $0.01 < x < 0.06$.

2.3.3 Dissolution of discharge products in the solution-based charging process

Recent studies proposed that the discharge product can be decomposed by a chemical dissolution process without a direct transfer of electrons through the discharge product.[21-25] In this case, the OER occurs at the interface between the air electrode and dissolved discharge products through a solution process mediated by the electrolyte. As illustrated in Figure 2-1, the discharge products must be dissolved into the electrolyte for the electrochemical reaction to occur via this process. To compare the different nature of discharge products under these circumstances, we investigated the tendency of dissolution of each discharge product in the electrolyte medium. Figure 2-13(a) plots the dissolution energies of each discharge product in the model electrolyte with a dielectric constant (ϵ) = 10, which is typical for the electrolytes used in metal–air batteries, such as ether-based electrolytes.[5-8, 52] Both molecular dissolution (red) and ionic dissolution (blue) were considered using equations (4) and (5), respectively. The dissolution energies of the peroxides were generally higher than those of the superoxides. Li_2O_2 and Na_2O_2 exhibited dissolution energies higher than 1.5 eV, whereas LiO_2 and NaO_2 exhibited relatively lower dissolution energies. In particular, the dissolution energy of NaO_2 was as low as 0.49 eV, which is expected to accelerate the solution-mediated process. The lower dissolution energy of NaO_2 is most likely due to the weak bonding nature of the metal and oxygen in the superoxides. As observed in Figure 2-2, the binding energies per oxygen of the discharge products were both experimentally and theoretically

evaluated to be $\text{Li}_2\text{O}_2 > \text{Na}_2\text{O}_2 > \text{NaO}_2$, which corresponds with the trend of the dissolution energy.

In Figures 2-13(b–c), the effect of the electrolyte solvent on the dissolution of the discharge products was further investigated. The dissolution energies of the discharge products decreased with increasing dielectric constant for both ionic and molecular dissolution processes. This phenomenon was due to the polar nature of all the discharge products, which are typically stabilized in polar solvents. In the ether-based solvents such as tetraglyme ($\epsilon=7.9$), diglyme ($\epsilon=7.7$) and dimethoxyethane ($\epsilon=7.2$), which were commonly used in metal–oxygen battery system,[5-8, 52] the dissolution does not significantly occur even in NaO_2 phase. As mentioned above, molecular dissolution energy of NaO_2 phase (0.49 eV) was the lowest among the discharge products in model solvents ($\epsilon=10$), which statistically corresponds to 1 molecule dissolution out of 10^8 formula units of bulk NaO_2 . However, as shown in Figure 2-13(b-c), the dissolution energy of NaO_2 remarkably decrease to 0.17 eV (1 molecule out of 1000 formula units of bulk) in $\epsilon=30$. It is well known that for solvents with low dielectric constant, the solution dielectric constant increases as the salt concentration increases, which can be well higher than that of the pure solvent.[53] This implies that although NaO_2 cannot dissolve into pure ether-based solvents, the dissolution of NaO_2 can occur when salts are present in the electrolyte, resulting in a solution-mediated process. In a highly polar solvent such as dimethyl sulfoxide ($\epsilon \approx 50$), the molecular and ionic dissolution energies of NaO_2 significantly decrease to 0.06 and

0.18 eV, respectively, which statistically corresponds to the dissolution of one molecule out of 10 and 1,000 formula units of the bulk phase, thus further accelerating the solution-mediated process. Moreover, at higher dielectric medium, the energy difference between molecular and ionic dissolutions become negligibly small, which would lead to the higher possibility of the ionic dissolution. The increased ionic dissolution would promote the oxidation process at the air electrode by skipping the dissociation step of the molecular NaO_2 , which would result in a low charging overpotential. Nevertheless, the ionic dissolution of NaO_2 implies that oxygen radicals should exist during charging and even in steady state, which may bring about the continuous decomposition of the electrolyte and corresponding formation of byproducts such as $\text{Na}_2\text{O}_2 \cdot 2\text{H}_2\text{O}$. This idea is consistent with previous experimental observations of $\text{Na}_2\text{O}_2 \cdot 2\text{H}_2\text{O}$ often being produced in Na–oxygen cells after discharge.^{22, 46, 47} The results imply that using an electrolyte with a higher dielectric constant can further promote the solution-mediated process; however, the liberation of oxygen radicals is also expected to lead to faster degradation of the solvents. Thus, the trade-off between energy efficiency and electrolyte stability works along with the polarity of solvents. Moreover, recent study[54] reported that the trade-off also works on the discharging process. The researchers reported that high ionic dissolution of LiO_2 could improve discharge capacity through the solution-mediated process, while dissolved species simultaneously accelerate side reaction of solvents. Therefore, these trade-offs should be considered when selecting an electrolyte.

We note that the property of solvent cannot be solely defined by dielectric constants. In this study, the chemical effects of solvents, i.e. donor number (DN) and acceptor number (AN) were not considered because evaluating DN/AN through first-principle calculation is highly challenging. However, the trend of calculated dissolution energies in this study well correspond to results in previous work by A. Ketan et al.,[54] which reported the ionic dissolution energy of LiO_2 calculated from the experimental DN/AN values (Figure 2-14). Accordingly, we believe that dielectric constant can be one meaningful property for predicting dissolution capability of discharge products. However, an explicit solvation model is still required for the exact calculation of dissolution energy, which should be studied in the future.

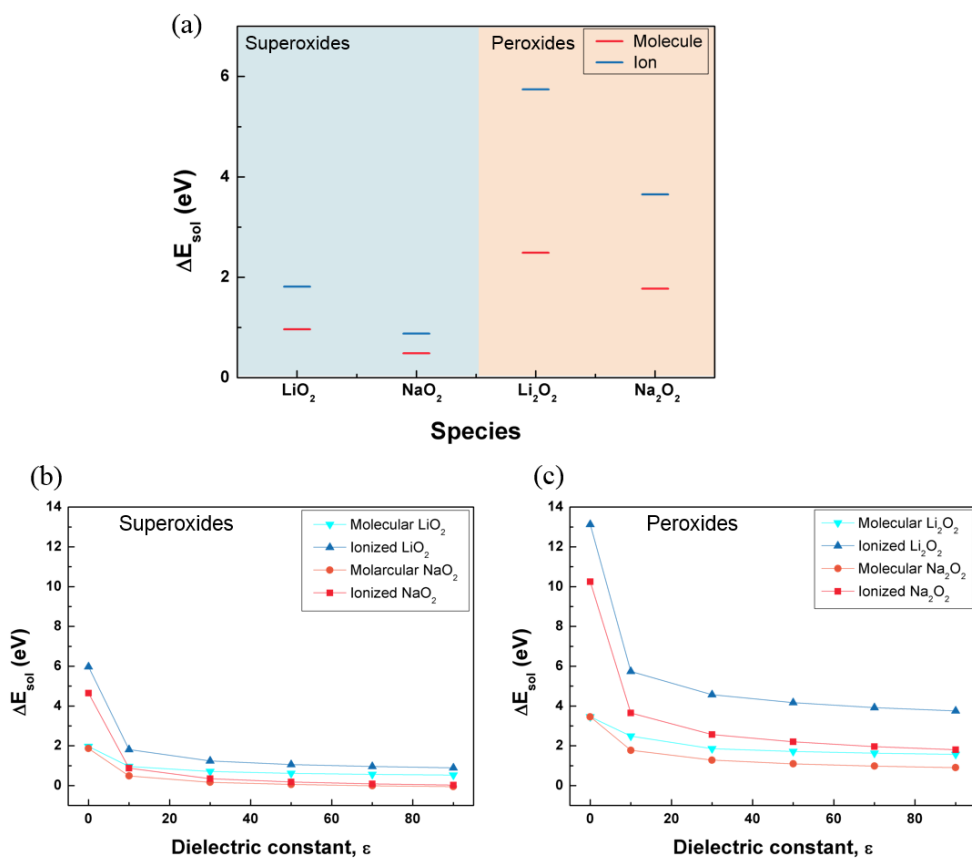


Figure 2-13. The dissolution energy of LiO_2 , NaO_2 , Li_2O_2 and Na_2O_2 . (a) in molecular and ionic form with respect to their bulk structure at dielectric constant (ϵ) = 10. The dielectric constant dependence of the dissolution energy in (b) superoxide species and (c) peroxide species were studied to investigate effect of different solvents.

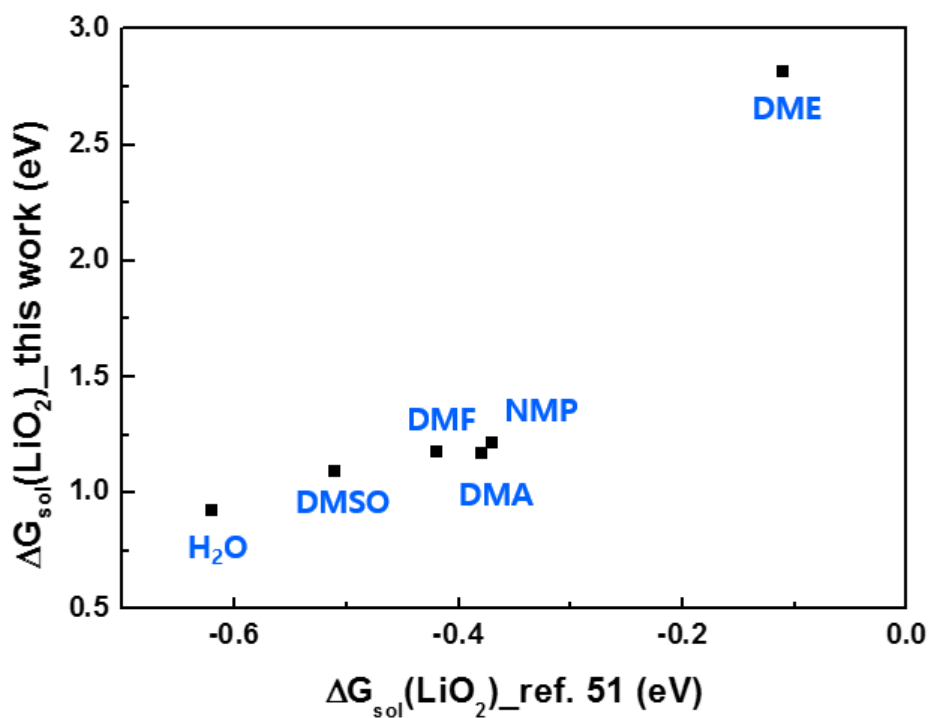


Figure 2-14. Relation between LiO₂ ion dissolution energy (vs. intermediate product LiO₂ at the surface) in ref. 51 and LiO₂ ion dissolution energy (vs. bulk LiO₂) in this study, calculated from interpolation of data in Figure 4(b), dielectric constants of 80.16 (H₂O), 46.45 (DMSO), 36.71 (DMF), 37.78 (DMA), 32.17 (NMP) and 7.2 (DME) were used.

2.3.4 Supplementary Notes

Supplementary Note 1. Polaron transfer barrier

Since hole polaron hopping is one of electron transfer reaction, its activation barrier should be calculated based on Marcus theory. [55] Marcus electron transfer scheme introduces two energy barrier, *i.e.* diabatic (non-adiabatic) and adiabatic activation barriers of electron transfer. If an electron transfer reaction is diabatic, rate of the reaction would be governed by Fermi's golden rule, while the reaction would be controlled by electron tunneling rate in case of adiabatic transfer. Adiabaticity of an electron transfer is determined by following equation,

$$\gamma = \frac{1}{\hbar v_{eff}} \left(\frac{\pi}{4\Delta G_{ad} kT} \right)^{\frac{1}{2}} V_{AB}^2$$

(9)

where ΔG_{ad} is the adiabatic activation energy, \hbar is Planck's constant, v_{eff} is the effective frequency for motion along the electron transfer direction, which can be estimated from a typical phonon frequency in the material, k is Boltzmann's constant, and V_{AB} is electronic coupling constant. Because the probability of adiabatic charge transfer is defined as $1 - \exp(-\gamma)$, the hopping with $\gamma \gg 1$ can be regarded as adiabatic and $\gamma \ll 1$ as diabatic. [56] It should be noted that, by using plane-wave based DFT calculation, we only can calculate adiabatic activation barrier, while further level of theory (e.g. local type hybrid DFT calculation with cluster model) is required for estimation of diabatic barrier. [57] Therefore, adiabaticity of polaron

hopping is worth being checked for LiO_2 , NaO_2 , Li_2O_2 , and Na_2O_2 . For estimation of V_{AB} , which is required in equation (9), following relation is exploited,

$$V_{AB} = \frac{1}{2} \Delta E_{12} \quad (10)$$

where energy difference ΔE_{12} will be evaluated from energy difference of the two gap states above and below the Fermi energy at the DOS of hopping transition state. Furthermore, v_{eff} values of discharge products were estimated from phonon frequency diagram in the literatures. [58,59] Table 2-7 summarizes V_{AB} , ΔG_{ad} , v_{eff} and γ values of each polaron hopping in LiO_2 , NaO_2 , Li_2O_2 , and Na_2O_2 . Calculated γ values of all discharge products show larger values than 1, which implies that all hoppings are adiabatic. Therefore, ΔG_{ad} values, which were calculated from plane-wave based calculation, can be used as hopping barrier of polaron.

Polaron path	V_{AB} (eV)	ΔG_{ad} (eV)	ν_{eff} (s⁻¹)	γ
NaO ₂	0.349	0.81	3.30 E+13 ^[33]	5
Na ₂ O ₂ intra	0.537	0.49	2.58 E+13 ^[33]	21
Na ₂ O ₂ inter	0.538	0.47	2.58 E+13 ^[33]	22
LiO ₂ intra	0.548	0.64	3.60 E+13 ^[37]	14
LiO ₂ inter	0.815	0.59	3.60 E+13 ^[37]	32
Li ₂ O ₂ intra	0.858	0.51	2.47 E+13	56
Li ₂ O ₂ inter	0.427	0.80	2.47 E+13	11

Table 2-7. Electronic coupling constant (V_{AB}), adiabatic activation barrier (ν_{eff}), effective frequency of motion, and adiabaticity (γ) values of each polaron hopping barrier in LiO₂, NaO₂, Li₂O₂, and Na₂O₂.

2.4 Conclusion

We investigated the intrinsic properties of the discharge products of metal–oxygen batteries with respect to their OER kinetics, conductivities, and dissolution properties in the electrolyte. Our calculations revealed that the superoxide discharge products, including the hypothetical LiO_2 , exhibited better OER efficiencies than the peroxide phases. Furthermore, the ionic conductivities of NaO_2 and LiO_2 were 11 and 4 orders higher than those of the peroxide phases, respectively. Even for the solution-mediated mechanism of charging, the dissolution energy of the superoxide phases was calculated to be lower than that of the peroxide phases and was particularly low for NaO_2 . Based on all the considered mechanisms, we believe that the formation of a superoxide discharge product is key to improving the energy efficiency of metal–oxygen batteries.

2.5 References

- [1] Abraham, K. M.; Jiang, Z., A Polymer Electrolyte-Based Rechargeable Lithium/Oxygen Battery. *Journal of the Electrochemical Society* **1996**, 143, (1), 1-5.
- [2] Freunberger, S. A.; Chen, Y.; Drewett, N. E.; Hardwick, L. J.; Bardé, F.; Bruce, P. G., The Lithium–Oxygen Battery with Ether-Based Electrolytes. *Angewandte Chemie International Edition* **2011**, 50, (37), 8609-8613.
- [3] Débart, A.; Bao, J.; Armstrong, G.; Bruce, P. G., *J. Power Sources* **2007**, 174, (2), 1177.
- [4] Bruce, P. G.; Freunberger, S. A.; Hardwick, L. J.; Tarascon, J. M., *Nat. Mater.* **2012**, 11, (1), 19.
- [5] Lim, H.-D.; Song, H.; Gwon, H.; Park, K.-Y.; Kim, J.; Bae, Y.; Kim, H.; Jung, S.-K.; Kim, T.; Kim, Y. H.; Lepro, X.; Ovalle-Robles, R.; Baughman, R. H.; Kang, K., A new catalyst-embedded hierarchical air electrode for high-performance Li-O₂ batteries. *Energy & Environmental Science* **2013**, 6, (12), 3570-3575.
- [6] Lim, H.-D.; Park, K.-Y.; Song, H.; Jang, E. Y.; Gwon, H.; Kim, J.; Kim, Y. H.; Lima, M. D.; Robles, R. O.; Lepró, X.; Baughman, R. H.; Kang, K., Enhanced Power and Rechargeability of a Li–O₂ Battery Based on a Hierarchical-Fibril CNT Electrode. *Advanced Materials* **2013**, 25, (9), 1348-1352.
- [7] Hartmann, P.; Bender, C. L.; Vračar, M.; Dürr, A. K.; Garsuch, A.; Janek, J.; Adelhelm, P., A rechargeable room-temperature sodium superoxide (NaO₂) battery. *Nat Mater* **2013**, 12, (3), 228-232.

- [8] Hartmann, P.; Bender, C. L.; Sann, J.; Durr, A. K.; Jansen, M.; Janek, J.; Adelhelm, P., A comprehensive study on the cell chemistry of the sodium superoxide (NaO₂) battery. *Physical Chemistry Chemical Physics* **2013**, 15, (28), 11661-11672.
- [9] Zhai, D.; Lau, K. C.; Wang, H.-H.; Wen, J.; Miller, D. J.; Lu, J.; Kang, F.; Li, B.; Yang, W.; Gao, J.; Indacochea, E.; Curtiss, L. A.; Amine, K., Interfacial Effects on Lithium Superoxide Disproportionation in Li-O₂ Batteries. *Nano Letters* **2015**, 15, (2), 1041-1046.
- [10] Liu, W.; Sun, Q.; Yang, Y.; Xie, J.-Y.; Fu, Z.-W., An enhanced electrochemical performance of a sodium-air battery with graphene nanosheets as air electrode catalysts. *Chemical Communications* **2013**, 49, (19), 1951-1953.
- [11] Li, Y.; Yadegari, H.; Li, X.; Banis, M. N.; Li, R.; Sun, X., Superior catalytic activity of nitrogen-doped graphene cathodes for high energy capacity sodium-air batteries. *Chemical Communications* **2013**, 49, (100), 11731-11733.
- [12] Hu, Y.; Han, X.; Zhao, Q.; Du, J.; Cheng, F.; Chen, J., Porous perovskite calcium-manganese oxide microspheres as an efficient catalyst for rechargeable sodium-oxygen batteries. *Journal of Materials Chemistry A* **2015**, 3, (7), 3320-3324.
- [13] Radin, M. D.; Siegel, D. J., Charge transport in lithium peroxide: relevance for rechargeable metal-air batteries. *Energy & Environmental Science* **2013**, 6, (8), 2370-2379.
- [14] Yang, S.; Siegel, D. J., Intrinsic Conductivity in Sodium–Air Battery Discharge Phases: Sodium Superoxide vs Sodium Peroxide. *Chemistry of Materials* **2015**, 27, (11), 3852-3860.

- [15] Araujo, R. B.; Chakraborty, S.; Ahuja, R., Unveiling the charge migration mechanism in Na₂O₂: implications for sodium-air batteries. *Physical Chemistry Chemical Physics* **2015**, 17, (12), 8203-8209.
- [16] Rossmeisl, J.; Logadottir, A.; Nørskov, J. K., Electrolysis of water on (oxidized) metal surfaces. *Chemical Physics* **2005**, 319, (1–3), 178-184.
- [17] Nørskov, J. K.; Bligaard, T.; Rossmeisl, J.; Christensen, C. H., Towards the computational design of solid catalysts. *Nat Chem* **2009**, 1, (1), 37-46.
- [18] Mo, Y.; Ong, S. P.; Ceder, G., First-principles study of the oxygen evolution reaction of lithium peroxide in the lithium-air battery. *Physical Review B* **2011**, 84, (20), 205446.
- [19] Hummelshøj, J. S.; Luntz, A. C.; Nørskov, J. K., Theoretical evidence for low kinetic overpotentials in Li-O₂ electrochemistry. *The Journal of Chemical Physics* **2013**, 138, (3), 034703.
- [20] Lee, B.; Seo, D.-H.; Lim, H.-D.; Park, I.; Park, K.-Y.; Kim, J.; Kang, K., First-Principles Study of the Reaction Mechanism in Sodium–Oxygen Batteries. *Chemistry of Materials* **2014**, 26, (2), 1048-1055.
- [21] Xia, C.; Black, R.; Fernandes, R.; Adams, B.; Nazar, L. F., The critical role of phase-transfer catalysis in aprotic sodium oxygen batteries. *Nat Chem* **2015**, 7, (6), 496-501.
- [22] Ortiz-Vitoriano, N.; Batcho, T. P.; Kwabi, D. G.; Han, B.; Pour, N.; Yao, K. P. C.; Thompson, C. V.; Shao-Horn, Y., Rate-Dependent Nucleation and Growth of NaO₂ in Na–O₂ Batteries. *The Journal of Physical Chemistry Letters* **2015**, 2636-

2643.

- [23] Johnson, L.; Li, C.; Liu, Z.; Chen, Y.; Freunberger, S. A.; Ashok, P. C.; Praveen, B. B.; Dholakia, K.; Tarascon, J.-M.; Bruce, P. G., The role of LiO₂ solubility in O₂ reduction in aprotic solvents and its consequences for Li–O₂ batteries. *Nat Chem* **2014**, 6, (12), 1091-1099.
- [24] Aetukuri, N. B.; McCloskey, B. D.; García, J. M.; Krupp, L. E.; Viswanathan, V.; Luntz, A. C., Solvating additives drive solution-mediated electrochemistry and enhance toroid growth in non-aqueous Li–O₂ batteries. *Nat Chem* **2015**, 7, (1), 50-56.
- [25] Abraham, K. M., Electrolyte-Directed Reactions of the Oxygen Electrode in Lithium-Air Batteries. *Journal of the Electrochemical Society* **2015**, 162, (2), A3021-A3031.
- [26] Heyd, J.; Scuseria, G. E.; Ernzerhof, M., Hybrid functionals based on a screened Coulomb potential. *The Journal of Chemical Physics* **2003**, 118, (18), 8207-8215.
- [27] Heyd, J.; Scuseria, G. E.; Ernzerhof, M., Erratum: “Hybrid functionals based on a screened Coulomb potential” [J. Chem. Phys. 118, 8207 (2003)]. *The Journal of Chemical Physics* **2006**, 124, (21), 219906.
- [28] Kresse, G.; Furthmüller, J., Efficient iterative schemes for \textit{ab initio} total-energy calculations using a plane-wave basis set. *Physical Review B* **1996**, 54, (16), 11169-11186.
- [29] Blöchl, P. E., Projector augmented-wave method. *Physical Review B* **1994**,

50, (24), 17953-17979.

[30] Komsa, H.-P.; Rantala, T. T.; Pasquarello, A., Finite-size supercell correction schemes for charged defect calculations. *Physical Review B* **2012**, 86, (4), 045112.

[31] Makov, G.; Payne, M. C., Periodic boundary conditions in *ab initio* calculations. *Physical Review B* **1995**, 51, (7), 4014-4022.

[32] Hummelshøj, J. S.; Blomqvist, J.; Datta, S.; Vegge, T.; Rossmeisl, J.; Thygesen, K. S.; Luntz, A. C.; Jacobsen, K. W.; Nørskov, J. K., Communications: Elementary oxygen electrode reactions in the aprotic Li-air battery. *The Journal of Chemical Physics* **2010**, 132, (7), 071101.

[33] Kang, S.; Mo, Y.; Ong, S. P.; Ceder, G., Nanoscale Stabilization of Sodium Oxides: Implications for Na-O₂ Batteries. *Nano Letters* **2014**, 14, (2), 1016-1020.

[34] Chase, M. W., *NIST-JANAF thermochemical tables*. American Chemical Society: American Institute of Physics for the National Institute of Standards and Technology: Washington, DC, 1998.

[35] H. Jonsson, G. M., K. W. Jacobsen, and B. J. Berne, *Classical and Quantum Dynamics in Condensed Phase Simulations*. World Scientific, Singapore: 1998.

[36] Radin, M. D.; Monroe, C. W.; Siegel, D. J., How Dopants Can Enhance Charge Transport in Li₂O₂. *Chemistry of Materials* **2015**, 27, (3), 839-847.

[37] Kang, J.; Jung, Y. S.; Wei, S.-H.; Dillon, A. C., Implications of the formation of small polarons in Li₂O₂ for Li-air batteries. *Physical Review B* **2012**, 85, (3), 035210.

- [38] Fishman, M.; Zhuang, H. L.; Mathew, K.; Dirschka, W.; Hennig, R. G., Accuracy of exchange-correlation functionals and effect of solvation on the surface energy of copper. *Physical Review B* **2013**, 87, (24), 245402.
- [39] Mathew, K.; Sundararaman, R.; Letchworth-Weaver, K.; Arias, T. A.; Hennig, R. G., Implicit solvation model for density-functional study of nanocrystal surfaces and reaction pathways. *The Journal of Chemical Physics* **2014**, 140, (8), 084106.
- [40] Ben-Naim, A., *Solvation Thermodynamics*. Plenum Press: New York, 1987.
- [41] Burgess, J., *Metal ions in Solution*. Chichester: Horwood Ellis: New York, 1978.
- [42] Lu, Y.-C.; Kwabi, D. G.; Yao, K. P. C.; Harding, J. R.; Zhou, J.; Zuin, L.; Shao-Horn, Y., The discharge rate capability of rechargeable Li-O₂ batteries. *Energy & Environmental Science* **2011**, 4, (8), 2999-3007.
- [43] Yang, J.; Zhai, D.; Wang, H.-H.; Lau, K. C.; Schlueter, J. A.; Du, P.; Myers, D. J.; Sun, Y.-K.; Curtiss, L. A.; Amine, K., Evidence for lithium superoxide-like species in the discharge product of a Li-O₂ battery. *Physical Chemistry Chemical Physics* **2013**, 15, (11), 3764-3771.
- [44] Kang, S.; Mo, Y.; Ong, S. P.; Ceder, G., A Facile Mechanism for Recharging Li₂O₂ in Li-O₂ Batteries. *Chemistry of Materials* **2013**, 25, (16), 3328-3336.
- [45] Ong, S. P.; Mo, Y.; Ceder, G., Low hole polaron migration barrier in lithium peroxide. *Physical Review B* **2012**, 85, (8), 081105.
- [46] Varley, J. B.; Viswanathan, V.; Norskov, J. K.; Luntz, A. C., Lithium and

oxygen vacancies and their role in Li₂O₂ charge transport in Li-O₂ batteries. *Energy & Environmental Science* **2014**, 7, (2), 720-727.

[47] Luntz, A. C.; Viswanathan, V.; Voss, J.; Varley, J. B.; Nørskov, J. K.; Scheffler, R.; Speidel, A., Tunneling and Polaron Charge Transport through Li₂O₂ in Li-O₂ Batteries. *The Journal of Physical Chemistry Letters* **2013**, 4, (20), 3494-3499.

[48] Viswanathan, V.; Nørskov, J. K.; Speidel, A.; Scheffler, R.; Gowda, S.; Luntz, A. C., Li-O₂ Kinetic Overpotentials: Tafel Plots from Experiment and First-Principles Theory. *The Journal of Physical Chemistry Letters* **2013**, 4, (4), 556-560.

[49] Tilley, R. J. D., *Defects in Solids*. John Wiley & Sons, Inc.: 2008.

[50] Van de Walle, C. G.; Neugebauer, J., First-principles calculations for defects and impurities: Applications to III-nitrides. *Journal of Applied Physics* **2004**, 95, (8), 3851-3879.

[51] Viswanathan, V.; Thygesen, K. S.; Hummelshøj, J. S.; Nørskov, J. K.; Girishkumar, G.; McCloskey, B. D.; Luntz, A. C., Electrical conductivity in Li₂O₂ and its role in determining capacity limitations in non-aqueous Li-O₂ batteries. *The Journal of Chemical Physics* **2011**, 135, (21), 214704.

[52] Kim, J.; Lim, H.-D.; Gwon, H.; Kang, K., Sodium-oxygen batteries with alkyl-carbonate and ether based electrolytes. *Physical Chemistry Chemical Physics* **2013**, 15, (10), 3623-3629.

[53] Petrowsky, M. A., *Ion transport in liquid electrolytes*. Department of Chemistry and Biochemistry, University of Oklahoma, Norman, OK: 2008.

[54] Khetan, A.; Luntz, A.; Viswanathan, V., Trade-Offs in Capacity and

Rechargeability in Nonaqueous Li–O₂ Batteries: Solution-Driven Growth versus Nucleophilic Stability. *The Journal of Physical Chemistry Letters* **2015**, 6, (7), 1254-1259.

[55] Marcus, R. A., On the Theory of Oxidation-Reduction Reactions Involving Electron Transfer. I. *The Journal of Chemical Physics* **1956**, 24, (5), 966-978.

[56] Newton, M. D., *Electron Transfer in Chemistry, Volume 1: Principles, Theories, Methods, and Techniques*. Wiley-VCH: Weinheim, Federal Republic of Germany, **2001**.

[57] Adelstein, N.; Neaton, J. B.; Asta, M.; De Jonghe, L. C., Density functional theory based calculation of small-polaron mobility in hematite. *Physical Review B* **2014**, 89, (24), 245115.

Chapter 3. Rational design of redox mediators for advanced Li-O₂ batteries

(The content of this chapter has been published in *Nature Energy*. Reproduced with permission from [Lim, H.-D. and Lee, B. et al., *Nature Energy* **2016**, 1, 16066.]

Copyright (2016) Nature Publishing Group)

3.1 Introduction

The rapid growth of portable energy demands has increased interest in next-generation batteries with high energy densities. Among several post-lithium ion battery candidates, Li-O₂ batteries have attracted tremendous attention because of their exceptionally high theoretical energy density (~3,500 Wh kg⁻¹). [1-4] The absence of a transition metal and the use of abundant resources of oxygen in the electrochemical reaction further make this chemistry appealing as a promising future battery system. [5-7] However, the current state of Li-O₂ batteries involves the critical limitations of low cycle life and high charging overpotential (low energy efficiency) during cycling. [8-10] Although the cycle life and high overpotential are believed to be correlated to each other to some extent, the origin of the latter is often attributed to several factors in the decomposition process of Li₂O₂, such as the sluggish oxygen evolution from the Li₂O₂ crystal, low electrical conductivity, and formation/decomposition of unwanted products including Li₂CO₃. [11-14]

Furthermore, the solid discharge product (Li_2O_2) in Li-O_2 batteries is irregularly formed on the electrode; thus, the porous air cathode is easily clogged, hindering the efficient transport of oxygen and ions causing further overpotential. [15, 16] Addressing these issues and enhancing the energy efficiency by decreasing the overpotential are indispensable in taking advantage of the high energy density of the Li-O_2 battery chemistry.

In this respect, the discovery of effective catalysts that are capable of effectively decomposing Li_2O_2 lies at the heart of the development of advanced Li-O_2 systems. During the early stage of research on developing catalysts for rechargeable Li-O_2 batteries, commonly used catalysts in the oxygen evolution reaction in fuel cells or water-splitting devices, were widely adopted, which resulted in some improvements. [17-20] However, it was observed that some of the catalysts severely promote the decomposition of the electrolyte solvents as well. [21] Moreover, the limited active sites at the solid–solid contact between a catalyst and the discharge product led to generally low catalytic activities. To circumvent this issue, more recently, the use of a soluble catalyst or redox mediator (RM) was proposed. [22-24] The diffusible RMs can easily move around in the electrolyte and have wet-contact with solid discharge products, thus maximizing the interaction areas for the catalysis. This approach was also beneficial in charging the discharge products that are detached or isolated from the electrode, which led to a dramatic increase in the cycle life and efficiency of Li-O_2 batteries. [22, 25] Accordingly, researchers have reported several types of soluble

catalysts such as tetrathiafulvalene (TTF), [22] LiI, [1, 23, 26] tetramethylpiperidinyloxy (TEMPO), [27] and iron phthalocyanine (FePc), [28] all of which have exhibited significantly reduced overpotential.

An appropriate selection of the catalyst can be used to manipulate the overpotential value because the redox potential of the RM determines the charging voltage of the electrochemical cell. Strategic design principles concerning the RM, hence, would be beneficial in systematically minimizing the overpotential and improving the cycle stability. In this work, a general design principle for finding a catalyst based on the ionization energy (I.E.) is proposed. We find that organic materials with only a certain range of I.E. can be utilized as a soluble catalyst. The combined density functional theory (DFT) calculations and experiments also reveal that catalysts with suitable highest occupied molecular orbital (HOMO) energy levels of the pristine and oxidized forms must be selected considering the Li_2O_2 decomposition energy and oxidation potential of the electrolyte solvent, which would determine the theoretical overpotential and stability. Based on the proposed strategy, we discovered 5,10-dimethylphenazine (DMPZ) which exhibits a remarkably low overpotential and stability. The identification of the key design descriptor herein will spur the development of effective soluble catalysts and provide a step forward in enhancing the performance of Li- O_2 batteries.

3.2 Method

3.2.1 Calculations details

Geometry optimization and energy evaluation of the molecules were conducted using a DFT calculation tool, Gaussian 09 quantum chemistry package. [29] For all the calculations, spin-unrestricted DFT was performed based on the Becke–Lee–Yang–Parr (B3LYP) hybrid exchange-correlation functional[30-32] and triple-zeta valence polarization (TZVP) basis set. [33-35] In the HOMO/LUMO plot, the Li/Li^+ redox potential was set to -1.39 V versus AVS because standard hydrogen electrode (SHE) is -4.44 V *vs.* AVS and Li/Li^+ is -3.05 V *vs.* SHE. [36, 37] Therefore, the redox potential of lithium peroxide formation $1/2 \cdot \text{Li}_2\text{O}_2 \leftrightarrow \text{Li}^+ + \text{e}^- + 1/2 \cdot \text{O}_2$ can be set to -4.35 V *vs.* AVS (-2.96 V *vs.* SHE), the electron energy of which corresponds to -4.35 eV *vs.* AVS. We note that Li/Li^+ redox potential of -3.05 V *vs.* SHE, which was derived in aqueous environment, can shift with the selection of solvent. The Li/Li^+ potential change in TEGDME was predicted to be less than 0.2 V compared to the aqueous solution [38, 39] (Table 3-1 and Figure 3-24), hence here we neglected the influence of solvent on the redox potential of Li/Li^+ *vs.* SHE. The catalytic activities of the target molecules were evaluated based on their HOMO/LUMO level with respect to the i) electron energy of the Li_2O_2 formation reaction and ii) HOMO/LUMO value of the electrolyte molecule. The redox potentials of the molecules were defined as the energy difference between the reduced and neutral molecule per electron, i.e., I.E. per electron *vs.* AVS and downshifted by 1.39 V if

Li/Li⁺ was used as the reference. A slight deviation of the calculated redox potential from the experimental value can occur due to intrinsic DFT errors, [40] however they were within ~0.3 V as shown in Table 3-2.

Solvent	Donor number ^[38] (kcal/mol)	Li/Li ⁺ redox potential vs.
		SHE ^[39] (V)
Benzonitrile	11.9	-2.68
Acetonitrile	14.1	-2.74
Tetramethylenesulfone	14.8	-2.8
Propylene carbonate	15.1	-2.78
Acetone	17	-2.94
Methanol	19	-3.09
Trimethyl phosphate	23	-3.26
N,N-dimethylformamide	26.6	-3.16
N-methylformamide	27	-3.2
1-methyl-2-pyrrolidinone	27.3	-3.24
N,N-dimethylacetamide	27.8	-3.23
Dimethylsulfoxide	29.8	-3.4
N,N-diethylformamide	30.9	-3.16
N,N,N,N-tetramethylurea	31	-3.3
N,N-diethylacetamide	32.2	-3.31

Table 3-1. Donor number of various non-aqueous solvents and Li/Li⁺ redox potential vs. SHE in each solvent.

Molecules	Redox potential from I.E. calculation (a) (vs. Li/Li ⁺)	Redox potential from HOMO level calculation (b) (vs. Li/Li ⁺)	Redox potential from experiment (c) (vs. Li/Li ⁺)	ΔE (c)-(a)	ΔE (c)-(b)	ΔE (a)-(b)
PPD	3.89	3.87	4.0	0.11	0.13	0.02
TMA	3.82	3.90	3.9	0.08	0	-0.08
NDA	3.65	3.86	3.6	-0.05	-0.26	-0.21
DMPZ	3.11	3.15	3.3	0.19	0.15	-0.04
TTF	3.43	3.47	3.6	0.17	0.13	-0.04
TMPD	3.09	3.35	3.3	0.21	-0.05	-0.26

Table 3-2. Experimental and calculated redox potential of RM candidates. See Supplementary Note 1 for detailed discussion.

3.2.2 Preparation of Li-O₂ cells

The air electrode was fabricated using a mixture of Ketjen black carbon (EC 600JD, Ilshin Chemtech) and polytetrafluoroethylene (PTFE, 60 wt % dispersion in H₂O) at a ratio of 8:2. The mixture was dispersed in isopropanol solution and cast on a Ni mesh (Nillaco Corp., 12.7 mm in diameter) current collector. The mixture was dried overnight at 60 °C to eliminate residual solvents. The Li-O₂ cell was assembled into a Swagelok-type cell as a sequence of lithium metal (1/2 in. diameter), a glass fiber separator (Whatman GF/D microfiber filter paper, 2.7-μm pore size), and the prepared air electrode; 1 M lithium bis (trifluoromethane) sulfonamide (LiTFSI) in TEGDME was used as a reference electrolyte. The water contents in the electrolytes are 22 ppm (TEGDME) and 27 ppm (DMSO) by a Karl Fisher titration. After the cell assembly, the cells were stabilized in an oxygen atmosphere for 0.5 h before testing.

3.2.3 Characterizations

All the electrochemical properties were evaluated using a potentio-galvanostat (WonA Tech, WBCS 3000, Korea) at a constant current of 0.2 mA cm^{-2} between 2.0–4.5 V. The internal atmosphere of each cell was carefully controlled and maintained with a high purity of oxygen (770 Torr) using an automated throttle valve. For CV testing, 1 M LiTFSI in TEGDME was used as an electrolyte, and 0.01 M of each RM was added. The systems were composed of a gold working electrode and Pt counter electrode with Ag/Ag⁺ in acetonitrile solution as a reference electrode. The scan rate was constantly maintained at 100 mV s^{-1} . Fourier-transform infrared (FTIR) spectroscopy (FT-IR-4200, JASCO, Japan) and XRD (D8-Advance, Bruker, Germany) with Cu K α radiation were used in an argon atmosphere. FESEM (Philips, XL 30 FEG, Eindhoven, Netherlands) was used to examine the cell morphologies. For *in situ* gas analysis, a mass spectrometer (MS) (HPR-20, Hiden Analytical) combined with a potentio-galvanostat was used. Argon carrier gas was used at a constant flow rate of 10 cc min^{-1} , and the evolved gas from the cathode flew into the MS during the charge process. For gas analysis of chemical decomposition of Li₂O₂, each RM was electrochemically oxidized (i.e., charged) with an equivalent capacity of 0.03 mAh in TEGDME to produce the reactive RM⁺ in the electrolyte before being transferred to a sealed glass bottle containing the excess amount of Li₂O₂ powder (0.05 mg). The charge capacity of 0.03 mAh should be capable of decomposing 0.025 mg Li₂O₂ based on its theoretical capacity. The catalytic activity of the RMs was

visibly probed by gauging the amount of the evolved oxygen using the gas analyzer.

3.3 Results and discussion

3.3.1 Screening for RMs based on ionization energy

Figure 3-1a illustrates the reaction mechanism of the RM in Li-O₂ cells, which is considered as a two-step process involving electrochemical and chemical reactions. The RM is oxidized during a charging process near an electrode surface before or simultaneously with the charging of Li₂O₂, even though the redox potential of the RM is typically higher than that of the Li₂O₂ because of the high charging overpotential of Li₂O₂ decomposition (step 1, electrochemical reaction). The oxidized RM (RM⁺) freely diffuses in the electrolyte and chemically reacts with Li₂O₂, decomposing it into 2Li⁺ and O₂ gas, and reduces back to the initial state of the RM (step 2). Because the charging voltage of the cell is determined by step 1, i.e. electrochemical oxidation of the RMs, a charge polarization can be reduced by choosing an appropriate RM (Figure 3-1b). To induce the chemical oxidation/decomposition of Li₂O₂ by RM⁺, a higher redox potential of RM/RM⁺ than that of the Li₂O₂ formation is required. Thus, the selection of RMs with a suitable redox potential is critical.

Given the reaction mechanism, the redox potential of the RMs should be the first criteria in selecting RM candidates. RMs must be oxidized at a voltage higher than ~2.96 V (the theoretical formation voltage of Li₂O₂) to be capable of chemically decomposing Li₂O₂; however, it is preferred that this voltage be only slightly higher than 2.96 V to maximize the energy efficiency. Thus, selecting RM candidates

according to their redox potential would be a rational approach to finding RMs, and redox-active soluble organics with redox potentials that lie between ~ 3 and 4 V in the electrolyte can be considered possible RM candidates. However, the redox potentials of organic materials are not readily available in the literature and vary with the type of solvent used in the electrochemical cell. [1, 41] In our selection process, instead, we chose the I.E. values of molecules in a vacuum as a reference for the redox potential. It is believed that the I.E. can serve as an appropriate basis for the oxidation potential of RMs in an electrolyte as it represents the redox potential in a vacuum versus the absolute vacuum scale (AVS). Furthermore, I.E. values are well tabulated in a database for a large number of molecules [42] and can be simply measured using photoelectron spectroscopy [43]. Indeed, our DFT calculations of the I.E. values along with the values acquired from the literature for many organics [42] revealed that there is a roughly linear relationship between the I.E. and oxidation voltage (vs. Li/Li^+) in an electrolyte (Figure 3-2).

Notably, it was observed that most effective RMs reported to date have similar I.E. values of approximately 6.7 eV (TTF: 6.8 eV [44], ferrocene: 6.7 eV [45], N,N,N',N'-tetramethyl-p-phenylenediamine (TMPD): 6.7 eV [46]), hinting at the appropriate range of I.E. for possible RM organics. In Table 3-3, some candidates with I.E. values close to the value of ~ 6.7 eV are listed (from experimental reports or our DFT calculations) among randomly selected organic molecules. [47-50] As a reference, organics with I.E. values far from 6.7 eV (1,4-dioxane and N,N-dimethylformamide)

and the inorganic LiI that has been recently reported as an RM are also listed. We selected 1,5-naphthalenediamine (NDA), 4,N,N-trimethylaniline (TMA), 1-phenylpyrrolidine (PPD), naphthacene (NC), and DMPZ as candidates for RMs because their I.E. values are in the range of 5.8–6.8 eV based on the DFT calculations and experimental reports. [47-50] By considering the redox potential *vs.* Li/Li⁺, these I.E. values can be approximated as 3.4–4.4 V (*vs.* Li/Li⁺) in the electrochemical cell using tetraethylene glycol dimethylether (TEGDME) (see the experimental section for a detailed description of the calculations). Among the candidates, DMPZ exhibits the lowest redox voltage of 3.10 V compared with 3.64, 3.81, 3.83, and 3.89 for NDA, TMA, NC, and PPD, respectively, implying that all the candidates are capable of thermodynamically decomposing Li₂O₂ in oxidized form. Additionally, we examined two other candidates which have much higher I.E. values of approximately 9 eV (1,4-dioxane[51] and N,N-dimethylformamide[52]). These materials are supposed to be oxidized at 6.87 and 7.08 V (*vs.* Li/Li⁺) in TEGDME, respectively, and would not be oxidized under a typical voltage window (2.0–4.5 V) for a Li-O₂ battery, which will be experimentally demonstrated later.

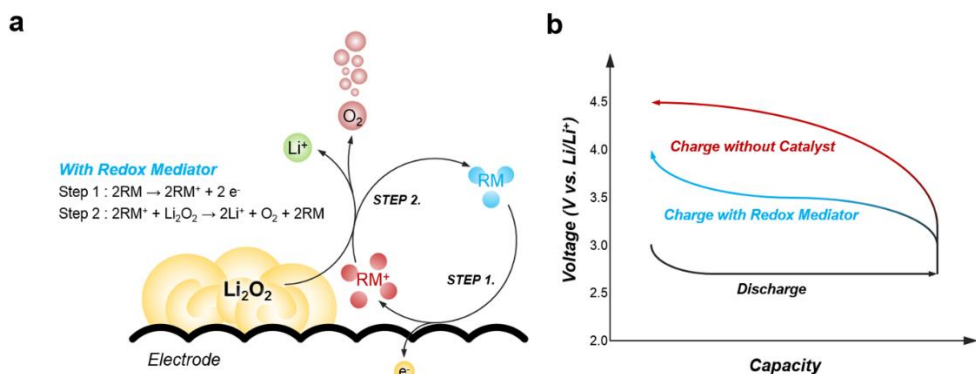


Figure 3-1. Role of RM for Li-O₂ batteries. (a) Schematic illustration of reaction mechanism of RM for Li-O₂ batteries. During the charge, RM (blue circles) is oxidized near the electrode surface (step 1, electrochemical reaction), then RM⁺ (red circles) chemically oxidizes Li₂O₂ to 2Li⁺ (green circle) and O₂ gas (orange circles). Finally, RM⁺ is reduced to the initial state of RM (step 2, chemical reaction). (b) Schematic discharge (black line) and charge profiles of Li-O₂ batteries with (blue line) and without RM (red line).

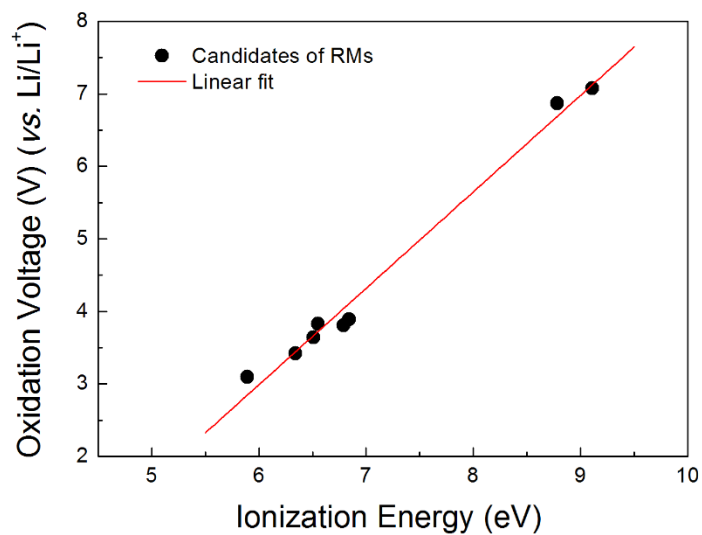


Figure 3-2. Relationship between ionization energy in a vacuum and oxidation voltage (vs. Li/Li⁺) in TEGDME electrolyte for the RM candidates described in Table 3-3.

No.	Name	Chemical formula	I. E. in vacuum (Exp.)	I. E. in vacuum (Cal.)	Oxidation V. in TEGDME (vs. Li/Li ⁺) (Exp.)	Oxidation V. in TEGDME (vs. Li/Li ⁺) (Cal.)
1	Tetrathiafulvalene (TTF)	C ₈ H ₄ S ₄	6.83 eV ⁴⁴⁾	6.34 eV	3.6 V ²²⁾	-
2	Ferrocene (FC)	C ₁₀ H ₁₀ Fe	6.72 eV ⁴⁵⁾	7.1 eV	3.6 V ²²⁾	-
3	N,N,N',N'-tetramethyl-p-phenylenediamine (TMPD)	C ₁₀ H ₁₆ N ₂	6.75 eV ⁴⁶⁾	5.88 eV	3.3 V ²²⁾	-
4	Lithium iodide *	LiI	-	-	2.95 - 3.55 V ^{1), 26)}	-
5	1,5-Naphthalenediamine (NDA)	C ₁₀ H ₁₀ N ₂	6.45 eV ⁴⁷⁾	6.51 eV	-	3.64 V
6	4,N,N-Trimethylaniline (TMA)	C ₉ H ₁₃ N	6.9 eV ⁴⁸⁾	6.79 eV	-	3.81 V
7	1-Phenylpyrrolidine (PPD)	C ₁₀ H ₁₃ N	6.8 eV ⁴⁹⁾	6.84 eV	-	3.89 V
8	Naphthacene (NC)	C ₁₈ H ₁₂	6.64 eV ⁵⁰⁾	6.55 eV	-	3.83 V
9	5,10-Dimethylphenazine (DMPZ)	C ₁₄ H ₁₄ N ₂	-	5.89 eV	-	3.10 V
10	1,4-Dioxane	C ₄ H ₈ O ₂	9.19 eV ⁵¹⁾	8.78 eV	-	6.87 V
11	N,N-Dimethylformamide	C ₃ H ₇ NO	9.12 eV ⁵²⁾	9.11 eV	-	7.08 V

* Various redox potentials of I⁻/I₃⁻ couple were reported in different solvent/electrode environment.

Table 3-3. Various RM candidates for Li-O₂ batteries.

3.3.2 Verification of the catalytic effect of RMs

Using the prescreened RM candidates, the chemical stability was first examined in a typical Li-O₂ cell because a soluble catalyst should be dissolved in an electrolyte and stable for a long time even in an oxygen atmosphere. All the candidates were observed to be well dissolved in the TEGDME-based electrolyte and stable in the absence of oxygen flowing (Figure 3-3). The stability in the oxygen flowing atmosphere was also investigated by monitoring the open-circuit voltage (OCV) in Li-O₂ cells (Figure 3-4a). Although a noticeable change was not observed for DMPZ, NDA, TMA, and PPD, the OCV of NC continuously decreased during a relaxation, indicating the instability in the electrochemical cell. This instability is attributed to the general tendency of acene-based materials, which are easily degraded in the presence of air and light. [53, 54]

The oxidation voltages of prescreened RMs were experimentally measured in the electrochemical cells, where each of the RMs was dissolved in TEGDME and electrochemically oxidized in Ar atmosphere, as illustrated in Figure 3-4b. The average charge voltages (vs. Li/Li⁺) of DMPZ, NDA, TMA, and PPD are 3.29, 3.64, 3.88, and 3.93 V, respectively, which are in agreement with our calculation results presented in Table 3-3. DMPZ exhibits the lowest oxidation voltage among the candidates as predicted, implying that DMPZ, if the redox reaction is reversible, could be an efficient catalyst for Li-O₂ batteries. Additionally, two organics (1,4-dioxane and N,N-dimethylformamide) with I.E. values much higher than 6.7 eV were

examined in an identical electrochemical cell; however, no activity is observed in the conventional operating voltage range (below 5 V) in Figure 3-4b due to their high expected oxidation voltages of 6.87 and 7.08 V (*vs.* Li/Li⁺), respectively, as indicated in Table 3-3. The series of experimental measurements of redox voltages of the prescreened RMs agree remarkably well with our prediction using I.E..

The electrochemical activities of the RMs were further evaluated in practical Li-O₂ cells. Figure 3-4c presents the first discharge/charge profiles of Li-O₂ cells employing different RMs compared with that of the reference Li-O₂ cell without a RM. All the cells were discharged and recharged to the same capacity of 1 mAh at a constant rate of 0.2 mA cm⁻² to ensure the same amount of formation/decomposition of Li₂O₂. It is clearly observable that the NDA, TMA, PPD, and DMPZ can significantly decrease the charge polarization in Li-O₂ cells compared with the cells without the RM. Moreover, it is noteworthy that the overall charging polarization reduces in the order of DMPZ, NDA, TMA, and PPD, which also agrees with the prediction in Table 3-3 and the experimental results in Figure 3-4b. The slight increase of the charging voltage at the end compared with the cell without discharge in Figure 3-4b is attributed to the transport limitations in the porous carbon-based air electrode, as demonstrated in previous reports [23] and in Figure 3-5. The control group of the two RMs (1,4-dioxane and N,N-dimethylformamide), which have high I.E. values of approximately 9 eV, did not affect the charge profiles and exhibited similar charge overpotentials to that of the reference cell without the RM. This result occurred

because the controls could not be oxidized below 5 V, as shown in Figure 3-4b, and thus did not function as RMs. In addition, in agreement with the OCV stability test, NC was unstable and rapidly degraded with the start of the discharge.

To verify whether the charging of the cell accompanies the decomposition of Li_2O_2 by the RM, we tested the chemical reactivity of the oxidized RM (RM^+) with Li_2O_2 using gas analysis, as schematically illustrated in Figure 3-6a. Pre-charged each RM was transferred to excess amount of Li_2O_2 powder, then corresponding oxygen gas evolved was gauged using the gas analyzer (Figures 3-6b-f). See method section for detailed procedure. The amount of evolved oxygen could be quantified by comparing with the number of electrons transferred (e^-/O_2), which verifies the selectivity of RMs to the decomposition of Li_2O_2 . Figure 3-6b demonstrates that the efficiencies of TTF and LiI (2.08 and 2.22, respectively) correspond to the theoretical value of 2, which confirms their high efficiencies for decomposing Li_2O_2 as previously reported. [22, 23] However, NDA, TMA, and PPD evolved only a small fraction of oxygen compared with the expected value and exhibited e^-/O_2 ratios of 3.00, 4.51, and 5.50, respectively. This result indicates that a significant portion of side reactions other than Li_2O_2 decomposition occurred in chemical contact with these RM^+ species. However, it is noteworthy that DMPZ produces the expected amount of oxygen, exhibiting the highest efficiency ($e^-/\text{O}_2 = 2.08$) among the candidates, pointing to the discovery of DMPZ as an effective catalyst in Li- O_2 batteries. [22, 23]

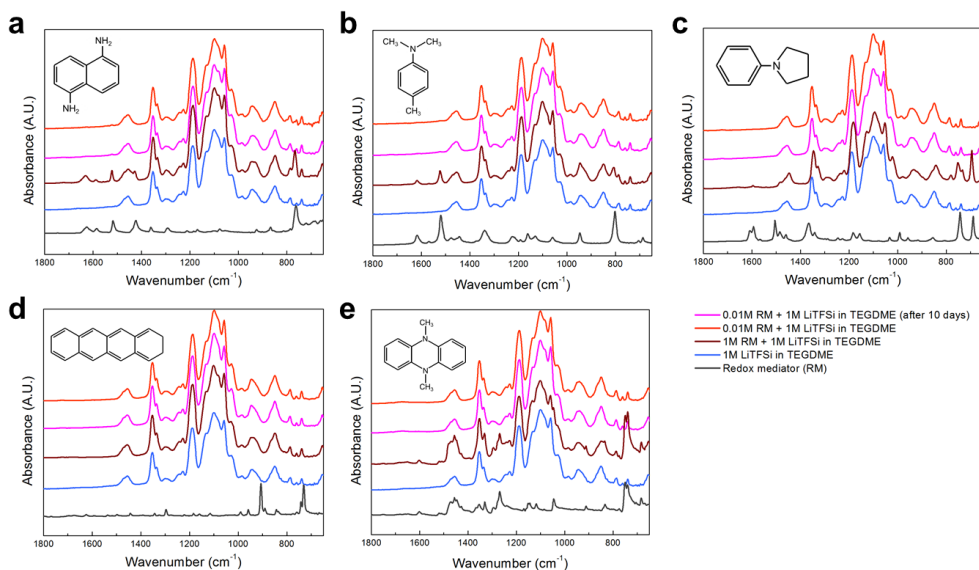


Figure 3-3. FT-IR spectra of (a) NDA, (b) TMA, (c) PPD, (d) NC, and (e) DMPZ in the range of 1800–650 cm^{-1} . The spectra were obtained after dissolving the RMs in TEGDME. All the RMs were well dissolved in TEGDME and stable even after 10 days. Although NC was not identified after its dissolution in the electrolyte, the electrolyte exhibited no changes and appeared to be stable.

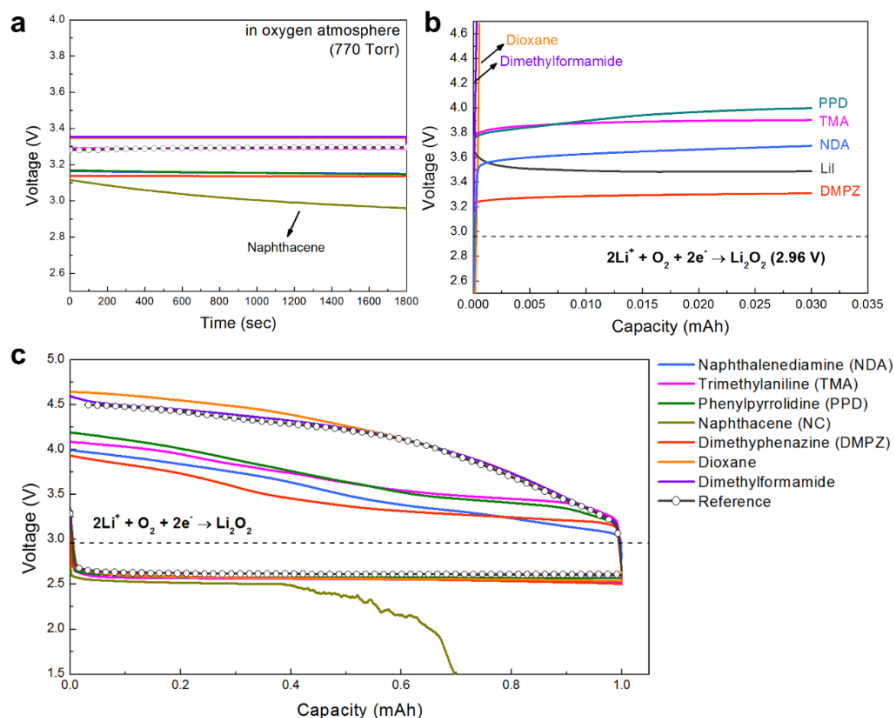


Figure 3-4. Electrochemical properties of various RMs. (a) Change of OCVs of Li-O₂ cells with various RMs upon a time. The line with small circles indicates the reference cell without catalyst. (b) Electrochemical oxidation potentials of RMs dissolved in the electrolyte under an Ar atmosphere. The dotted line is the theoretical formation voltage of Li₂O₂. (c) The first discharge and charge profiles of Li-O₂ cells using various 0.01 M RMs at a constant current density of 0.2 mA cm⁻². Discharge capacity are limited to 1 mAh and recharged to the same capacity. The reference (the line with small circles) indicates the electrochemical profile of Li-O₂ cell without catalyst.

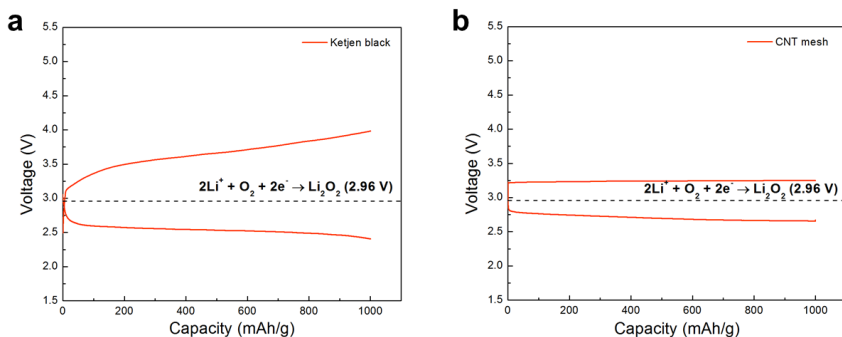


Figure 3-5. The first discharge and charge profiles of Li-O₂ cells using a) Ketjen black electrode with LiI catalyst and b) carbon nanotube mesh electrode with LiI catalyst. The discharge capacity is limited to 1000 mAhg⁻¹, and the current density is 200 mA g⁻¹. Even if the Li-O₂ cells used the same soluble catalyst of LiI, the charge profiles were different based on the types of air cathodes used. A slight deviation of the charge profile is observed in the cell using the bulk carbon of Ketjen black because of the transport limitations of the catalyst and reaction products, whereas constant charge potential was observed using the hierarchically porous carbon nanotube mesh electrode.

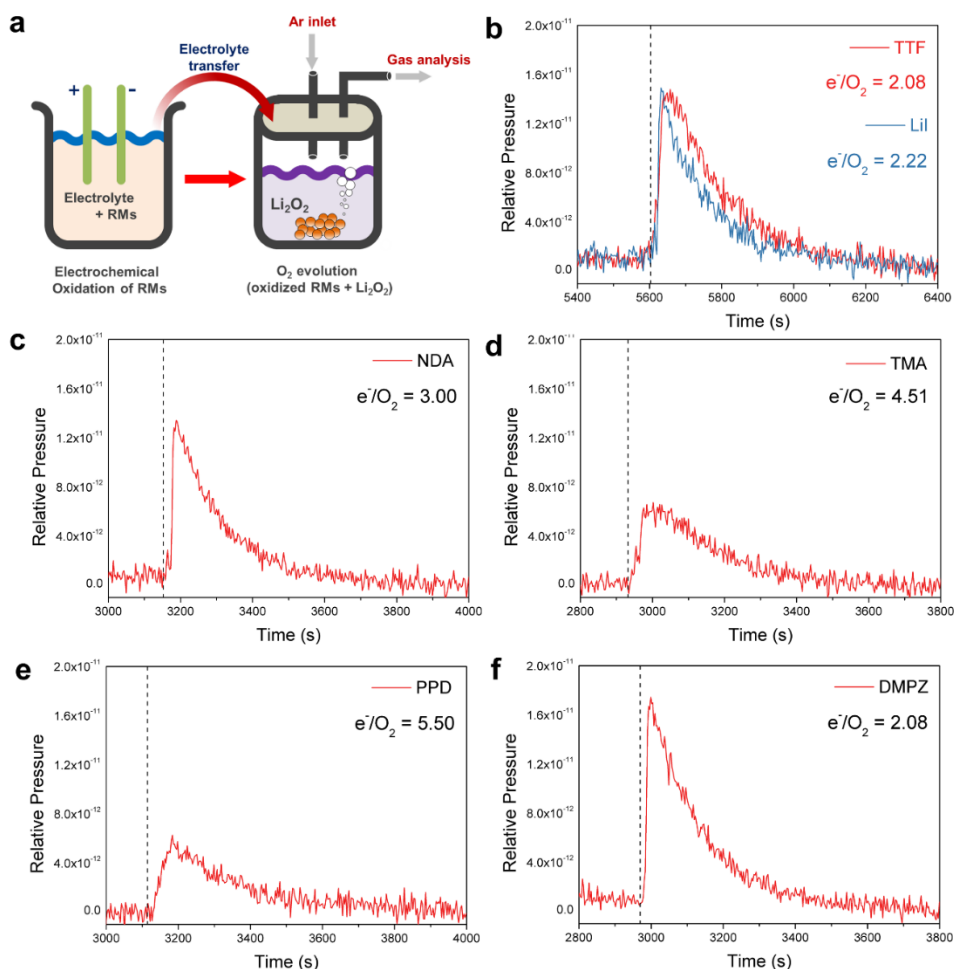


Figure 3-6. Gas analyses on effect of RMs. (a) Schematic illustration of the gas analysis process. RMs dissolved in the electrolyte were electrochemically charged to 0.03 mAh, and the electrolyte containing the RMs⁺ was transferred to the excess Li₂O₂ powder in a glass vial. Then, the evolved inner gases were flowed into the gas analyzer. Detections of the evolved oxygen using (b) TTF and LiI, (c) NDA, (d) TMA, (e) PPD, and (f) DMPZ. The Ar carrier gas was flowed in at a constant rate of 10 ml min⁻¹, and the dotted line represents the injection time of the electrolyte in the vial.

3.3.3 Understanding the reaction mechanism of RMs

The origin of different charging polarizations and efficiencies among candidate RMs can be understood with respect to the relative energetic states of RM, RM^+ , and the electrolyte solvent. We calculated the energy levels of the pristine and oxidized states of the RMs and compared them with the energy of the electrolyte oxidation, as shown in Figure 3-7. The energy levels of the RMs were calculated in an electrolyte environment by adopting dielectric constants (ϵ) of TEGDME (7.9) and DMSO (46.8) as described in Figure 3-7 and Figure 3-8, respectively. The black bars in the figure indicate the energy levels of the pristine RMs, where the two energy levels for each RM represent the lowest unoccupied molecular orbital (LUMO) and HOMO levels. Considering that the magnitude of the HOMO energy is generally identical to the I.E. (Koopmans' theorem) and corresponds to the redox potential (vs. AVS) of RM/RM^+ , all the prescreened molecules were observed to be capable of decomposing Li_2O_2 . Their redox potentials are highlighted in yellow and are higher than the 2.96 V value for Li_2O_2 decomposition (blue dotted line vs. Li/Li^+) in Figure 3-7, which is also consistent with the experiments above. However, to achieve a low charging polarization in $\text{Li}-\text{O}_2$ cells, the RM/RM^+ redox potentials are recommended to be located near the electron energy of Li_2O_2 formation. For example, the redox level of $\text{DMPZ}/\text{DMPZ}^+$ is located near the dotted blue line; thus, this molecule is capable of exhibiting the lowest charge voltage and highest energy efficiency among the candidates, as demonstrated in Figure 3-4b and 3-4c. The redox potential of the

control group (1,4-dioxane and N,N-dimethylformamide) resides below 2.96 V; however, is too far from the energy level, making the control group practically less useful as RMs even when oxidized (Figure 3-9).

Some RMs^+ may not only decompose Li_2O_2 but also oxidize the electrolyte solvent, causing unwanted side reactions in the Li-O_2 cell. This process will gradually consume the electrolyte, yielding byproducts and degrading the cycle life of the cell. The relative position of the singly occupied molecular orbital (SOMO) energies of the RMs^+ with respect to HOMO of the electrolyte can serve as a useful criterion for predicting the efficiency and selectivity of RMs. The red bars in Figure 3-7 indicate the re-configured SOMO and LUMO levels of the RMs when they are oxidized during a charge process. The SOMO energies of the RMs^+ should be higher than HOMO of the electrolyte; otherwise, the RM^+ can be reduced to RM by taking the electron from the electrolyte instead of decomposing Li_2O_2 . In this case, the decomposition of both Li_2O_2 and the electrolyte would occur simultaneously, and the oxidized electrolyte can further react with oxygen radicals or Li_2O_2 by nucleophilic attack, degrading the cell performance by forming various byproducts. [37, 38, 55-58] (See Figure 3-10 for detailed discussion.)

The prescreened RMs can be roughly divided into two groups, as indicated by the purple and green boxes. The RMs in the purple box of Figure 3-7, including FC^+ , TMA^+ and PPD^+ , exhibit SOMO levels lower than HOMO of TEGDME, whereas the SOMO levels of DMPZ^+ and TTF^+ in the green box are higher than HOMO of the

electrolyte. It implies that the RMs in the purple box would undergo significant side reactions with the electrolyte during cycling in contrast to those in the green box. This speculation is in good agreement with previous observations on FC reported by Chen *et al.*[22] and our experimental results in Figure 3-6, which indicate that TMA and PPD exhibit substantially lower efficiencies in the gas evolution experiments. In addition, it is remarkably consistent with the results on DMPZ and TTF, which were capable of selectively decomposing Li_2O_2 , resulting in a nearly theoretical amount of oxygen evolution (i.e., $e^-/\text{O}_2 = 2.08$ for DMPZ and TTF).

For NDA^+ whose SOMO energy is higher than HOMO of the electrolyte, the efficiency in decomposing Li_2O_2 (Figure 3-6) does not reach the level of DMPZ and TTF (i.e., $e^-/\text{O}_2 = 3.00$ for NDA) even though it is higher than that of TMA and PPD. We believe that this result is due to the slight uncertainty in the estimation of the energy level of TEGDME. It is known that the HOMO/LUMO energy of the solvent (TEGDME) can be affected by the solvation characteristics of different salts and that the HOMO/LUMO gap can shrink near the substrate (i.e., electrode materials in our study)[37, 59-61] to some extent. These considerations indicate that the HOMO level of TEGDME would lie in a certain range around the calculated value for pure TEGDME, as indicated for the gray-shaded area in Figure 3-7. In this gray-shaded region, a reaction between the RMs^+ and electrolyte possibly occurs, reducing the efficiency and selectivity of the RMs as for NDA.

We further investigated HOMO/LUMO level of various reported RMs in literature,

such as 2,2,6,6-tetramethylpiperidinyloxy (TEMPO)[27], tris[4-(diethylamino)phenyl]amine (TDPA)[62] and iron phthalocyanine (FePc)[28], of which results agreed well with corresponding experiments (Figure 3-11). See more discussion on the stability of electrolyte with RMs in Figure 3-12. Consequently, RMs^+ with SOMO levels further from HOMO of the electrolyte can be better utilized as efficient catalysts. The gap between the LUMO and HOMO of NC is obviously small (approximately 2.9 eV) compared with that of the other candidates. Because of the small band gap below 3 eV, photo-oxidation is prone to be triggered, [63] leading to the unstable OCV and discharge property demonstrated in Figure 3-4.

To further verify the reversibility and efficiency of the RMs, a cyclic voltammetry (CV) tests were performed using a three-electrode cell, as shown in Figure 3-13 and Figure 3-14. When there is a minimal side reaction between the RMs and electrolyte, reversible redox peaks of RM/RM^+ are expected during both the anodic and cathodic scan. In the case of NDA, the first oxidation peak is observed at 3.75 V in Figure 3-13a, however, its corresponding reduction peak is not unambiguously identified; instead, a small reduction peak appears at approximately 3.1 V. In addition, a new reduction peak is observed at 2.4 V, which is attributed to peak from the reduction of a proton possibly originating from the electrolyte deterioration. [64] This result indicates that the redox of NDA/NDA^+ is not fully stable in the TEGDME and accompanies some side reactions with the electrolyte. Similar results are observed for TMA and PPD in Figures 3-13b and c. The first oxidations are observed between 3.5

and 4 V; however, a corresponding peak during the reduction does not appear as clearly as during the oxidation.

These CV results are well matched with differential electrochemical mass spectrometry experiment and our calculation, revealing the low efficiencies of NDA, TMA, and PPD. In contrast, the reversible redox of DMPZ/DMPZ⁺ is clearly displayed in Figure 3-13d. The first oxidation occurs at ~3.4V, which is followed by the symmetrically equivalent reduction peak at ~3.3V with negligibly small polarization. Moreover, the second oxidation/reduction of DMPZ⁺/DMPZ²⁺ at higher potential (~4V vs. Li/Li⁺) was also highly reversible without any signature of a side reaction peak after hundreds of cycles of CV (Figure 3-13e). It implies that even in the overcharged states of RM, the DMPZ would maintain its chemical stability by the additional redox capability. (See Figure 3-15 for the discussion on the stability of DMPZ²⁺ in the electrolyte.) We additionally tested the reversible activity of DMPZ in a dimethyl sulfoxide (DMSO)-based electrolyte or in the oxygen atmosphere in Figure 3-13f. Both results indicated that the redox of DMPZ/DMPZ⁺ is highly reversible under various electrolyte conditions and stably accompanies the redox reaction of O₂/O₂⁻ in the electrolyte. See the stability of DMPZ/DMPZ⁺ redox under the prolonged cycles in Figure 3-16 and Figure 3-17.

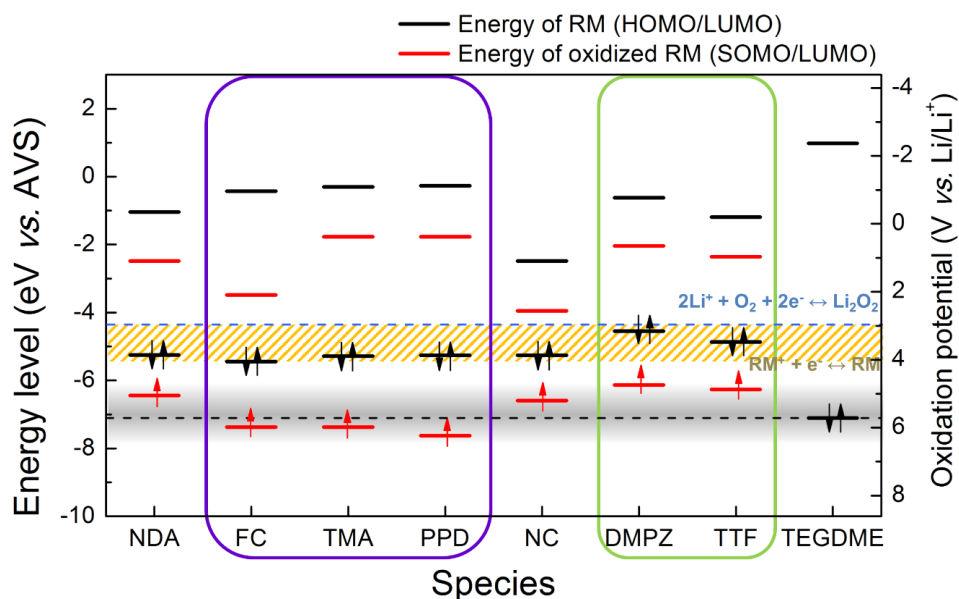


Figure 3-7. Molecular orbital energies of RMs and TEGDME. HOMO and LUMO energies of original RMs (black line) and first oxidized RMs (red line) in TEGDME electrolyte based on DFT calculations. The dotted blue line represents the theoretical formation energy of Li₂O₂ ($2\text{Li}^+ + \text{O}_2 + 2\text{e}^- \leftrightarrow \text{Li}_2\text{O}_2$, 2.96 V vs. Li/Li⁺), and the redox potentials of $\text{RM}^+ + \text{e}^- \leftrightarrow \text{RM}$ reactions are indicated in yellow region, which are required to be higher than 2.96 V. The dotted black line represents the HOMO energy of TEGDME. When SOMO of oxidized RM is lower than HOMO of TEGDME, the RM can react with the electrolyte (purple box), otherwise, the RM is stable in TEGDME (green box). Black shaded area indicates the relative instability of molecules possibly reacting with TEGDME.

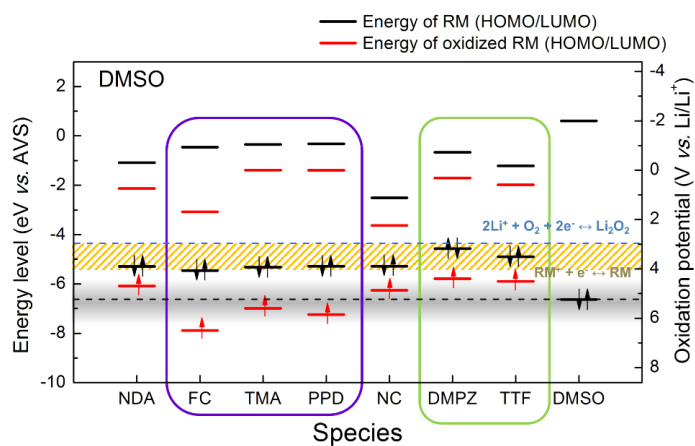


Figure 3-8. HOMO and LUMO energies of original RMs (black line) and first oxidized RMs (red line) in DMSO electrolyte using DFT calculations. The dotted blue and black lines represent the theoretical formation energy of Li₂O₂ and the HOMO energy of DMSO, respectively.

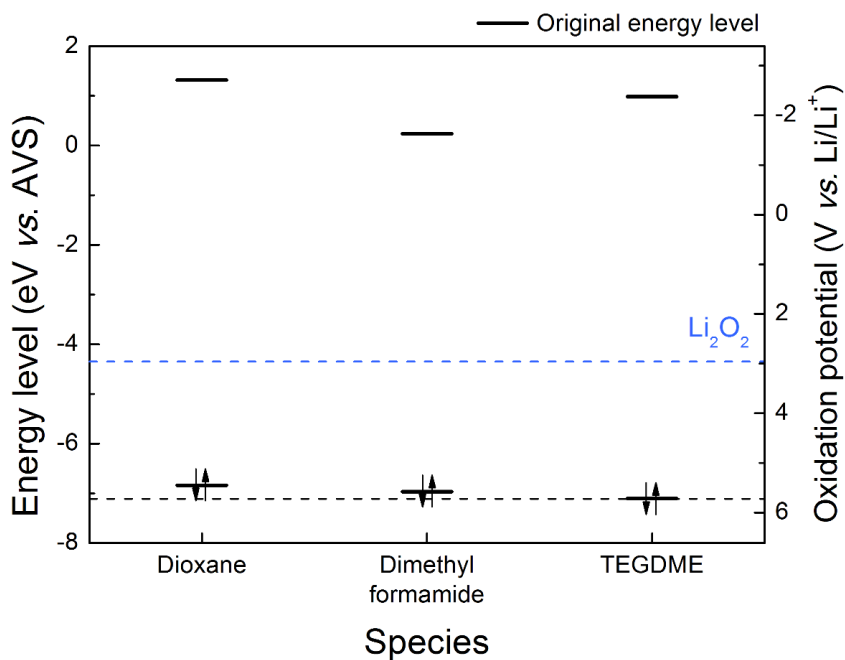


Figure 3-9. HOMO and LUMO energies of 1,4-dioxane and N,N-dimethylformamide in TEGDME electrolyte using DFT calculations. 1,4-dioxane and N,N-dimethylformamide have high I.E. values of ~6.8 and ~6.9 eV in TEGDME, respectively, which are quite high compared with those of the other RM candidates described in Figure 3-7. Therefore, it is believed that these molecules are not oxidized under a typical voltage window (2.0–4.5 V), as demonstrated in Figure 3-4c.

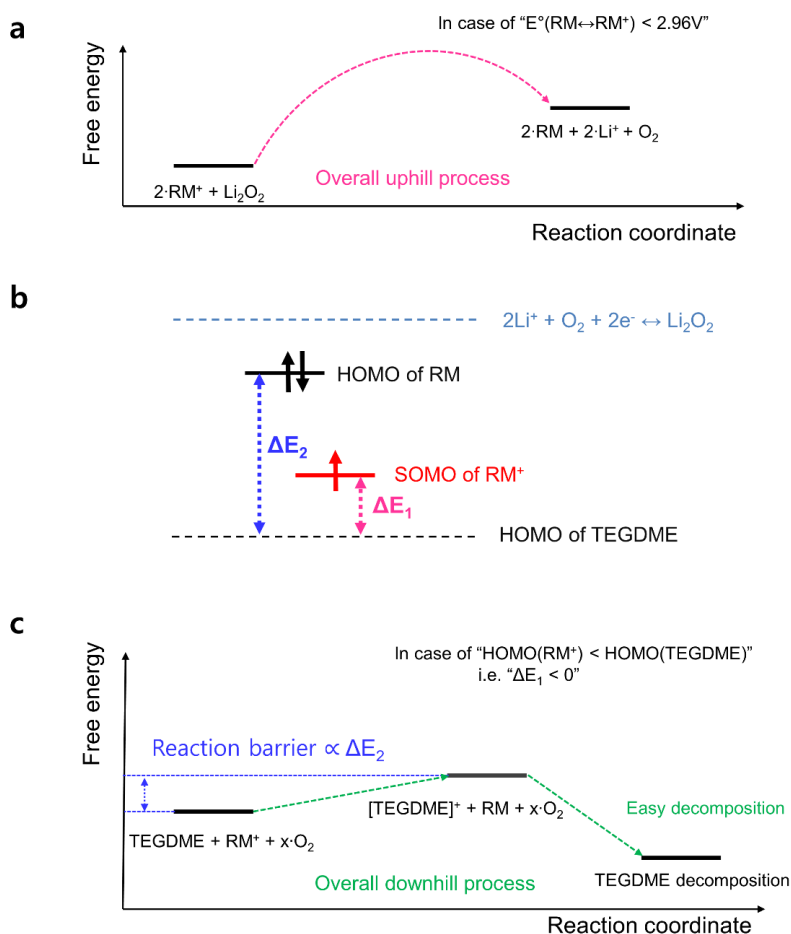
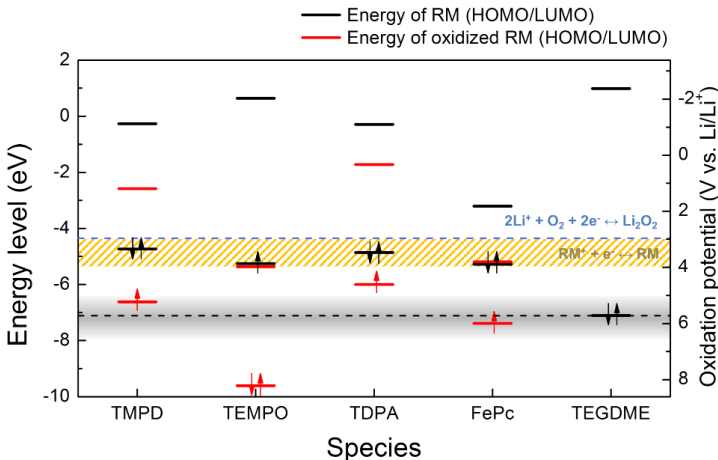


Figure 3-10. Schematic energy diagram of (a) $2\text{RM}^+ + \text{Li}_2\text{O}_2 \leftrightarrow 2\text{RM} + 2\text{Li}^+ + \text{O}_2$ reaction in case of $E^\circ(\text{RM} \leftrightarrow \text{RM}^+) < 2.96\text{ V}$ (b) relative MO position of RM/TEGDME, and (c) TEGDME decomposition reaction in the presence with RM^+ whose HOMO is lower than that of the solvent. See Supplementary Note 2 for detailed discussion.

a



b

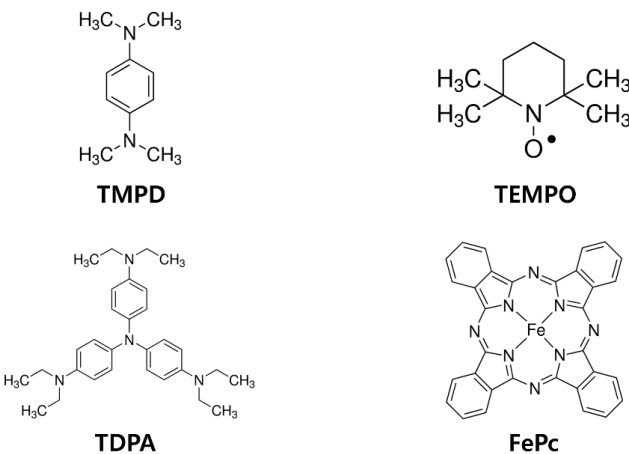


Figure 3-11. (a) HOMO and LUMO energies and (b) molecular structures of TMPD, TEMPO, TDPA and FePc in TEGDME electrolyte based on DFT calculations. See Supplementary Note 3 for detailed discussion.

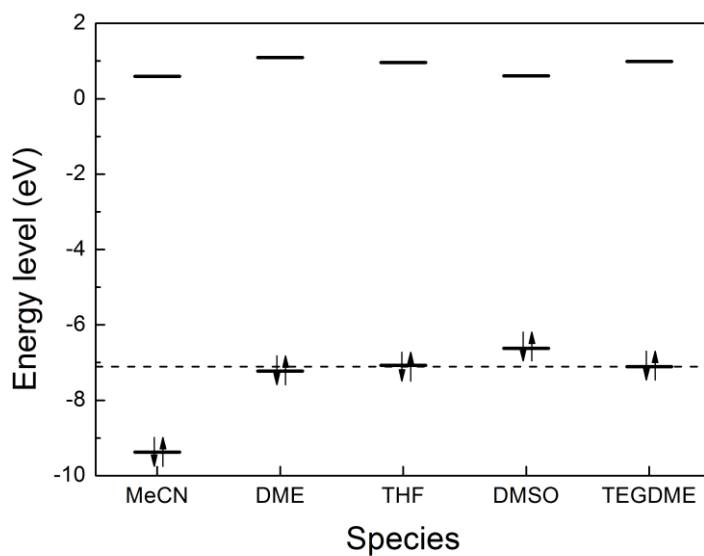


Figure 3-12. The HOMO/LUMO energies of five representative solvents used in the Li-O₂ battery. See Supplementary Note 4 for detailed discussion.

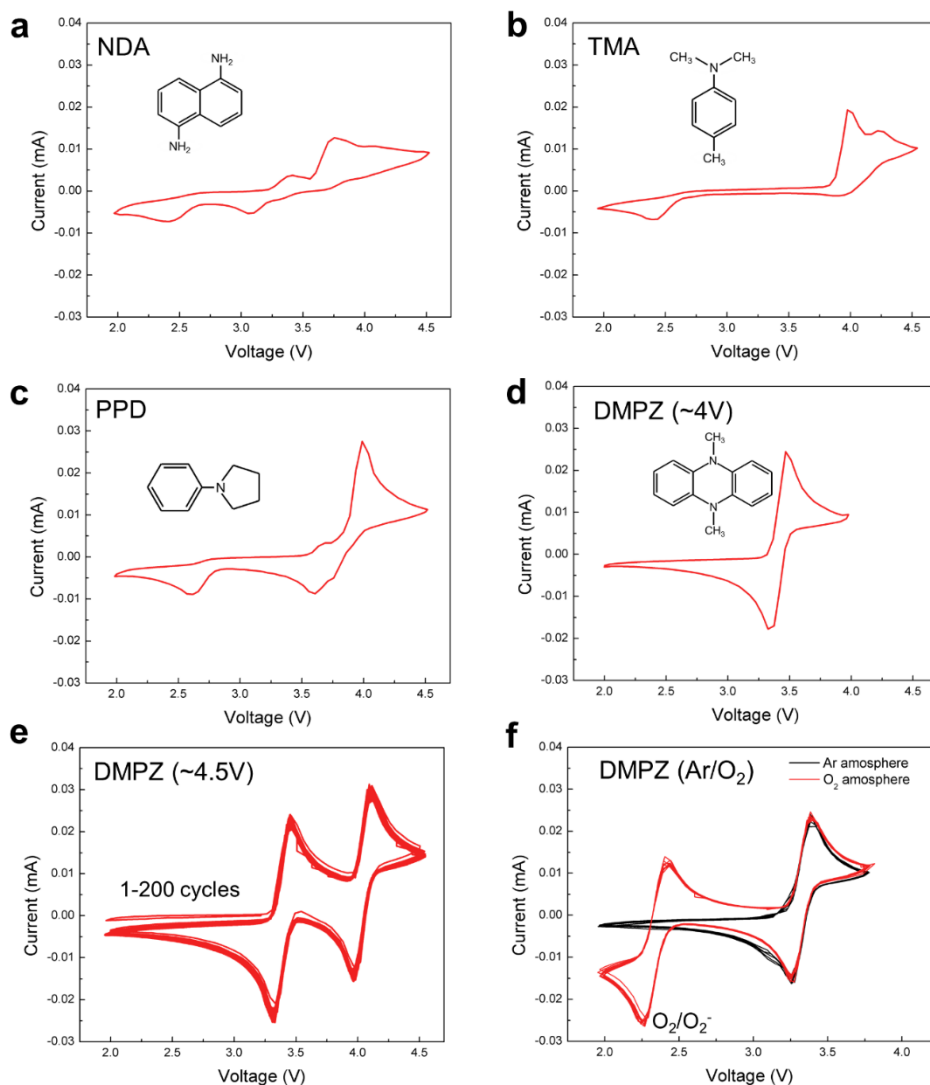


Figure 3-13. Cyclic voltammetries of RMs. CV and chemical structure of (a) NDA, (b) TMA, (c) PPD, and (d) DMPZ in 1 M LiTFSI/TEGDME under an Ar atmosphere at a scan rate of 100 mV s⁻¹. (e) CV of DMPZ for 200 cycles in the voltage range of 2.0–4.5 V vs. Li/Li⁺. (f) CV of DMPZ in 1 M TBATFSI/DMSO under an Ar and an O₂ atmosphere.

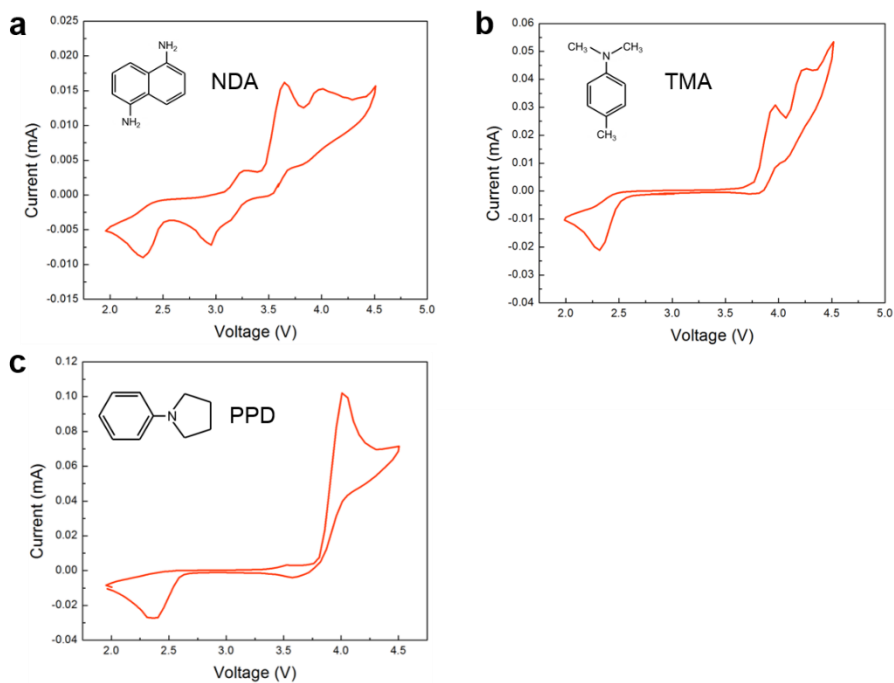


Figure 3-14. CV of (a) NDA, (b) TMA, and (c) PPD in 0.1 M TBATFSI/DMSO under Ar atmosphere at a scan rate of 100 mV s^{-1} . In total, 1 mM of the RMs was added to the electrolyte.

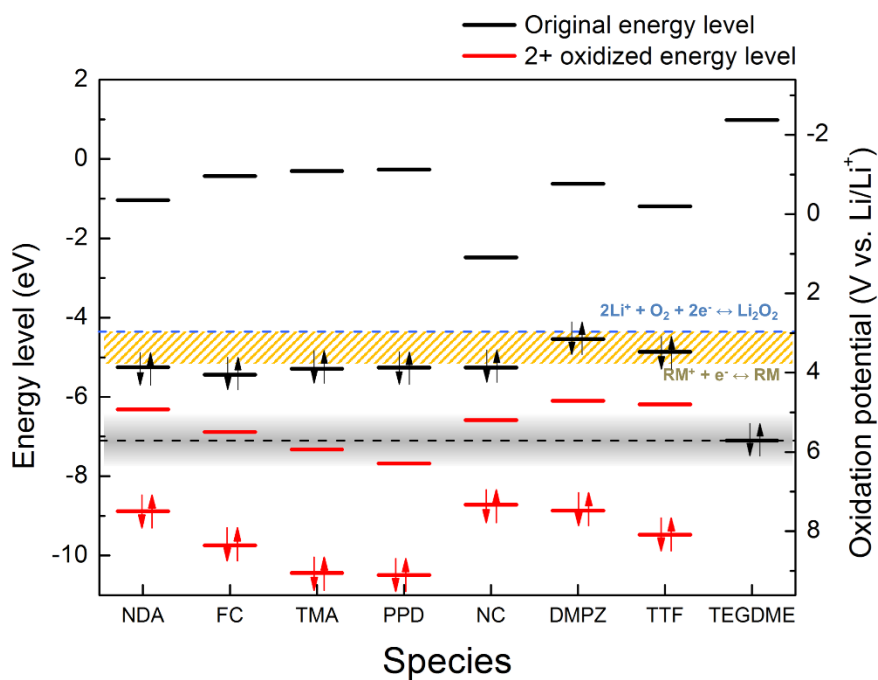


Figure 3-15. HOMO and LUMO energies of original RMs (black line) and second oxidized RMs (red line) in TEGDME electrolyte based on DFT calculations. See Supplementary Note 5 for detailed discussion.

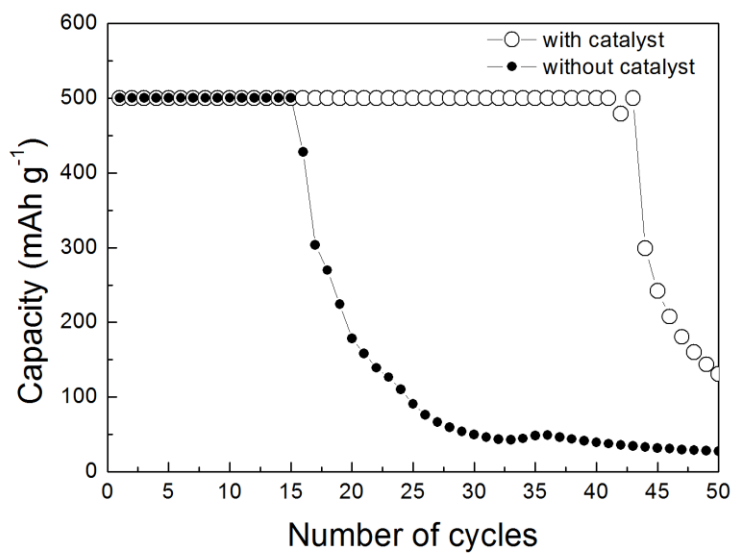


Figure 3-16. Cyclability of the Li-O₂ cells with and without DMPZ catalyst. The capacity is limited to 500 mAh g⁻¹ at a constant current of 0.2 mA cm⁻² in an oxygen atmosphere. See Supplementary Note 6 for detailed discussion.

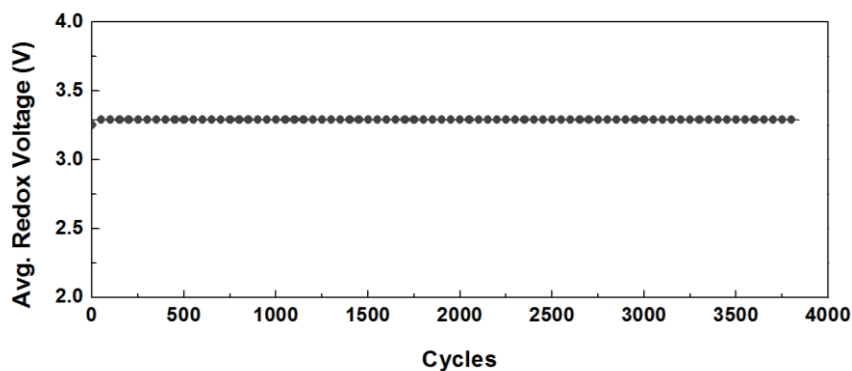


Figure 3-17. Average redox voltage of DMPZ/DMPZ⁺ along with the cycle numbers.

The scan rate was constantly maintained at 100 mV s⁻¹. We investigated the stability of DMPZ/DMPZ⁺ redox under the prolonged cycles. Figure 3-17 shows that the redox potentials of DMPZ/DMPZ⁺ is highly stable for a few thousands cycles. Average redox voltages of DMPZ/DMPZ⁺ are constantly maintained, which implies that the redox of DMPZ/DMPZ⁺ is reversible and stable.

3.3.4 Catalytic effect of DMPZ for Li–O₂ batteries

Based on the prescreening calculation and experimental verification, we finally selected DMPZ as the most effective catalyst among the candidates and investigated its catalytic activity in a practical Li–O₂ cell. Figure 3-18 presents the corresponding results from X-ray diffraction (XRD), the galvanostatic intermittent titration technique (GITT) and field-emission scanning electron microscopy (FESEM). The air cathode in each state was carefully washed with TEGDME solvent and examined without exposure to air. Although the XRD pattern of the as-prepared electrode corresponds only to that of the Ni mesh substrate, new sets of peaks corresponding to Li₂O₂ were clearly visible after a discharge (Figure 3-18a). After the re-charge, the peaks completely disappeared, suggesting that DMPZ could effectively decompose Li₂O₂ during a charge process. The reversible formation and decomposition of Li₂O₂ is additionally supported by the GITT results (Figure 3-18b). During the discharge (blue line) and charge (red line) processes, the relaxation potentials of each step approached the theoretical formation voltage of Li₂O₂ (2.96 V, dotted line), as illustrated in the inset of Figure 3-18b, indicating the primary reactions involving Li₂O₂ during the cycle.

The chemical reaction of RM⁺ with Li₂O₂ and its recovery to RM was also hinted at from the over-charging experiment of DMPZ beyond its intrinsic redox capability without discharge as shown in Figure 3-19. Furthermore, the morphology study of the air cathode in Figures 3-18c–e supports the conclusion that DMPZ is capable of

efficiently decomposing Li_2O_2 during the charge process. The as-prepared air electrode in Figure 3-18c consists of Ketjen black carbon on the electrode surface with pores and empty spaces. The formation of the toroidal-like Li_2O_2 discharge product after the discharge is consistent with previous reports as observed in Figure 3-18d. [10, 65] However, the discharge products were obviously decomposed after the charge (Figure 3-18e). Additional information on property of DMPZ is given in Figure 3-20 ~ Figure 3-23.

The basic rules and conditions for the design of a RM are proposed as follows. 1) As a first screening, organic molecules with I.E. values of approximately 6 eV in vacuum can be considered as RM candidates. Note that redox potential of Li/Li^+ and I.E. of molecules alter with the selection of solvent, hence one should elaborately consider the effect of solvent on redox potential when screening a redox mediator with I.E. of molecules (6 eV criterion is particularly for low donor number solvents such as glyme-based ones. See Table 3-3 and Figure 3-24). 2) The I.E. values of the RMs should be less than the formation energy of Li_2O_2 . A smaller gap between these values is preferred with regards to energy efficiency. 3) The SOMO energy level of RM^+ should be higher than HOMO of the electrolyte to avoid side reactions. Better chemical stability is achieved for HOMO energy levels further from that of the electrolyte. Finally, 4) these molecules should be soluble and stable in the electrolyte in an oxygen atmosphere. The guidelines for designing a RM presented here are based on a simple physical parameter, the I.E. values of molecules, which are easily

accessible, and are applicable to further development of series of soluble catalysts.

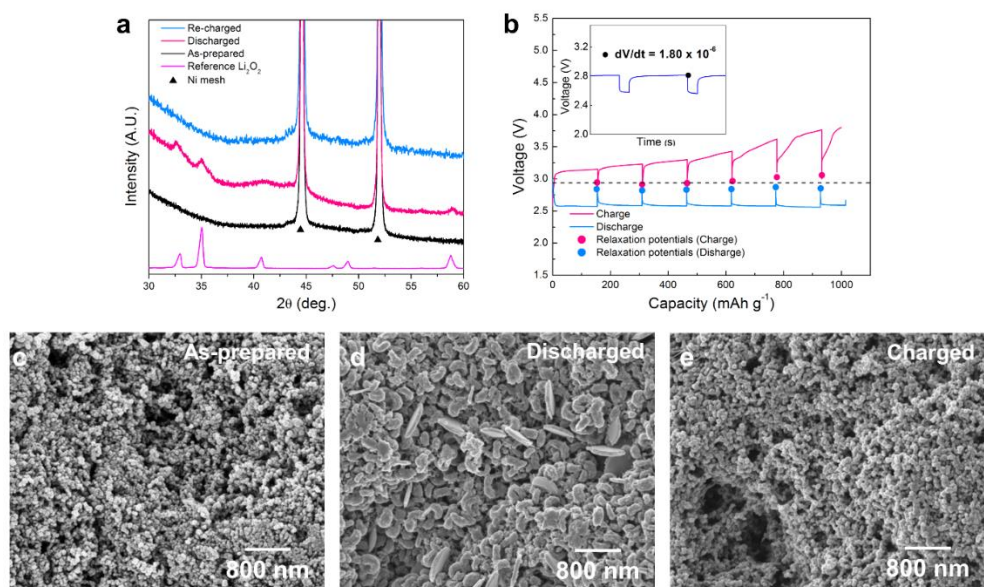


Figure 3-18. Effects of DMPZ as a catalyst for Li-O₂ battery. (a) *Ex situ* XRD patterns of Li-O₂ cells using DMPZ catalyst: as-prepared, after discharge, and after re-charge. (b) GITT voltage profile of Li-O₂ cell using DMPZ catalyst during discharge (blue) and charge (red). The dotted line is the theoretical formation voltage of Li_2O_2 (2.96 V vs. Li/Li^+) and the inset presents a voltage vs. time plot. FESEM images of the air electrode: (c) as-prepared, (d) after discharge, and (e) re-charge at same magnification.

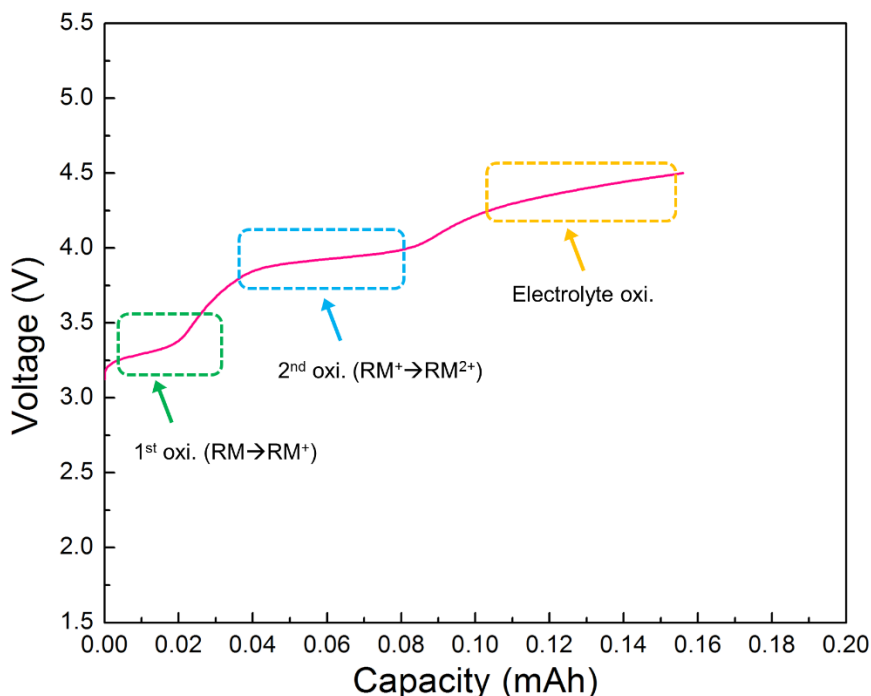


Figure 3-19. Electrochemical oxidation of DMPZ to 4.5 V in TEGDME electrolyte.

The theoretical capacity that DMPZ alone can contribute by the oxidation to DMPZ^+ and DMPZ^{2+} in the absence of Li_2O_2 is approximately 0.1 mAh based on the amount of RMs used in the Li- O_2 cell. Accordingly, the capacity from the intrinsic DMPZ oxidation is close to 0.1 mAh, as shown in Figure 3-19, followed by the electrolyte oxidation in the continuing charge over 4.2 V. Considering that the capacity of the Li- O_2 cell in Figure 3-42c is 1 mAh, which is 10 times higher than the possible capacity from RM, the charge capacity with the low overpotential in Figure 3-4c clearly demonstrates a continuous and simultaneous reduction of DMPZ^+ to DMPZ by reacting with Li_2O_2 during the charge process.

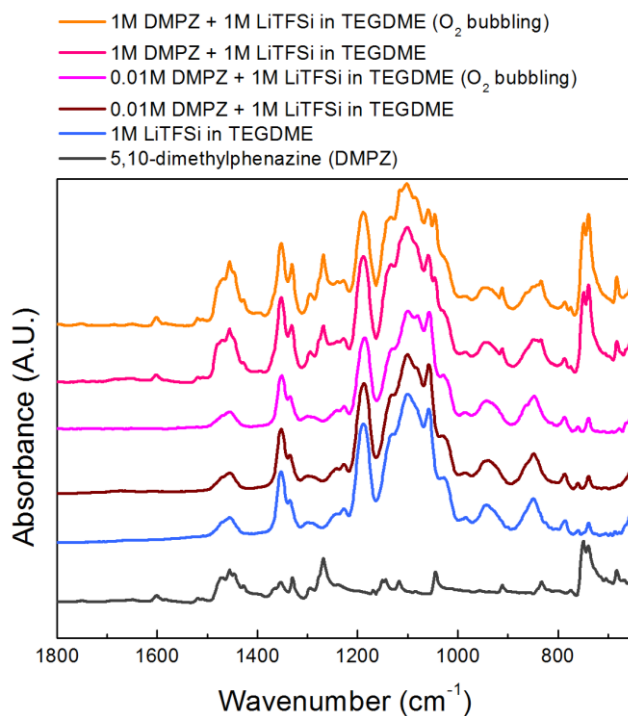


Figure 3-20. FT-IR spectra of DMPZ in the range of 1800–650 cm^{-1} . The spectra were obtained after dissolving the RMs in TEGDME electrolyte with Ar and O_2 bubbling. The stability of DMPZ in the presence of oxygen was first examined with 0.01M and 1M concentration of DMPZ in TEGDME-based electrolyte. We dissolved DMPZ in the electrolyte and bubbled with O_2 for 1 hour before carrying out FTIR measurements. Figure 3-20 shows that there is no dominant change in the peaks from both DMPZ and electrolyte, which indicates the stability of DMPZ with the oxygen in the electrolyte.

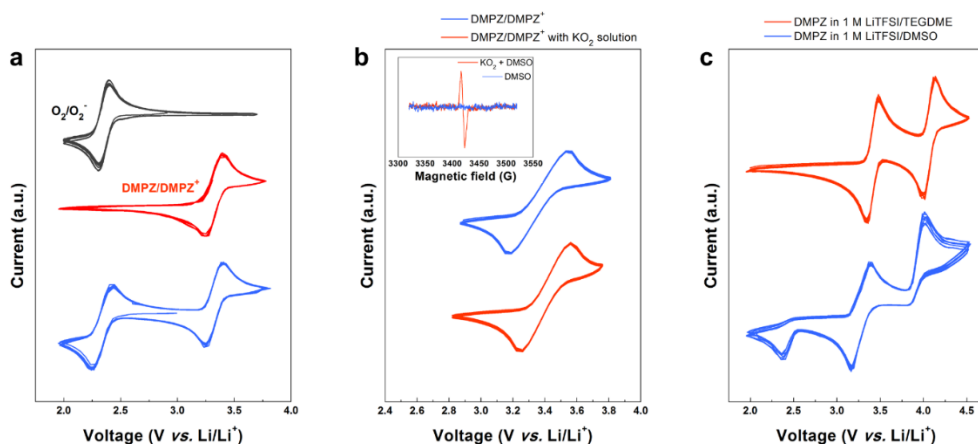


Figure 3-21. a) Cyclic voltammogram of oxygen alone (black), DMPZ with no oxygen present (red), and DMPZ (blue) under an O_2 atmosphere in TEGDME electrolyte. b) Cyclic voltammogram of DMPZ in DMSO electrolyte without (blue) and with (red) the chemically synthesized oxygen radicals. (Inset: ESR signal of the chemically generated oxygen radicals.) c) Cyclic voltammogram of DMPZ in different electrolytes of TEGDME and DMSO under an Ar atmosphere. The three electrodes compose of Pt counter and gold working electrodes with Ag/Ag^+ in acetonitrile solution as a reference electrode. The scan rate was maintained at 100 mV s^{-1} . See Supplementary Note 7 for detailed discussion.

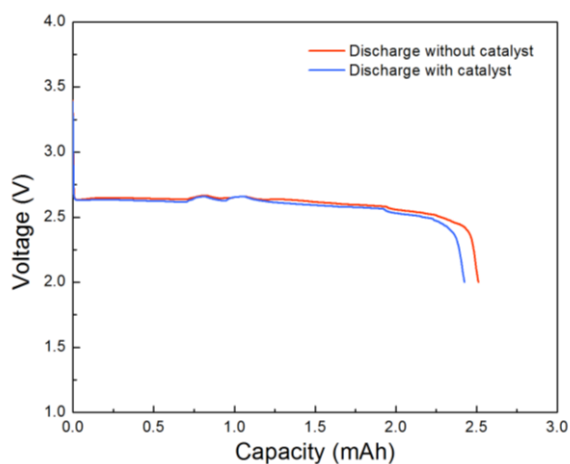


Figure 3-22. Discharge profiles of the cells with and without DMPZ catalyst in an oxygen atmosphere at a constant rate of 0.2 mA/cm^2 . See Supplementary Note 8 for detailed discussion.

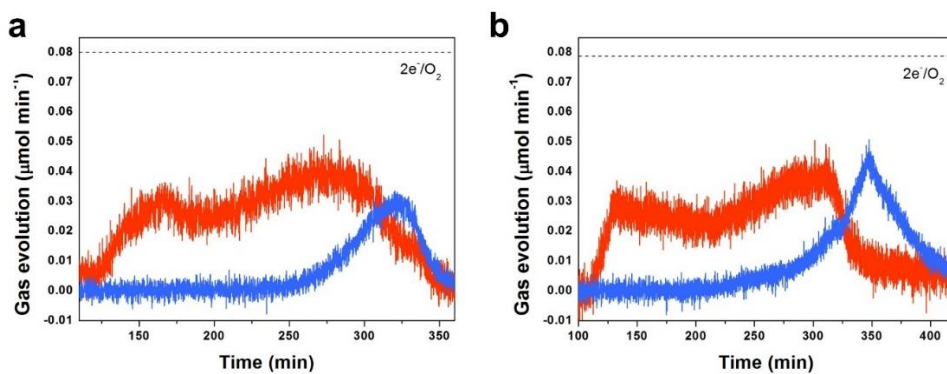


Figure 3-23. DEMS results of Li-O₂ cells during charge (a) with and (b) without DMPZ catalyst. Each cell was discharged to 1mAh and recharge to the same capacity at a current density of 0.2 mA cm⁻². See Supplementary Note 9 for detailed discussion.

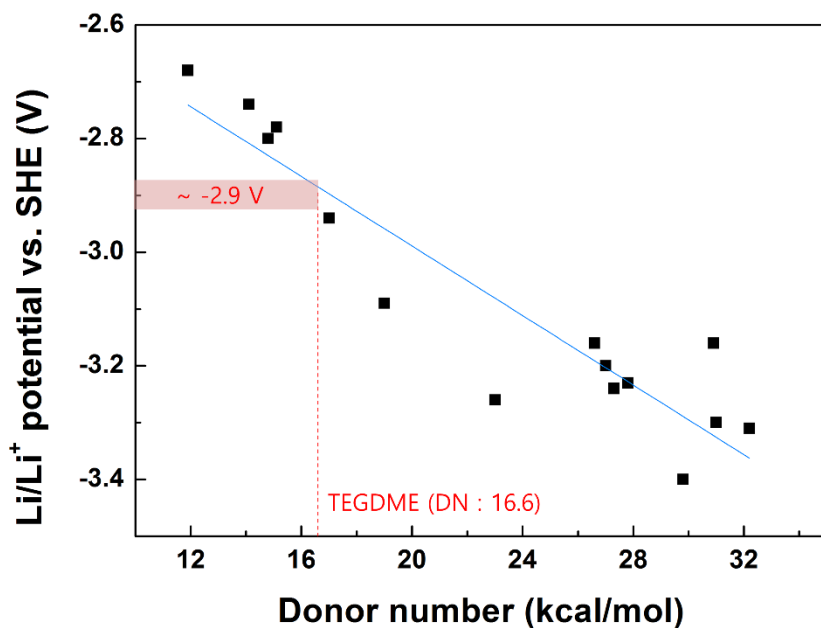


Figure 3-24. Relationship between donor number of various non-aqueous solvents and Li/Li⁺ redox potential vs. SHE in each solvent. While the redox potential of Li/Li⁺ vs. SHE in TEGDME electrolyte was not precisely reported, it can be derived from the relationship between the donor number of solvent and Li/Li⁺ redox potential in each solvent. The redox potential of Li/Li⁺ vs. SHE in TEGDME can be interpolated to around -2.9 V, which is similar to that in water. See Supplementary Note 9 for detailed discussion.

3.3.5 Supplementary Notes

Supplementary Note 1. Discrepancy between experimental and calculated voltages.

Experimental potential data for Table 3-2 were taken from Figure 3-4b in the manuscript, while calculated potential data were predicted from ionization energy and HOMO level of molecules. The discrepancy among redox potentials from the three methods was ~0.3 V, which is attributed to intrinsic DFT errors, e.g. spin contamination, the correlation effect of electrons in molecular orbital, implicit solvation assumption, etc. [40]

While the discrepancy of the first redox potential between calculation and experiment was within ~0.3 V, the calculated second ionization potential of DMPZ was notably higher than the experimental value (~4.1 V). This discrepancy can be attributed to the particularly strong interaction of DMPZ^{2+} with salt anions in the electrolyte, which was neglected in the HOMO calculation. The high valent DMPZ^{2+} ion has the stronger interaction with salt anions and can be stabilized lowering the redox potential.

Supplementary Note 2. Reaction energetics of RM, Li₂O₂ and TEGDME.

The catalytic activity of RM is determined by the relative HOMO energy state of RM not that of RM⁺ vs. the oxidation potential of Li₂O₂. It is because, when the redox potential of RM \leftrightarrow RM⁺ + e⁻ is lower than that of Li₂O₂ \leftrightarrow 2Li⁺ + O₂ + 2e⁻ (*i.e.* the formation of Li₂O₂ is thermodynamically more favorable than the reduction of RM⁺), the decomposition of Li₂O₂ via the reduction of RM⁺ is the uphill process in the overall energy scale of the reaction. As schematically depicted in Figure 3-10a, even if SOMO level of RM⁺ is located below the Li₂O₂ energy, thus, the electron prone to be transferred from Li₂O₂ to RM⁺ reducing to RM and oxidizing Li₂O₂, the overall energy of products (2RM + 2Li⁺ + O₂) becomes higher than the reactants (2RM⁺ + Li₂O₂) simply because the formation of Li₂O₂ is thermodynamically more favorable than the reduction of RM⁺ (*i.e.* redox potential of RM \leftrightarrow RM⁺ + e⁻ is lower than that of Li₂O₂ \leftrightarrow 2Li⁺ + O₂ + 2e⁻). In this respect, the decomposition of Li₂O₂ should not occur if the oxidation potential of RM is below the energy level of Li₂O₂.

The situation is slightly different in the case of TEGDME decomposition as shown in Figure 3-10b-c. In Figure 3-10b, the relative position of HOMO of RM⁺ (and RM) vs. that of TEGDME is denoted as ΔE_1 and ΔE_2 , respectively, for the clarity of the discussion. When the ΔE_1 is positive, *i.e.* the HOMO of RM⁺ lies above that of TEGDME, the decomposition of TEGDME does not occur due to the absence of electron transfer as mentioned in the main text. Let us consider the case that ΔE_1 is negative and ΔE_2 is positive. In this case, the reduction of RM⁺ would increase the

overall energy of the system similar to the case above (if the electron transfer from TEGDME to RM^+ occurs). However, it should be noted that the oxidation of TEGDME molecules easily triggers sequential side reactions leading to the decomposition of the electrolyte, thus the process does not go back to the initial condition. It is well known that the solvents in Li-O₂ cells is highly vulnerable to H-abstraction and nucleophilic attack of oxygen radical and upon the oxidation of solvents they become more vulnerable triggering sequential side reactions. [38, 55-57, 66] Especially in the presence of O₂ in the cell, it is expected that the decomposition of TEGDME can readily occur by the nucleophilic attack of oxygen molecule or radicals.

One thing that should be noted, nevertheless, is that the temporary increase of the energy in the intermediate state plays a role of kinetic barrier of the TEGDME decomposition as depicted in Figure 3-10c. As discussed above, the uphill energy is proportional to how far the HOMO level of RM is located from the oxidation potential of TEGDME. (i.e. ΔE_2) In this respect, the higher ΔE_2 is, the more resistant to the TEGDME decomposition. On the other hand, if ΔE_2 is too large so that the HOMO level lies above the Li₂O₂ potential, the RM is not active. It implies that the HOMO level of RM should be more carefully considered and it can be the indirect descriptor for the stability of RM with respect to the electrolyte.

Supplementary Note 3. Stability of TMPD, TEMPO, TDPA and FePc.

The HOMOs of all four molecules in neutral state were lower than electron energy of Li_2O_2 formation, implying that all the molecules are capable of decomposing Li_2O_2 in the oxidized form. We also examined the stability of the four molecules as following. As mentioned in the manuscript, although the HOMO of TMPD^+ is slightly higher than HOMO of TEGDME, TMPD^+ can decompose TEGDME because the HOMO of TMPD^+ is located in the vicinity of HOMO of TEGDME (grey region). It corresponds well with the previous paper reporting the low efficiency of TMPD compared to that of TTF. [22] In the case of TEMPO, it has a partially filled HOMO state in the neutral state unlike other RMs, thus, the HOMO of TEMPO^+ is fully occupied. It indicates that it can be stable against the TEGDME oxidation even though the HOMO of TEMPO^+ lies below that of TEGDME due to the lack of the available energy state in the HOMO of TEMPO^+ . Accordingly, experimentally it was reported that TEMPO decomposes Li_2O_2 efficiently. [27] TDPA is also predicted to be stable in TEGDME when oxidized, because the HOMO of TDPA^+ is higher than the HOMO of TEGDME, which also agrees well with experimental result. [62] In case of FePc, the HOMO of FePc^+ was predicted to be lower than the HOMO of TEGDME, however, the experiments reported a high cycle stability (~ 135 cycles) of Li- O_2 cell with FePc mediator. [28] We attribute the discrepancy to the reaction mechanism of FePc. When charged, FePc^+ was reported to react with $(\text{O}_2)^{2-}$ ion, immediately forming $(\text{FePc-O}_2)^-$ complex, then oxidize into FePc and O_2 . These

multi-step reactions cannot be predicted by our methodology, which should be studied further in the future.

Supplementary Note 4. Stability of RM with different solvents.

We selected five representative solvents used in Li-O₂ batteries and calculated their MO energies as shown in Figure 3-12. Except for the DMSO case, the HOMOs of solvents were calculated to be lower than that of TEGDME, which implies that MeCN, DME and THF are more stable from RM⁺ attack than TEGDME and DMSO is less stable. Although the HOMO of DMSO is higher than that of TEGDME, the relative location of the HOMO of RM⁺ with respect to the HOMO of DMSO is not significantly changed compared to the case of TEGDME. (Figure 3-8) It is because the HOMO level of RM⁺ is also affected by the choice of solvent due to the different dielectric constant of the solvent, and the HOMO levels of RM⁺s are all upshifted in the DMSO. Therefore, the stability of DMSO against RM⁺ would be only slightly inferior to the TEGDME case.

Supplementary Note 5. Stability of RM^{2+} with TEGDME.

The stability of an RM is determined by the relative energy level of the RM^+ with respect to that of the electrolyte, however, it should be noted that the electron transfer from the high energy state to the low energy state (from electrolyte to RM^+) can occur only when there is an available energy state present in the electron accepting molecule. In Figure 3-7, HOMO levels of all the RM^+ s have unpaired electron in the state, thus are capable of accepting the electron from the electrolyte. In this respect, the stability of RMs with fully occupied HOMO level should be carefully considered. In Figure 3-15, we plotted the molecular orbital (MO) energy diagram of the RM^{2+} including DMPZ^{2+} with respect to the TEGDME. The HOMO level of DMPZ^{2+} lies below that of the electrolyte (lower than -9 eV vs. AVS). However, the electron transfer from the electrolyte to the HOMO level of DMPZ^{2+} is not possible because the HOMO level is fully filled. Instead, the LUMO level of DMPZ^{2+} is unoccupied and available, however, it lies above the energy level of the TEGDME. Thus the DMPZ^{2+} can stay stable in TEGDME.

Supplementary Note 6. Cyclabilities of the cells with and without DMPZ.

The comparison of cyclabilities of the cells with and without DMPZ are presented in Figure 3-16. Interestingly, the cycle stability could be enhanced by about three times with the use of DMPZ catalyst at the same charge/discharge protocol using the carbon air electrode. The enhanced cyclability is attributable to the decreased charge polarization and the reduced CO_2 evolution due to the use of DMPZ catalyst, which successfully oxidizes Li_2O_2 by maintaining the low charging potential with minor side reactions. Nevertheless, the formation of unwanted discharge products, self-consuming of RMs in the anode side and the shuttle reaction need to be addressed for higher cycle stability.

Supplementary Note 7. The stability of DMPZ with reduced oxygen species.

The stability of DMPZ with reduced oxygen species was also investigated by comparing the electrochemical activities of DMPZ/DMPZ⁺ with and without oxygen radicals present by solution-based cyclic voltammetry (CV) as shown in Figure 3-21. Figure 3-21a shows the CV profile of O₂/O₂⁻ redox (black) and DMPZ/DMPZ⁺ in an Ar atmosphere (red), which shows their characteristic anodic/cathodic peaks. The CV of DMPZ under an oxygen atmosphere (blue) in the same figure demonstrates that the redox of DMPZ/DMPZ⁺ is still reversible and stable accompanying the redox of O₂/O₂⁻. It suggests that the redox of DMPZ is stably maintained even with the redox reaction of O₂/O₂⁻ in the electrolyte. In order to further demonstrate the stability of DMPZ to oxygen radicals, we chemically generated O₂⁻ in DMSO electrolyte and tested the redox activity of DMPZ/DMPZ⁺ as shown in Figure 3-21b. Oxygen radicals were chemically synthesized in the electrolyte using KO₂ powder based on the previous reports, [67, 68] and the chemically generated oxygen radicals were clearly detected by ESR measurement in the inset of Figure 3-21b. Figure 3-21b also confirms that the redox activity of DMPZ/DMPZ⁺ (red) is almost unaltered with respect to the reference (blue) suggesting a stable redox of DMPZ in the reductive atmosphere. (DMSO solvent was used in this experiment because it has been reported as a relatively stable electrolyte for oxygen radicals, and it could dissolve KO₂ well. [67])

The stability of DMPZ was further inspected according to the types of electrolytes

with different nucleophilic characters; DMSO (donor number 29.8) and TEGDME (donor number 16.6). As shown in the Figure 3-21c, the first and second redox reactions of DMPZ in TEGDME are highly reversible. On the other hand, those in DMSO are not fully reversible, while the first redox reaction is relatively stable in consistent with the Figure 3-21b. The cathodic peak from the second redox reaction of DMPZ in DMSO electrolyte disappears and new cathodic peak around 2.4 V arises. (Such cathodic peaks around 2.4V is commonly observed in the electrolyte system that suffers from proton-involving side reactions. [64]) The irreversibility of second redox reaction of DMPZ in DMSO is attributed to a strong nucleophilic attack of the solvent with high donor number (29.8) and can affect the reversibility of RM. [69] The demethylation of DMPZ at the second oxidation leads to a loss of its relevant reduction, and new peak around 2.4 V is attributable to a formed 5-methylphenazinium type product. [64] In this respect, when using DMPZ and utilizing the second redox reaction in Li-O₂ cells, TEGDME is preferred to DMSO electrolyte.

Supplementary Note 8. Effect of DMPZ on discharge process of the Li-O₂ cell.

We measured the amount of evolved oxygen gas during charging by *in situ* DEMS (Differential Electrochemical Mass Spectroscopy) analysis. In the DEMS setup, Mass spectrometer (MS) (HPR-20, Hiden Analytical) and a potentio-galvanostat (WonA Tech, WBCS 3000, Korea) were combined. (The detail setup is described in previous reports. [70, 71]) Before the gas analysis for the charging process, same discharge protocols were applied to cells with and without DMPZ. In Figure 3-22, the discharge capacities and profile shapes are shown for the two cells, which are almost similar regardless of the use of DMPZ and indicate that DMPZ has little influence during a discharge process. For the precise comparison, the discharge/charge capacity was limited to 1 mAh for the two cells which theoretically correspond to 18.6 μ mole of O₂ evolution during charging.

Supplementary Note 9. Gas analysis for the Li-O₂ cell with and without DMPZ.

Figure 3-23 shows the DEMS result for the two cells with concurrent O₂ and CO₂ evolution during the charging. The measured oxygen evolution efficiency is found to be almost similar to each other; the cell with DMPZ shows 5.76 e⁻/O₂ (6.47 μ mole) and the cell without catalyst shows 5.66 e⁻/O₂ (6.59 μ mole). While the efficiency of DMPZ decomposing pure Li₂O₂ in the electrolyte with 2.08 e⁻/O₂ was clearly demonstrated in Figure 3-6 in the manuscript, much less efficiency was observed for both cells. It indicates that the formation of Li₂CO₃ or carbonate-based byproducts that decomposes and evolves CO₂ has already occurred during the discharge process and they are inevitable regardless of the use of RM which have little influence in the discharge process as shown in Figure 3-22. Actually, it is well-known that the current state of Li-O₂ battery is facing a big hurdle of dealing with side reactions during discharge, where Li₂CO₃ and carbonate-based byproducts are formed due to the carbon contamination and electrolyte deterioration. In particular, carbon-based electrode is more vulnerable to the formation of Li₂CO₃ upon deposition of Li₂O₂ discharge product on the surface of the carbon electrode, which leads to a decreased charging efficiency.[14] Even though the gold and TiO₂ electrodes have been suggested as substitutional electrodes, other problems still persist such as the low energy density. In this respect, to avoid the formation of undesirable discharge products and clearly verify the intrinsic efficiency of RMs with Li₂O₂, we used commercialized Li₂O₂ powder in our experiment (Figure 3-6).

One thing that is worthy to note is that, in spite of the similar oxygen efficiency between the two cells, the use of DMPZ could reduce CO₂ evolution during charging compared to the cell without DMPZ. The Li-O₂ cell with DMPZ evolved only one third of CO₂ (1.02 μ mole) compared to the cell without DMPZ (3.44 μ mole). The decreased CO₂ evolution is attributable to the reduced charge polarization which lowers the charging voltage of the cell. It has been known that the carbon corrosion is accelerated in the high voltage charging above 3.5 V, where the primary source of carbon in the CO₂ evolution is the carbon electrode. [72]

3.4 Conclusion

We proposed general design principles for finding a soluble catalyst and demonstrated their validity using DFT calculations and experimental verification. The I.E. was suggested as the key descriptor for designing a catalyst, where specific organics with a certain range of I.E. values (5.8–6.8 eV) can be used as soluble catalysts. Furthermore, the HOMO energy level of the catalyst should be considered in comparison with the formation energy of Li_2O_2 and the HOMO energy of the electrolyte. Based on this guideline, DMPZ was successfully identified with a remarkably low overpotential and stability in the Li-O_2 cell. We believe that the verification of key factors for designing a RM will open up a new avenue to the development of effective novel catalysts and advanced Li-O_2 batteries with high efficiency and long cycle life.

3.5 References

- [1] Liu, T.; Leskes, M.; Yu, W.; Moore, A. J.; Zhou, L.; Bayley, P. M.; Kim, G.; Grey, C. P., Cycling Li-O₂ batteries via LiOH formation and decomposition. *Science* **2015**, 350, (6260), 530-533.
- [2] Bruce, P. G.; Freunberger, S. A.; Hardwick, L. J.; Tarascon, J.-M., Li-O₂ and Li-S batteries with high energy storage. *Nature Materials* **2012**, 11, (1), 19-29.
- [3] Black, R.; Oh, S. H.; Lee, J.-H.; Yim, T.; Adams, B.; Nazar, L. F., Screening for Superoxide Reactivity in Li-O₂ Batteries: Effect on Li₂O₂/LiOH Crystallization. *Journal of the American Chemical Society* **2012**, 134, (6), 2902-2905.
- [4] Lim, H.-D.; Park, K.-Y.; Song, H.; Jang, E. Y.; Gwon, H.; Kim, J.; Kim, Y. H.; Lima, M. D.; Robles, R. O.; Lepró, X.; Baughman, R. H.; Kang, K., Enhanced Power and Rechargeability of a Li-O₂ Battery Based on a Hierarchical-Fibril CNT Electrode. *Advanced Materials* **2013**, 25, (9), 1348-1352.
- [5] Xu, J.-J.; Wang, Z.-L.; Xu, D.; Zhang, L.-L.; Zhang, X.-B., Tailoring deposition and morphology of discharge products towards high-rate and long-life lithium-oxygen batteries. *Nature Communications* **2013**, 4, 2438.
- [6] Lu, J.; Li, L.; Park, J.-B.; Sun, Y.-K.; Wu, F.; Amine, K., Aprotic and Aqueous Li-O₂ Batteries. *Chemical Reviews* **2014**, 114, (11), 5611-5640.
- [7] Li, F.; Wu, S.; Li, D.; Zhang, T.; He, P.; Yamada, A.; Zhou, H., The water catalysis at oxygen cathodes of lithium-oxygen cells. *Nature Communications* **2015**, 6, 7843.

- [8] Balaish, M.; Kraytsberg, A.; Ein-Eli, Y., A critical review on lithium-air battery electrolytes. *Physical Chemistry Chemical Physics* **2014**, 16, (7), 2801-2822.
- [9] Lim, H.-D.; Park, K.-Y.; Gwon, H.; Hong, J.; Kim, H.; Kang, K., The potential for long-term operation of a lithium-oxygen battery using a non-carbonate-based electrolyte. *Chemical Communications* **2012**, 48, (67), 8374-8376.
- [10] Aetukuri, N. B.; McCloskey, B. D.; García, J. M.; Krupp, L. E.; Viswanathan, V.; Luntz, A. C., Solvating additives drive solution-mediated electrochemistry and enhance toroid growth in non-aqueous Li-O₂ batteries. *Nat Chem* **2015**, 7, (1), 50-56.
- [11] Zhu, Y.; Liu, S.; Jin, C.; Bie, S.; Yang, R.; Wu, J., MnO_x decorated CeO₂ nanorods as cathode catalyst for rechargeable lithium-air batteries. *Journal of Materials Chemistry A* **2015**, 3, (25), 13563-13567.
- [12] Black, R.; Adams, B.; Nazar, L. F., Non-Aqueous and Hybrid Li-O₂ Batteries. *Advanced Energy Materials* **2012**, 2, (7), 801-815.
- [13] Freunberger, S. A.; Chen, Y.; Peng, Z.; Griffin, J. M.; Hardwick, L. J.; Bardé, F.; Novák, P.; Bruce, P. G., Reactions in the Rechargeable Lithium-O₂ Battery with Alkyl Carbonate Electrolytes. *Journal of the American Chemical Society* **2011**, 133, (20), 8040-8047.
- [14] McCloskey, B. D.; Speidel, A.; Scheffler, R.; Miller, D. C.; Viswanathan, V.; Hummelshøj, J. S.; Nørskov, J. K.; Luntz, A. C., Twin Problems of Interfacial Carbonate Formation in Nonaqueous Li-O₂ Batteries. *The Journal of Physical Chemistry Letters* **2012**, 3, (8), 997-1001.

- [15] Liu, S.; Wang, Z.; Yu, C.; Zhao, Z.; Fan, X.; Ling, Z.; Qiu, J., Free-standing, hierarchically porous carbon nanotube film as a binder-free electrode for high-energy Li-O₂ batteries. *Journal of Materials Chemistry A* **2013**, 1, (39), 12033-12037.
- [16] Cheng, F.; Chen, J., Lithium-air batteries: Something from nothing. *Nat Chem* **2012**, 4, (12), 962-963.
- [17] Suntivich, J.; Gasteiger, H. A.; Yabuuchi, N.; Nakanishi, H.; Goodenough, J. B.; Shao-Horn, Y., Design principles for oxygen-reduction activity on perovskite oxide catalysts for fuel cells and metal–air batteries. *Nature Chemistry* **2011**, 3, (7), 546-550.
- [18] Lu, Y.-C.; Xu, Z.; Gasteiger, H. A.; Chen, S.; Hamad-Schifferli, K.; Shao-Horn, Y., Platinum–Gold Nanoparticles: A Highly Active Bifunctional Electrocatalyst for Rechargeable Lithium–Air Batteries. *Journal of the American Chemical Society* **2010**, 132, (35), 12170-12171.
- [19] Peng, Z.; Freunberger, S. A.; Chen, Y.; Bruce, P. G., A Reversible and Higher-Rate Li-O₂ Battery. *Science* **2012**, 337, (6094), 563-566.
- [20] Ryu, W.-H.; Yoon, T.-H.; Song, S. H.; Jeon, S.; Park, Y.-J.; Kim, I.-D., Bifunctional Composite Catalysts Using Co₃O₄ Nanofibers Immobilized on Nonoxidized Graphene Nanoflakes for High-Capacity and Long-Cycle Li–O₂ Batteries. *Nano Letters* **2013**, 13, (9), 4190-4197.
- [21] McCloskey, B. D.; Scheffler, R.; Speidel, A.; Bethune, D. S.; Shelby, R. M.; Luntz, A. C., On the Efficacy of Electrocatalysis in Nonaqueous Li–O₂ Batteries. *Journal of the American Chemical Society* **2011**, 133, (45), 18038-18041.

- [22] Chen, Y.; Freunberger, S. A.; Peng, Z.; Fontaine, O.; Bruce, P. G., Charging a Li–O₂ battery using a redox mediator. *Nature Chemistry* **2013**, 5, (6), 489-494.
- [23] Lim, H.-D.; Song, H.; Kim, J.; Gwon, H.; Bae, Y.; Park, K.-Y.; Hong, J.; Kim, H.; Kim, T.; Kim, Y. H.; Lepró, X.; Ovalle-Robles, R.; Baughman, R. H.; Kang, K., Superior Rechargeability and Efficiency of Lithium–Oxygen Batteries: Hierarchical Air Electrode Architecture Combined with a Soluble Catalyst. *Angewandte Chemie International Edition* **2014**, 53, (15), 3926-3931.
- [24] Chase, G. V.; Zecevic, S.; Walker, W.; Uddin, J.; Sasaki, K. A.; Giordani, V.; Bryantsev, V.; Blanco, M.; Addison, D. D., Soluble oxygen evolving catalysts for rechargeable metal-air batteries. **2011**, U.S. Patent US2011/033821.
- [25] Wang, Y.; Xia, Y., Li-O₂ batteries: An agent for change. *Nat Chem* **2013**, 5, (6), 445-447.
- [26] Yu, M.; Ren, X.; Ma, L.; Wu, Y., Integrating a redox-coupled dye-sensitized photoelectrode into a lithium–oxygen battery for photoassisted charging. *Nature Communications* **2014**, 5, 5111.
- [27] Bergner, B. J.; Schürmann, A.; Peppler, K.; Garsuch, A.; Janek, J., TEMPO: A Mobile Catalyst for Rechargeable Li-O₂ Batteries. *Journal of the American Chemical Society* **2014**, 136, (42), 15054-15064.
- [28] Sun, D.; Shen, Y.; Zhang, W.; Yu, L.; Yi, Z.; Yin, W.; Wang, D.; Huang, Y.; Wang, J.; Wang, D.; Goodenough, J. B., A Solution-Phase Bifunctional Catalyst for Lithium–Oxygen Batteries. *Journal of the American Chemical Society* **2014**, 136, (25), 8941-8946.

- [29] Frisch, M.; Trucks, G.; Schlegel, H.; Scuseria, G.; Robb, M.; Cheeseman, J.; Scalmani, G.; Barone, V.; Mennucci, B.; Petersson, G., Gaussian 09 Revision D. **2009**, 01.
- [30] Lee, C.; Yang, W.; Parr, R. G., Development of the Colle-Salvetti correlation-energy formula into a functional of the electron density. *Physical Review B* **1988**, 37, (2), 785-789.
- [31] Stephens, P. J.; Devlin, F. J.; Chabalowski, C. F.; Frisch, M. J., Ab Initio Calculation of Vibrational Absorption and Circular Dichroism Spectra Using Density Functional Force Fields. *Journal of Physical Chemistry* **1994**, 98, (45), 11623-11627.
- [32] Becke, A. D., Density-functional thermochemistry. III. The role of exact exchange. *The Journal of Chemical Physics* **1993**, 98, (7), 5648-5652.
- [33] Schäfer, A.; Huber, C.; Ahlrichs, R., Fully optimized contracted Gaussian basis sets of triple zeta valence quality for atoms Li to Kr. *The Journal of Chemical Physics* **1994**, 100, (8), 5829-5835.
- [34] Schäfer, A.; Horn, H.; Ahlrichs, R., Fully optimized contracted Gaussian basis sets for atoms Li to Kr. *The Journal of Chemical Physics* **1992**, 97, (4), 2571-2577.
- [35] Klauminzer, B.; Kröner, D.; Saalfrank, P., (TD-)DFT Calculation of Vibrational and Vibronic Spectra of Riboflavin in Solution. *Journal of Physical Chemistry B* **2010**, 114, (33), 10826-10834.
- [36] Trasatti, S., The absolute electrode potential: an explanatory note (Recommendations 1986). *Pure Appl. Chem.* **1986**, 58, (7), 955-966.

- [37] Khetan, A.; Pitsch, H.; Viswanathan, V., Identifying Descriptors for Solvent Stability in Nonaqueous Li–O₂ Batteries. *Journal of Physical Chemistry Letters* **2014**, 5, (8), 1318-1323.
- [38] Khetan, A.; Pitsch, H.; Viswanathan, V., Solvent Degradation in Nonaqueous Li-O₂ Batteries: Oxidative Stability versus H-Abstraction. *The Journal of Physical Chemistry Letters* **2014**, 5, (14), 2419-2424.
- [39] Gritzner, G., Standard electrode potentials of M⁺|M couples in non-aqueous solvents (molecular liquids). *Journal of Molecular Liquids* **2010**, 156, (1), 103-108.
- [40] Cramer, C. J., *Essentials of Computational Chemistry: Theories and Models*. 2nd ed.; Wiley: 2014.
- [41] Paduszek, B.; Kalinowski, M. K., Redox behaviour of phenothiazine and phenazine in organic solvents. *Electrochimica Acta* **1983**, 28, (5), 639-642.
- [42] Yoo, E.; Nakamura, J.; Zhou, H., N-Doped graphene nanosheets for Li-air fuel cells under acidic conditions. *Energy & Environmental Science* **2012**, 5, (5), 6928-6932.
- [43] Cederbaum, L. S.; Domcke, W., Theoretical Aspects of Ionization Potentials and Photoelectron Spectroscopy: A Green's Function Approach. **1977**, 39, 205-344.
- [44] Gleiter, R.; Kobayashi, M.; Spanget-Larsen, J.; Ferraris, J. P.; Bloch, A. N.; Bechgaard, K.; Cowan, D. O., Photoelectron and electronic absorption spectra of tetrathiafulvalene and related compounds. *Ber. Bunsenges. Phys. Chem.* **1975**, 79, (12), 1218-1226.
- [45] Rabalais, J. W.; Werme, L. O.; Bergmark, T.; Karlsson, L.; Hussain, M.;

Siegbahn, K., Electron Spectroscopy of Open-Shell Systems: Spectra of Ni(C₅H₅)₂, Fe(C₅H₅)₂, Mn(C₅H₅)₂, and Cr(C₅H₅)₂. *The Journal of Chemical Physics* **1972**, 57, (3), 1185-1192.

[46] Foster, R., Ionization Potentials of Electron Donors. *Nature* **1959**, 183, (4670), 1253-1253.

[47] Maier, J. P., Photoelectron Spectroscopy of peri-Amino Naphthalenes. *Helv. Chim. Acta* **1974**, 57, (4), 994-1003.

[48] Egde, R.; Green, J. C.; Rao, C. N. R., Photoelectron spectra of substituted benzenes. *Chem. Phys. Lett.* **1975**, 33, (3), 600-607.

[49] Rozeboom, M. D.; Houk, K. N.; Searles, S.; Seyedrezai, S. E., Photoelectron spectroscopy of N-aryl cyclic amines. Variable conformations and relationships to gas- and solution-phase basicities. *Journal of the American Chemical Society* **1982**, 104, (12), 3448-3453.

[50] Matsen, F. A., Electron Affinities, Methyl Affinities, and Ionization Energies of Condensed Ring Aromatic Hydrocarbons. *The Journal of Chemical Physics* **1956**, 24, (3), 602-606.

[51] Fraser-Monteiro, M. L.; Fraser-Monteiro, L.; Butler, J. J.; Baer, T.; Hass, J. R., Thermochemistry and dissociation dynamics of state-selected C₄H₈O₂⁺ ions. 1. 1,4-Dioxane. *J. Phys. Chem.* **1982**, 86, (5), 739-747.

[52] Watanabe, K.; Nakayama, T.; Mottl, J., Ionization potentials of some molecules. *J. Quant. Spectry. Radiative Transfer* **1962**, 2, (4), 369-382.

[53] Chen, Y.; Shen, L.; Li, X., Effects of Heteroatoms of Tetracene and

Pentacene Derivatives on Their Stability and Singlet Fission. *Journal of Physical Chemistry A* **2014**, 118, (30), 5700-5708.

[54] Liang, Z.; Zhao, W.; Wang, S.; Tang, Q.; Lam, S.-C.; Miao, Q., Unexpected Photooxidation of H-Bonded Tetracene. *Organic Letters* **2008**, 10, (10), 2007-2010.

[55] McCloskey, B. D.; Bethune, D. S.; Shelby, R. M.; Mori, T.; Scheffler, R.; Speidel, A.; Sherwood, M.; Luntz, A. C., Limitations in Rechargeability of Li-O₂ Batteries and Possible Origins. *The Journal of Physical Chemistry Letters* **2012**, 3, (20), 3043-3047.

[56] Bryantsev, V. S.; Uddin, J.; Giordani, V.; Walker, W.; Addison, D.; Chase, G. V., The Identification of Stable Solvents for Nonaqueous Rechargeable Li-Air Batteries. *Journal of the Electrochemical Society* **2013**, 160, (1), A160-A171.

[57] Bryantsev, V. S., Predicting the stability of aprotic solvents in Li-air batteries: pK_a calculations of aliphatic C–H acids in dimethyl sulfoxide. *Chemical Physics Letters* **2013**, 558, 42-47.

[58] Bryantsev, V. S.; Giordani, V.; Walker, W.; Blanco, M.; Zecevic, S.; Sasaki, K.; Uddin, J.; Addison, D.; Chase, G. V., Predicting Solvent Stability in Aprotic Electrolyte Li–Air Batteries: Nucleophilic Substitution by the Superoxide Anion Radical (O₂•[–]). *The Journal of Physical Chemistry A* **2011**, 115, (44), 12399-12409.

[59] Garcia-Lastra, J. M.; Rostgaard, C.; Rubio, A.; Thygesen, K. S., Polarization-induced renormalization of molecular levels at metallic and semiconducting surfaces. *Physical Review B* **2009**, 80, (24), 245427.

[60] Johnson, P. D.; Hulbert, S. L., Inverse-photoemission studies of adsorbed

diatomic molecules. *Physical Review B* **1987**, 35, (18), 9427-9436.

[61] Repp, J.; Meyer, G.; Stojković, S. M.; Gourdon, A.; Joachim, C., Molecules on Insulating Films: Scanning-Tunneling Microscopy Imaging of Individual Molecular Orbitals. *Physical Review Letters* **2005**, 94, (2), 026803.

[62] Kundu, D.; Black, R.; Adams, B.; Nazar, L. F., A Highly Active Low Voltage Redox Mediator for Enhanced Rechargeability of Lithium–Oxygen Batteries. *ACS Central Science* **2015**, 1, (9), 510-515.

[63] Takimiya, K.; Yamamoto, T.; Ebata, H.; Izawa, T., Design strategy for air-stable organic semiconductors applicable to high-performance field-effect transistors. *Science and Technology of Advanced Materials* **2007**, 8, (4), 273-276.

[64] Nelson, R. F.; Leedy, D. W.; Seo, E. T.; Adams, R., Anodic oxidation of 5,10-dihydro-5,10-dimethylphenazine. *Fresenius' Zeitschrift für analytische Chemie* **1966**, 224, (1), 184-196.

[65] Adams, B. D.; Radtke, C.; Black, R.; Trudeau, M. L.; Zaghib, K.; Nazar, L. F., Current density dependence of peroxide formation in the Li-O₂ battery and its effect on charge. *Energy & Environmental Science* **2013**, 6, (6), 1772-1778.

[66] Bryantsev, V. S.; Giordani, V.; Walker, W.; Blanco, M.; Zecevic, S.; Sasaki, K.; Uddin, J.; Addison, D.; Chase, G. V., Predicting Solvent Stability in Aprotic Electrolyte Li-Air Batteries: Nucleophilic Substitution by the Superoxide Anion Radical (O₂(center dot-)). *Journal of Physical Chemistry A* **2011**, 115, (44), 12399-12409.

[67] Schwenke, K. U.; Meini, S.; Wu, X.; Gasteiger, H. A.; Piana, M., Stability

of superoxide radicals in glyme solvents for non-aqueous Li-O₂ battery electrolytes.

Physical Chemistry Chemical Physics **2013**, 15, (28), 11830-11839.

[68] Kim, B. G.; Kim, S.; Lee, H.; Choi, J. W., Wisdom from the Human Eye: A Synthetic Melanin Radical Scavenger for Improved Cycle Life of Li-O₂ Battery. *Chemistry of Materials* **2014**, 26, (16), 4757-4764.

[69] G. Mamantov, A.I. Popov (Eds.): Chemistry of Nonaqueous Solutions, Current Progress, VCH, New York, Basel, Cambridge, Tokyo, ISBN 1-56081-546-9, 1994. *Berichte der Bunsengesellschaft für physikalische Chemie* **1995**, 99, (2), 230-230.

[70] Lim, H.-D.; Gwon, H.; Kim, H.; Kim, S.-W.; Yoon, T.; Choi, J. W.; Oh, S. M.; Kang, K., Mechanism of Co₃O₄/graphene catalytic activity in Li-O₂ batteries using carbonate based electrolytes. *Electrochimica Acta* **2013**, 90, (0), 63-70.

[71] Adams, B. D.; Black, R.; Radtke, C.; Williams, Z.; Mehdi, B. L.; Browning, N. D.; Nazar, L. F., The Importance of Nanometric Passivating Films on Cathodes for Li-Air Batteries. *ACS Nano* **2014**, 8, (12), 12483-12493.

[72] Ottakam Thotiyl, M. M.; Freunberger, S. A.; Peng, Z.; Bruce, P. G., The Carbon Electrode in Nonaqueous Li-O₂ Cells. *Journal of the American Chemical Society* **2012**, 135, (1), 494-500.

Chapter 4. Summary

This thesis is mainly about elucidating reaction chemistry of metal-air batteries, especially Li-oxygen batteries and Na-air batteries and their soluble catalyst. The contents are composed of two parts: (i) Theoretically investigating evidence for low charging overpotentials of superoxide discharge products in metal-oxygen batteries, (ii) Unveiling desired/undesired reaction mechanism of soluble catalyst and their rational design for advanced Li-O₂ batteries.

In the first part of this thesis, the intrinsic properties of the discharge products of metal–oxygen batteries were investigated with respect to their OER kinetics, conductivities, and dissolution properties in the electrolyte. Calculations in this part revealed that the superoxide discharge products, including the hypothetical LiO₂, exhibited better OER efficiencies than the peroxide phases. Furthermore, the ionic conductivities of NaO₂ and LiO₂ were predicted to be 11 and 4 orders higher than those of the peroxide phases, respectively. Even for the solution-mediated mechanism of charging, the dissolution energy of the superoxide phases was calculated to be lower than that of the peroxide phases and was particularly low for NaO₂. Based on all the considered mechanisms, it is believed that the formation of a superoxide discharge product is key to improving the energy efficiency of metal–oxygen batteries.

In the second part, general design principles for finding a soluble catalyst were proposed and their validity was demonstrated using DFT calculations and

experimental verification. The I.E. was suggested as the key descriptor for designing a catalyst, where specific organics with a certain range of I.E. values (5.8–6.8 eV) can be used as soluble catalysts. Furthermore, the HOMO energy level of the catalyst should be considered in comparison with the formation energy of Li_2O_2 and the HOMO energy of the electrolyte. Based on this guideline, DMPZ was successfully identified with a remarkably low overpotential and stability in the Li- O_2 cell. It is believed that the verification of key factors for designing a RM will open up a new avenue to the development of effective novel catalysts and advanced Li- O_2 batteries with high efficiency and long cycle life.

Abstract in Korean

초록

최근 전기자동차 및 에너지저장시스템 시장의 급격한 성장으로 인해 높은 에너지밀도, 낮은 가격을 가지며 친환경적인 전지 시스템의 연구가 중요해지고 있다. 지난 수십 년 간 휴대용 전자기기의 에너지원이었던 리튬이온 전지는, 그 제한된 에너지밀도와 높은 생산단가로 인해 미래의 수요를 충족하지 못할 것으로 예상되고 있다. 이러한 상황에서, 금속 (Li, Na, K, Al 등) 및 공기 분자 (O_2 , CO_2 , SO_2 등)의 직접적인 반응을 이용하여 높은 에너지 밀도를 가지는 금속-공기 전지가 가장 촉망되는 차세대 전지 시스템으로 손꼽히고 있다. 하지만, 이러한 금속-공기 전지는 일반적으로 부반응과 큰 과전압으로 인한 나쁜 수명특성과 낮은 에너지 효율로 인해 상용화에 어려움을 겪고 있다.

이러한 금속-공기 전지 시스템 중에서도 그 구성 원소가 풍부하고 에너지밀도가 특히 높은 리튬-산소 전지와 소듐-산소 전지는 가장 집중적으로 연구되었다. 하지만 리튬과 소듐의 화학적 유사성에도 불구하고, 두 전지 시스템은 매우 다른 특징을 나타내었는데, 특히 리튬-산소 전지의 상대적으로 높은 충전 과전압이 전형적으로 관측되었다. 리튬-산소 전지에 대한 기존 이론 및 실험 연구들에서는

이러한 과전압의 원인을 느린 산소 분자의 방출이나 방전생성물의 낮은 전달 성질을 통해 설명하였다. 하지만, 방전생성물과 과전압 사이의 일반적인 이해는 아직 정확히 정립되지 않고 남아있다. 제 2장에서는, 산소발생반응의 반응속도론, 전하전달 전도도, 용해도의 측면에서 리튬-산소 전지와 소듐-산소 전지의 방전생성물에 대한 충전 반응을 분석하였다. 그 결과 산소발생반응의 반응속도론은 초과산화물 (LiO_2 및 NaO_2)의 경우에 과산화물 (Li_2O_2 및 Na_2O_2)의 경우보다 더 빨랐다. 전기전도도 및 이온전도도의 경우에도 초과산화물이 과산화물보다 훨씬 빠른 것으로 예측되었다. 또한, 용액상 반응을 유도하는 것으로 알려진 용해된 방전생성물들의 용해 에너지를 체계적으로 계산한 결과, 초과산화물, 특히 NaO_2 가 과산화물에 비해 독보적으로 낮은 용해 에너지를 보였다. 이러한 결과는 방전 중 과산화물보다 초과산화물을 생성시키는 것이 금속-공기 전지의 에너지 효율을 향상시키는 데 있어 중요한 열쇠가 될 것임을 시사한다.

리튬-산소 전지에서 높은 수명특성과 높은 에너지 밀도를 달성하기 위해서는 효율적인 촉매를 개발하는 것이 중요한 단계이다. 액상 촉매, 혹은 산화환원 매개체 (RM)은 고체 촉매에 비해 많은 장점을 가지고 있어 일반적으로 훨씬 높은 효율을 나타낸다. 제 3장에서는, 리튬-산소 전지의 촉매 활성화와 안정성을 결정하는 중요 인자를 알아내기 위해

일단의 유기 RM 분자들을 선정하였다. 이를 통해, 많은 데 이터베이스에 이미 조사되어있는 이온화 에너지를 Li_2O_2 및 전해질의 HOMO 에너지를 비교함으로써, 촉매의 활성 및 안정성을 결정하는 인자로서 사용할 수 있음이 밝혀졌다. 이론 및 실험적 분석을 통해 Li_2O_2 와 RM의 이온화 에너지의 비교는 과전압의 크기를 알아 내기 위해, 전해질의 HOMO와 RM의 이온화 에너지의 비교는 안정성을 알아내기 위해 각각 이용할 수 있다는 것을 밝혀낼 수 있었다. 이를 통해 우수한 촉매를 개발하는 일반적인 법칙을 제시하였고, 이 법칙을 이용하여 매우 낮은 과전압과 높은 안정성을 가지는 새로운 액상촉매인 디메틸페나진을 보고하였다.

이번 논문을 통해 새롭게 알려진 충전 과전압의 원인의 이론적 분석 (제 2장) 및 액상촉매의 화학 반응 분석 (제 3장)에 대한 기초적 지식은 금속-공기 전지의 성능 향상을 위한 다른 연구들에 영감을 줄 수 있을 것으로 기대된다.

주요어 : 에너지 저장장치, 제일원리 계산, 금속-공기 전지, 산화환원 매개체

학번 : 2014-30196

Curriculum Vitae

Byungju Lee

+82-1051506269

petitcloud@snu.ac.kr

Educational Background

- **Ph. D. candidate** March 2014 – February 2018 (prospective)

Advanced Energy Materials Laboratory

Department of Materials Science and Engineering

Seoul National University | Republic of Korea

(Supervisor: Prof. Kisuk Kang)

- **Master of Science** March 2012 – February 2014

Advanced Energy Materials Laboratory

Department of Materials Science and Engineering

Seoul National University | Republic of Korea

Thesis Title: “First-principles study on the reaction mechanism in metal-air batteries”

(Supervisor: Prof. Kisuk Kang)

- **Bachelor of Science** March 2008 – February 2012

Major: Materials Science and Engineering

Seoul National University | Republic of Korea

Research Interests

DFT calculations on metal-oxygen batteries

Unveiling fundamental properties of discharge products and reaction mechanism of metal-oxygen batteries

- Physical/chemical properties of discharge products of metal-oxygen batteries
- Discharge/charge mechanism of metal-oxygen batteries and their effect on electrochemical behavior

Mechanism studies on advanced rechargeable batteries

Theoretical studies for next-generation rechargeable batteries

- Novel phosphate cathode materials for Li- and Na-ion batteries
- Solid electrolytes for all-solid-state batteries
- Organic electrodes materials for Li- and Na-ion batteries

Honors and Scholarships

- Korea National Science& Technology Scholarship (2008 – 2009)

List of Publications

(1) Journals

† These authors contributed equally.

- 1) **Byungju Lee**, Hee-Dae Lim, Youngmin Ko and Kisuk Kang "Fast screening of parasitic reaction capability among cell components in lithium-oxygen batteries", In Preparation
- 2) Youngmin Ko†, **Byungju Lee**†, Hyeokjun Park, Hee-Dae Lim, Giyun Kwon, Sechan Lee, Youngjoon Bae, SungKwan Park and Kisuk Kang "Desinging an efficient ORR redox mediators for lithium-oxygen battery", In Preparation
- 3) Youngmin Ko, Hyeokjun Park, Hee-Dae Lim, **Byungju Lee**, Giyun Kwon, Sechan Lee, Youngjoon Bae, SungKwan Park, and Kisuk Kang "Biological redox mediation in electron transport chain of bacteria for oxygen reduction reaction catalysts in lithium-oxygen batteries", Submitted
- 4) **Byungju Lee**†, Youngmin Ko†, Giyun Kwon†, Sechan Lee, Kyojin Ku, Jihyeon Kim, and Kisuk Kang "Exploiting biological systems: Toward eco-friendly and high-efficiency rechargeable batteries", *Joule*, accepted
- 5) **Byungju Lee**, and Kisuk Kang "Materials science: Long-lived electrodes for plastic batteries", *Nature*, Vol 549, pp. 339-340. (2017)
- 6) Hee-Dae Lim†, **Byungju Lee**†, Youngjoon Bae, Hyeokjun Park, Youngmin Ko, Haegyeom Kim, Jinsoo Kim, and Kisuk Kang "Reaction chemistry in

rechargeable Li–O₂ batteries”, *Chemical Society Reviews*, Vol 46, pp. 2873-2888. (2017)

- 7) Jongsoon Kim†, **Byungju Lee**†, Hyungsub Kim, Hyunah Kim, Kisuk Kang “Redesign of Li₂MP₂O₇ (M = Fe, Mn) by tuning the Li diffusion in rechargeable battery electrodes” *Chemistry of Materials*, Vol 28, pp. 6894-6899 (2016)
- 8) Hee-Dae Lim†, **Byungju Lee**†, Yongping Zheng, Jihyun Hong, Jinsoo Kim, Hyeokjo Gwon, Youngmin Ko, Minah Lee, Kyeongjae Cho, Kisuk Kang “Rational design of redox mediators for advanced Li-O₂ batteries” *Nature Energy*, Vol 1, 16066. (2016)
- 9) **Byungju Lee**, Jinsoo Kim, Gabin Yoon, Hee-Dae Lim, In-Suk Choi, Kisuk Kang “Theoretical evidence for low charging overpotentials of superoxide discharge products in metal-oxygen batteries” *Chemistry of Materials*, Vol 27, pp. 8406-8413. (2015)
- 10) **Byungju Lee**, Dong-Hwa Seo, Hee-Dae Lim, Inchul Park, Kyu-Young Park, Jinsoo Kim, and Kisuk Kang “First-principles study of the reaction mechanism in sodium-oxygen batteries” *Chemistry of Materials*, Vol 26, pp. 1048-1055. (2014)
- 11) Sung-Kyun Jung, Hyunchul Kim, Min Gee Cho, Sung-Pyo Cho, **Byungju Lee**, Hyungsub Kim, Young-Uk Park, Jihyun Hong, Kyu-Young Park, Gabin Yoon, Won Mo Seong, Yongbeom Cho, Myoung Hwan Oh, Haegyeom Kim, Hyeokjo Gwon, Insang Hwang, Taeghwan Hyeon, Won-Sub Yoon, Kisuk Kang “Lithium-free transition metal monoxides for positive electrodes in lithium ion batteries”

Nature Energy, Vol 2, 16208 (2017)

- 12) Jinsoo Kim†, Hyeokjun Park†, **Byungju Lee**, Won Mo Seong, Hee-Dae Lim, Youngjoon Bae, Haegyeom Kim, Won Keun Kim, Kyoung Han Ryu, Kisuk Kang “Dissolution and Ionization of Sodium Superoxide in Sodium-Oxygen Batteries” *Nature Communications*, Vol 7, 10670. (2016)
- 13) Do-Hoon Kim, **Byungju Lee**, Kyu-Young Park, Kisuk Kang “First-principles study on charge transport mechanism of lithium sulfide (Li₂S) in lithium-sulfur batteries” *Chemistry - An Asian Journal*, Vol 11, pp. 1288-1292. (2016)
- 14) Young Soo Yun, Kyu-Young Park, **Byungju Lee**, Se Youn Cho, Young-Uk Park, Sung Ju Hong, Byung Hoon Kim, Hyeokjo Gwon, Haegyeom Kim, Sungho Lee, Yung Woo Park, Hyoung-Joon Jin, Kisuk Kang “Sodium-ion storage in pyroprotein-based carbon nanoplates” *Advanced Materials*, Vol 27, pp. 6914-6921. (2015)
- 15) Haegyeom Kim, Ji Eon Kwon, **Byungju Lee**, Jihyun Hong, Minah Lee, Soo Young Park, Kisuk Kang “High energy organic cathode for sodium rechargeable batteries” *Chemistry of Materials*, Vol 27, pp. 7258-7264. (2015)
- 16) Hee-Dae Lim†, Hyeokjun Park†, Hyungsub Kim, Jinsoo Kim, **Byungju Lee**, Youngjoon Bae, Hyeokjo Gwon, Kisuk Kang “A new perspective on Li-SO₂ batteries for rechargeable systems” *Angewandte Chemie International Edition*, Vol 54, pp. 9663-9667. (2015)
- 17) Yuesheng Wang, Liu Jue, **Byungju Lee**, Ruimin Qiao, Zhen-Zhong Yang, Shuyin Xu, Xiqian Yu, Lin Gu, Yong-Sheng Hu, Wanli Yang, Kisuk Kang, Hong

- Li, Xiao-Qing Yang, Liquan Chen, Xuejie Huang “Ti substituted tunnel-type Na_{0.44}MnO₂ oxide as negative electrode for aqueous sodium-ion batteries” *Nature Communications*, Vol 6, 6401. (2015)
- 18) Hyungsub Kim†, Gabin Yoon†, Inchul Park, Kyu-Young Park, **Byungju Lee**, Jongsoon Kim, Young-Uk Park, Sung-Kyun Jung, Hee-Dae Lim, Docheon Ahn, Seongsu Lee, Kisuk Kang “Anomalous Jahn-Teller behavior in manganese-based mixed-phosphate cathode for sodium ion batteries” *Energy and Environmental Science*, Vol 8, pp. 3325-3335. (2015)
- 19) Hee-Dae Lim†, Won Mo Seong†, Jinsoo Kim, Byungju Lee, Dong Hoe Kim, Kisuk Kang “Nb-doped TiO₂ air-electrode for advanced Li-air batteries” *Journal of Asian Ceramic Societies*, Vol 3, pp. 77-81. (2015)
- 20) Dong Ok Shin†, Kyungbae Oh†, Kwang Man Kim, Kyu-Young Park, **Byungju Lee**, Young-Gi Lee, Kisuk Kang “Synergistic multi-doping effects on the Li₇La₃Zr₂O₁₂ solid electrolyte for fast lithium ion conduction” *Scientific Reports*, Vol 5, 18053. (2015)
- 21) Hyunchul Kim, Gwi Ok Park, Yunok Kim, Shoaib Muhammad, Jaeseung Yoo, Mahalingam Balasubramanian, Yong-Hun Cho, Min-Gyu Kim, **ByungJu Lee**, Kisuk Kang, Han-Su Kim, Ji Man Kim, Won-Sub Yoon “New Insight into the Reaction Mechanism for Exceptional Capacity of Ordered Mesoporous SnO₂ Electrode via Synchrotron-based X-ray Analysis” *Chemistry of Materials*, Vol 26, pp. 6361-6370. (2014)
- 22) Jihyun Hong†, Minah Lee†, **Byungju Lee**, Dong-Hwa Seo, Chan Beum Park,

Kisuk Kang “Biologically inspired pteridine redox centres for rechargeable batteries” *Nature Communications*, Vol 5, 5335 (2014)

- 23) Jimin Park†, Hyunah Kim†, Kyoungsuk Jin, **Byungju Lee**, Yong-Sun Park, Hyungsub Kim, Inchul Park, Ki Dong Yang, Hui-Yun Jeong, Jongsoon Kim, Koo Tak Hong, Ho Won Jang, Kisuk Kang, and Ki Tae Nam “A New water oxidation catalyst : Lithium Manganese Pyrophosphate with tunable Mn valency” *Journal of the American Chemical Society*, Vol 136, pp. 4201-4211. (2014)
- 24) Donghwa Seo, Inchul Park, **Byungju Lee** and Kisuk Kang “특집마당: 제일원리 계산을 이용한 리튬/소듐 이차전지용 전극 소재 디자인” *Trends in Metals & Materials Engineering*, Vol 26 (5), pp.28-34. (2013)

(2) Conferences

- 1) Haegyeom Kim, Dong-Hwa Seo, Sung-Wook Kim, Jongsoon Kim, **Byungju Lee** and Kisuk Kang, International Union of Materials Research Society - ICYRAM 2012 (Republic of Singapore, July 1-6, 2012), Poster presentation, “Highly Reversible Co₃O₄/Graphene Hybrid Anode for Lithium Rechargeable Batteries”
- 2) **Byungju Lee**, Dong-Hwa Seo, Hee-Dae Lim, Inchul Park, Kyu-Young Park, Jinsoo Kim, Dohoon Kim, and Kisuk Kang, Materials Research Society Fall Meeting & Exhibit (Boston, Massachusetts, December 1-6, 2013), Poster presentation, “Density functional theory (DFT) study of the reaction mechanism

in sodium-oxygen batteries”

- 3) **Byungju Lee**, Dong-Hwa Seo, Hee-Dae Lim, Inchul Park, Kyu-Young Park, Jinsoo Kim, Dohoon Kim, and Kisuk Kang, International Conference Electronic Materials and Nanotechnology for Green Environment 2014 (Jeju, Republic of Korea, November 16-19, 2014), oral presentation, “First-principles study on the reaction mechanism in metal-air batteries”
- 4) **Byungju Lee**, Dong-Hwa Seo, Hee-Dae Lim, Inchul Park, Kyu-Young Park, Jinsoo Kim, Dohoon Kim, and Kisuk Kang, (Daejeon, Republic of Korea, May 14-15, 2015), oral presentation, “First-principles study on the reaction mechanism in metal-air batteries”
- 5) **Byungju Lee**, Gabin Yoon, Hee-Dae Lim, and Kisuk Kang, 2015 IUPAC 45th World Chemistry Congress (Busan, Republic of Korea, August 9-14, 2015), poster presentation, “Theoretical evidences for low charging overpotentials of superoxide discharge products in metal-oxygen batteries”
- 6) **Byungju Lee**, Gabin Yoon, Hee-Dae Lim, and Kisuk Kang, The 18th Asian Workshop on First-Principles Electronic Structure Calculations (Kashiwa, Japan, November 9-11, 2015), poster presentation, “Theoretical evidences for low charging overpotentials of superoxide discharge products in metal-oxygen batteries”
- 7) **Byungju Lee**, Gabin Yoon, Hee-Dae Lim, and Kisuk Kang, The 56th Battery Symposium in Japan (Nagoya, Japan, November 11-13, 2015), oral presentation, “Theoretical evidence for low charging polarizations of

superoxide discharge products in M-O₂ (M=Li, Na) batteries”

- 8) **Byungju Lee**, Gabin Yoon, Hee-Dae Lim, and Kisuk Kang, The Korean Electrochemical Society 2016 fall meeting (Gwangju, Republic of Korea, April 7-9, 2016), oral presentation, “Theoretical evidence for low charging overpotentials of superoxide discharge products in metal–oxygen batteries”
- 9) Hee-Dae Lim†, **Byungju Lee**†, Yongping Zheng, Jihyun Hong, Jinsoo Kim, Hyeokjo Gwon, Youngmin Ko, Minah Lee, Kyeongjae Cho, Kisuk Kang, The 57th Battery Symposium in Japan (Makuhari, Japan, November 29-December 1, 2016), oral presentation, “Design principles of redox mediator for advanced Li-O₂ batteries”

(3) Patents

- 1) “리튬–공기 전지용 액상 촉매/A soluble catalyst for lithium-air battery” Korean Patent, [KR] 1020150163516
- 2) “p 형 유기 화합물을 포함하는 이차전지용 양극 조성물 및 이를 포함하는 이차전지/ CATHOD MATERIAL CONTAINING P-TYPE ORGANIC COMPOUND AND ION SECONDARY BATTERY COMPRISING THE SAME” Korean Patent, [KR] 1020170000586
- 3) “용액상 방전 반응을 유도하는 퀴논계 액상 촉매를 포함하는 리튬공기전지/ A Lithium air battery comprising quinone-based soluble catalyst inducing discharge in solution” Korean Patent, [KR] 1020160177581